# Articles:

## 1

## Structural Health Monitoring for Prefabricated Building Envelope under Stress Tests

*By: Laura Vandi, Maria Teresa Calcagni, Francesco Belletti, Giuseppe Pandarese, Milena Martarelli, Gian Marco Revel, Vincent Docter and Alessandro Pracucci.*

*Ed. Applied Sciences* **2**

## 2

## Integration of Piezoelectric Energy Harvesting Systems into Building Envelopes for Structural Health Monitoring with Fiber Optic Sensing Technology

*By: Alessandro Pracucci, Laura Vandi, Francesco Belletti, Amanda Ramos Aragão Melo, Marios Vlachos, Angelos Amditis, Maria Teresa Calcagni and David Seixas Esteves*

*Ed. Energies MDPI* **34**

## 3

## Optimization of piezoelectric wind-excited cantilever for energy harvesting from façades

*By: Domenico Tommasino, Federico Moro, Enrique de Pablo Corona, Laura Vandi, Alessia Baietta, Alessandro Pracucci and Alberto Doria*

**65**

applied sciences

MDPI

*Article*

# Structural Health Monitoring for Prefabricated Building Envelope under Stress Tests

**Laura Vandi [1], Maria Teresa Calcagni [2], Francesco Belletti [1], Giuseppe Pandarese [2], Milena Martarelli [2], Gian Marco Revel [2], Vincent Docter [3] and Alessandro Pracucci [1,4,*]**

[1] Focchi S.p.A., 47824 Poggio Torriana, Italy; l.vandi@focchi.it (L.V.); f.belletti@focchi.it (F.B.)
[2] Department of Industrial Engineering and Mathematical Sciences, Università Politecnica delle Marche, 60131 Ancona, Italy; m.t.calcagni@pm.univpm.it (M.T.C.); g.pandarese@staff.univpm.it (G.P.); m.martarelli@staff.univpm.it (M.M.); gm.revel@staff.univpm.it (G.M.R.)
[3] PhotonFirst International, 1812 SC Alkmaar, The Netherlands; vincent.docter@photonfirst.com
[4] Levery S.r.l. Società Benefit, 47814 Bellaria Igea Marina, Italy
* Correspondence: a.pracucci@focchi.it or a.pracucci@levery.it

**Abstract:** This paper details the comprehensive activities conducted in a laboratory setting to assess the structural health monitoring (SHM) of prefabricated building envelopes. Integrating sensors into building components like curtain wall facades poses challenges but offers opportunities for monitoring structural health, requiring compliance with regulatory standards. The research investigates the possibility of defining a kit of conventional and multi-parameter sensors integrated within the building envelope to monitor its behavior during the performance test conducted. The kit of sensors also includes Fiber Optic Sensors for effectively monitoring building envelope behavior and structural integrity. In this context, the European project InComEss (H2020-GA862597) aims to define a stand-alone solution for SHM using Piezoelectric Energy Harvesting Systems (PE-EHS) for façade monitoring through FBG/FOS system. After analyzing the main façade structural stress, a series of FBGs, accelerometers, and force washers were integrated within a 1:1 scale façade prototype and tested in a laboratory following the test sequence parameters required by the curtain wall standard EN 13830. The data collected were analyzed with the aim of monitoring the façade behavior before and after the tests. The results show that the façade's performance passed the assessing test criteria without reporting any damages. In addition, the outcomes demonstrated the effectiveness of the defined kit of multi-parameter sensors for the building envelope's SHM.

**Keywords:** building envelope; façade; structural health monitoring; fiber optic sensor; fiber brag grating; IoT



**Citation:** Vandi, L.; Calcagni, M.T.; Belletti, F.; Pandarese, G.; Martarelli, M.; Revel, G.M.; Docter, V.; Pracucci, A. Structural Health Monitoring for Prefabricated Building Envelope under Stress Tests. *Appl. Sci.* **2024**, *14*, 3260. https://doi.org/10.3390/app14083260

Academic Editors: Luis Hernández-Callejo, Sergio Nesmachnow and Pedro Moreno-Bernal

Received: 14 February 2024
Revised: 25 March 2024
Accepted: 27 March 2024
Published: 12 April 2024



## 1. Introduction

The building environment's increasing reliance on smart technologies opens up opportunities for a deeper understanding and consequent service operations of building performance within the so-called Intelligent Building [1,2]. The relevance of data-driven approaches within the smart built environment is consolidating dynamic control for energy optimization and occupant well-being within building automation [3,4].

This field involves the continuous and real-time assessment of a structure's structural integrity, allowing for the early detection of potential issues such as deterioration, damage, or unforeseen structural changes. In the dynamic and ever-changing urban environment, where buildings are subjected to diverse loads, environmental conditions, and unforeseen events, structural health monitoring (SHM) serves as a proactive measure to mitigate risks and enhance the resilience of structures [5]. By leveraging advanced sensing technologies, data analytics, and monitoring systems, SHM empowers engineers and stakeholders with valuable insights, enabling timely interventions, maintenance, and, ultimately, the optimization of overall performance and safety.

In recent years, both civil construction and the building sector have explored the utilization of sensing technologies for SHM embedded in their structure [6,7]; in particular, focus has been given to the SHM of bridges [8,9]. However, the integration of sensors into non-load-bearing structures, such as a curtain wall façade, represents an increasing topic that needs to be further investigated. Indeed, this component faces the risk of sudden breakage, vulnerability to severe weather conditions, and unexpected collisions. These variables present significant obstacles to maintaining the longevity and dependability of these architectural elements. Recent research focused on the SHM of glass curtain walls of a super-high-rise building by integrating thermocouples in a real building to monitor the temperature distribution [10] with the aim of avoiding thermal shock or monitoring the wind effect on a single-layer cable net with modern curtain walls [11]. SHM sensors in no-load-bearing building components are also useful for analyzing the actual behavior of buildings and the relationship between the building response and the damage caused by earthquakes [12]. Moreover, other solutions for façade SHM could be investigated without directly integrating sensors within the façade; indeed, the study conducted by Brell-Cokcan and Co. investigated the possibility of developing an automated system that scans the façade surface through a projector light with the aim of detecting defections and alerting the automized components' replacing system positioned at the façade perimeters [13].

Investigating sensing solutions embedded in prefabricated façades becomes a perspective opportunity, as demonstrated by the exploration of smart applications for other building applications [14,15]. Indeed, as the interface between the internal and external environments, building envelopes serve as invaluable indicators of a building's structural health. For these reasons, compliance with regulatory standards, such as EN 13830 [16] and CWCT's 'Standard for Systemized Building Envelopes'-Part 8 Testing-Section 8.12.2 [17], is compulsory. Therefore, performing a mock-up validation is required to ensure the façade's functional efficacy and safety. The validation process, outlined in detail in Table A1 and reported in Appendix A of these standards, provides a systematic sequence of steps for conducting the validation phase. Each parameter critical to the façade's performance and safety undergoes evaluation within this framework. Structural integrity and functioning are scrutinized to guarantee compliance with established benchmarks. Indeed, by adhering to these standards, the industry demonstrates a commitment to upholding safety and operational standards in curtain wall façade construction ensuring safety of curtain wall façades, mitigating risks, and safeguarding the well-being of occupants. The standards also defined assessing criteria for each test paraments for verified the façade behavior during each test. These criteria, reported in Table A1 of Appendix A, determine the test pass or failure limit values.

Within this scientific and technological context focused on façade applications, this research investigates the possibility of defining a kit of conventional and multi-parameter sensors integrated within the building envelope to monitor its behavior during performance tests. During the research, the kit is validated with the aim of demonstrating its effectiveness and replicability for structural health monitoring of building envelopes. Therefore, an analysis of conventional sensors was conducted to determine the most suitable ones. Fiber Optic Sensors (FOS) featuring Fiber Bragg Gratings (FBGs) [18,19] are examined with the goal of demonstrating potentialities and limitations for their application in building envelopes. Together with FBG sensors, the possibility of integrating conventional devices was investigated; therefore, vibration sensors and force washers have been explored to monitor structural conditions [20]. Numerous research works have not only considered the use of accelerometers to detect the impact of weathering and external forces on buildings for structural analysis, to monitor the behavior in infrastructure [21] and historical building behavior [22], or to quantify the seismic damage in building structure [23], but also for the identification and verification of possible structural damage because of the stresses imposed on the structure under investigation by performing a modal analysis before and after the events [24]. In fact, modal parameters can be used to evaluate the safety condition of a structure and assess structural health based on modal parameters [25]. Deng et al. [9]

demonstrated that temperature is an important factor that affects the natural frequency of the bridge, and it is not negligible. Therefore, the temperature must be controlled in order to not consider a variation in frequency only due to temperature change as a damage indicator. Strain gauge-based force washers have also been considered as commercial sensors to monitor bolt irregularities [26]. This research focuses on monitoring the structure behavior during the performance of the standard compliance tests for wall curtain façades; the temperature variation results in a few degrees between days since they were accelerated tests, and thus they were performed in short duration even if the temperature is monitored during the performance of the test.

In line with these research and technological scenarios, the EU-funded InComEss project [27] aims to define a stand-alone solution for SHM using Piezoelectric Energy Harvesting Systems (PE-EHS) for façade monitoring [28], and this paper presents the structural health monitoring sensing solutions within the InComEss architectural system [29]. The architectural design of the InComEss system is geared towards harnessing the potential of Piezoelectric Energy Harvesting Systems (PE-EHS) to supply energy to a fiber optic sensor, MonadGator. This interrogator reads data from FBG and communicates with a Power Conditioner Circuit (PCC) seamlessly integrated with a Printed Circuit Board (PCB) powered by a locally implemented Supercapacitor (SC). The connection between the PCC/PCB, an Internet of Things (IoT) gateway, and a cloud-based IoT monitoring platform facilitates data collection and analysis. The overarching objective is to showcase the practicality of Wireless Sensor Networks (WSNs) for structural health monitoring (SHM). Based on the InComEss system architecture conceptualization, the PE-EHS and FBG sensors are designed to demonstrate their integrability within a prefabricated façade. Figure 1 shows the InComEss architecture underlining the components embedded within the façade and the digital components.

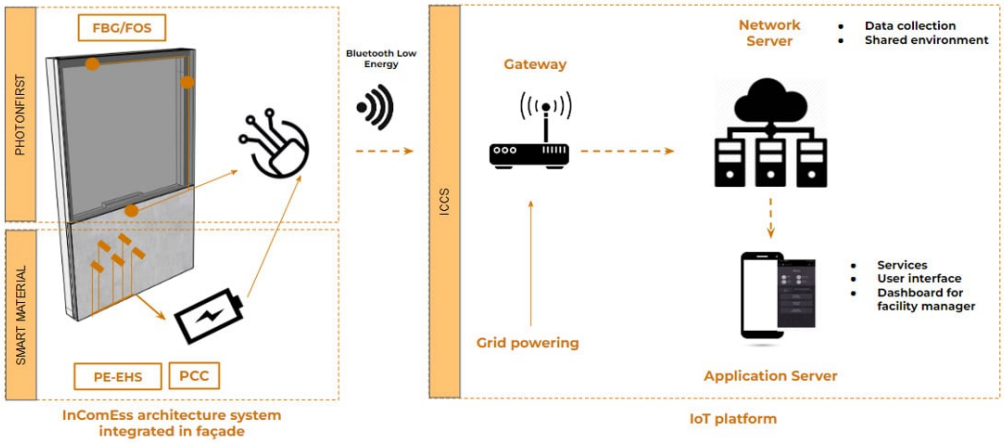


**Figure 1.** Scheme of InComEss system architecture with components integrated into façade and communication to IoT platform.

The first considerations presented are related to physical components such as the FBG sensors. This product represents an application for the façade demo case, and during the InComEss project, it will demonstrate the potential of its applicability for SHM in the building envelope market. An optical fiber consists of a core and cladding. The cladding of the fiber has a typical diameter of 125 µm while the core has a diameter of typically ~10 µm. The core has a higher refractive index than the cladding, such that the light is captured in the core. A Fiber Bragg Grating is a periodic modulation of the refractive index in the fiber core. A representation can be seen in Figure 2.

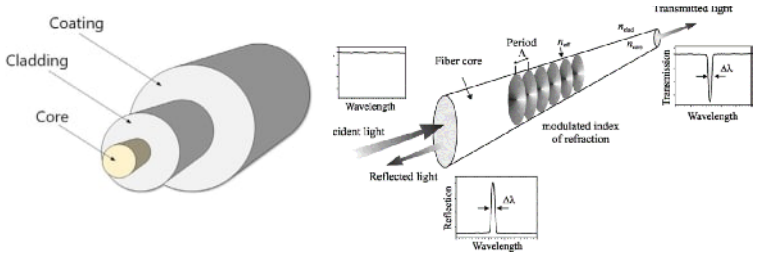


**Figure 2.** Schematic representation of a fiber and Fiber Bragg Grating inscribed into the core of an optical fiber.

The period of the refractive index modulation determines the wavelength of light that is reflected. Due to temperature or strain, the period of the modulation, and thus, its reflected wavelength, will change. Due to this principle, FBG sensors serve dual roles as both strain and temperature detectors. When mounted within a hollow capillary, an FBG sensor exclusively detects temperature changes, disregarding strain. The sensor's wavelength indicates temperature variations through a fixed, linear conversion based on glass material properties. The MonadGator interrogator is the measurement device developed to measure the shift in Bragg wavelength of the FBG sensors. The system uses a light source that emits a broadband wavelength spectrum through the fiber toward the FBG sensors. The reflected wavelength is measured by the MonadGator and converted to a strain or temperature. This MonadGator is designed to operate with low power consumption. Figure 3 reports the InComEss architecture, showing how the energy generated powered the MonadGator for the FBG sensors.

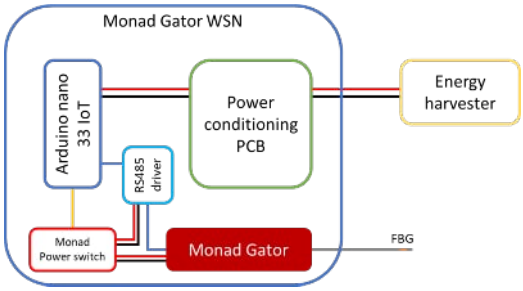


**Figure 3.** Scheme of InComEss architecture.

An Arduino nano is used to rapidly start up the MonadGator and execute a measurement of the FBG wavelength. The broadband light source is turned on for a period of 70 ms. In that time span, the FBG sensor is read, and the data from the photodiodes are acquired by the Arduino. These data are transferred using a Bluetooth Low Energy (BLE) connection to the IOT gateway. The Arduino is powered by a power conditioning circuit, which is charged with the energy that is harvested from the energy harvester connected to this circuit. A total measurement cycle, including wireless data transfer, takes less than 150 ms and uses only 0.08 J of energy per measurement.

In this scenario, the research aims to investigate the possibility of integrating a kit of sensors for structural health monitoring (SHM) into the curtain wall facade to monitor its behavior post-installation. Therefore, this paper outlines the results achieved by the SHM sensors during a performance test, wherein a full-scale facade prototype was subjected to various weather and mechanical conditions in a controlled laboratory environment. The objective was to monitor the facade's behavior under stress from weather conditions and accidental impacts. The paper's objectives are to investigate and provide original contributions in the scientific field to support analyses useful for establishing monitoring solutions integrated into building envelopes using low-consumption sensing technology. Additionally, it aims to explore potential applications within facade components to define the stress application of Fiber Bragg Grating (FBG) and Fiber Optic Sensors (FOS).

Furthermore, the study seeks to validate the facade's integrability and the effectiveness of the multi-parameter sensor kit for facade SHM, along with the measurement method employed.

This paper is structured as follows: Section 2 presents the methods used for the identification of SHM's sensors to be integrated into the façade, along with the tests conducted for their validation and the design and integration activities in the façade; Section 3 presents the outcomes of the laboratory test activities, displaying collected data and graphical representations for SHM sensing technologies; Section 4 highlights the relevant insights that SHM integrated into the façade can provide and identifies gaps for its application; Section 5 summarizes the main achievements related to the paper's goal of analyzing SHM opportunities within stand-alone solutions as the one proposed by InComEss architecture and suggests further investigations needed for market adoption.

## 2. Materials and Methods

This section offers an overview of the developed methodology, including the stages involved, and delineates the materials utilized for conducting the research activities presented in this paper, specifically focusing on the selection of SHM sensors and the testing set-up.

### *2.1. Method*

The methods are focused on the stages deployed for the SHM's sensing solutions adopted within the InComEss system architecture with the following development stages.

#### 2.1.1. Analysis of Façade Structural Stress

The analysis of structuring components to be monitored is investigated with the objective of examining the stress conditions and the range of operations, consequently deriving the sensing solution needed. The comprehensive evaluation of these components to be monitored addresses the final structural health monitoring sensing technologies to be included in an SHM configuration.

Given their exposure to various environmental stressors, such as wind, temperature fluctuations, moisture, accidental impact, and seismic activity, façades are susceptible to degradation and structural issues over time. Consequently, defining the components and parameters relevant to façade monitoring becomes important for effective maintenance, timely detection of defects, solution replicability, and proactive mitigation of risks. Indeed, during the research, a list of possible façade defects to be monitored and relative parameters based on structural analysis and an internal key stakeholders' interview was defined. Table 1 presents the façade parameters, their description, and the range of value acceptable for the façade structural health together with the selected monitoring sensors.

Therefore, Table 1 summarizes the most relevant parameters in terms of façade safety, scheduled for monitoring, accompanied by a selection of the suitability of employing FBG technology and conventional sensors for each defined objective. Alongside FBG, conventional sensors will also be applied in the façade system with the aim of defining a complete kit of sensors for building envelope SHM. Therefore, the kit of sensors selected for the façade monitoring, based on possible façade defects, are described as follows:

- FBGs—Previous applications demonstrated the effectiveness of these technologies in the building and infrastructure sectors, such as bridges [29–31], concrete, wood [32], and steel structures, where strain and temperature have so far been the dominating measurands of interest. Utilizing conventional FBG sensors for SHM in building façades offers significant advantages over electrical strain gauges. Unlike electrical strain gauges, which require multiple wires per sensor point, leading to scalability issues, FBG sensors allow for multiplexing multiple sensors into a single fiber. This feature makes FBG sensors highly suitable for environments requiring numerous sensor points, such as the building envelope sector. The main advantages are their lightweight characteristics, single-ended connections, water and corrosion resistance,

and absence of electric current in the measurement array, making them suitable for embedding within or attaching to a structure [33], which make them suitable for embedding within or attaching to a structure. In addition, research on integrating FBG cables into the façade system involved examining critical factors to determine the optimal configuration. Key considerations included the FBG cable's bending radius, path within façade components towards the monitoring system for efficiency and aesthetics, sensor position, cable dimensions, lengths, thickness, and material properties for fixing method (e.g., glue, silicone). In this research, the use of FBG for temperature monitoring is integrated into the InComEss architecture. Given that the MonadGator can monitor only one FBG at a time, it was connected to the FBG for temperature, which requires punctual monitoring. The integration of FGB for temperature in the glazed façade design should prevent thermal shock episodes in vision and spandrel parts caused by solar radiation and light converting to IR. Installing temperature sensors can prevent damage and provide data for future thermal shock designs. Conversely, conventional FBGs for strain were selected to investigate further applications and to compare their results to those of conventional sensors such as accelerometers. In this case, FBGs for strain are connected to a conventional switchgator, allowing for measuring multiple FBGs and powered by commercial energy.

- Accelerometers—Vibrational sensors have been considered for the monitoring of a structure combined with IoT systems [20]. The vibration signals encompass parameters such as displacement, velocity, and acceleration. Accelerometers prove to be efficient instruments for detecting vibrations. Several studies have been conducted with accelerometers, starting from the structure analysis to identify the weathering and excitation agents affecting the buildings [21–23,34,35] Positioned on curtain wall façades, they detect dynamic forces such as wind or seismic activity, providing insights into structural health by converting vibrations into electrical signals for frequency, amplitude, and duration analysis [35]. Indeed, in this research, accelerometers were used with the following two aims: The first was to evaluate the structural status of the curtain wall façade, performing a modal analysis—one before the tests of compliance and the other one at the end of the tests. The second was the monitoring of the structure during the compliance test to understand the phenomenology of the event affecting the structure. For the façade integration, the sensors were selected based on their dimensions, water-tightness characteristics, and functionalities. Accelerometers are connected to commercial data collectors.
- Force washers—The curtain wall façade relies on precisely torqued screws within a bracket system, which is essential for accurate positioning and optimal performance [36,37]. Therefore, an issue that could affect the life cycle of a structure could be bolt anomalies. Dominika Ziaja et al. analyzed and proposed a procedure for fault detection, as well as for the determination of their location and type, using IoT [26]. This is why, for our project, a non-destructive system, the strain gauge-based force washers—useful for the measurements of the bolt's load—were installed and strategically placed within these brackets to facilitate accurate measurements, providing insights into façade response under diverse conditions. These washers record structural deformations, aiding in ongoing assessment of façade integrity and performance, enhancing structural resilience and efficiency.

In this research, the information exploited by the force transducers was combined with the information from the accelerometers.

**Table 1.** List of defined most relevant parameters to be monitored in terms of safety.

| Label | Description | Range | Selected Sensor |
| --- | --- | --- | --- |
| SHM—thermal shock—temperature | Glazed façade needs to be designed to prevent episodes of thermal shock in vision and spandrel parts linked to the thermal variation due to solar radiation and light conversion into IR on glass and other façade components. The installation of a temperature sensor allows for collecting a set of data to support further thermal shock design. | Temperature of service with a daily excursion between 5 °C and 120 °C<br>Temperature of service with a daily excursion between −5 °C and 80 °C | FBG |
| SHM—mechanical stress—Strain and vibration due to accidental impacts | Façade could be stressed by extraordinary events as accidental and not possible to foreseen impacts, which could compromise the structural façade's behavior. | Accidental impact—range between 6 J (1.224 mm height) and 343 J (700 mm height) | FBG Accelerometer Force washers |
| SHM—mechanical stress—Strain and vibration due to dynamic pressure | Façade is stressed by ordinary (wind load) and extraordinary (seismic load) loads and its mechanical behavior needs to be monitored to guarantee the structural integrity | Pressure ranges from −3000 Pa to +2625 Pa | FBG Accelerometer Force washers |
| SHM—mechanical stress—torque screw | Façade hangs on a brackets system fixed to the load-bearing structure through the utilization of screws specifically torqued to guarantee the right placement and performance of the façade. This torque needs to be preserved during building service to avoid a loss of façade performance and safety issues. The monitoring of torque (e.g., brackets on steelwork) can directly intervene to preserve the façade serviceability and detect defects as distance façade/slab and façade/edge (±5 mm), stack joint distance (±5 mm). | 60–120 N | Force washers |

#### 2.1.2. Sensing Technologies Integration in Façade

Structural sensing technologies are designed for integration in façade, studying their applicability during off-site façade manufacturing, as well as during installation.

The integration of these sensors underwent a thorough examination involving an analysis of several key parameters. Dimensions were examined to determine compatibility and correctness for its application. Further consideration was given to the sensors' positioning, factoring in orientation and functionality to optimize data collection effectiveness. This included assessing the efficacy of data obtained, co-locating commercial sensors near Fiber Bragg Grating (FBG) sensors for direct comparative analysis, and situating sensors to monitor critical components of the facade, such as the center of transom width, the center of mullion height, and the center of the ventilated cavity. Additionally, the routing and length of cables connecting the sensors were analyzed to ensure efficient signal transmission and practical installation. The fixing system methodology was examined to guarantee stability and reliability in data acquisition. This comprehensive analysis contributes to an informed understanding of the integrated sensor system's performance within the context of the monitored facade. In Section 2.3, the final sensor integration designed for the testing activities is reported.

#### 2.1.3. Testing Activities and Outcomes Analysis

The laboratory tests for structural health monitoring sensing technologies were analyzed based on multiple testing conditions to obtain a complete comprehension of their behavior under weather conditions. The FBG/FOS and conventional sensors were analyzed to wrap up potentialities and limitations within real environment applications.

### 2.2. Materials

The materials adopted for the research activities were:

- InComEss components—the research was based on component development within the InComEss project [27] concerning the FOS MonadGator. The FOS MonadGator is based on a low-energy consumption solution for data gathering and transmission of the InComEss system architecture. The FOS MonadGator needs 3.3 V to be powered.
- On-market sensing solutions for SHM:
    a. FBG for FOS to monitor stress conditions of façade. The selection of FBG is based on well-established sensors on the market. The InComEss project did not expect to investigate and develop FBG solutions. The FBG used for this research was a fiber type SM1250B, with a length of 9 mm, a reflectivity of 45%, and 3 dB bandwidth of 0.16 nm. The FBG coating is a fiber polyamide.
- Sensors in the field of structural health monitoring to monitor stress conditions of façade to collect data not collectible from FBG, such as the following:
    a. Accelerometers—On the external side of the façade prototypes, a triaxial accelerometer PCB 354C03 is integrated with IP66 characteristics and a compact dimension of 27 × 21 × 11 mm. It is feasible to be integrated into the façade ventilated cavity. On the internal side, the selected accelerometers are monoaxial sensors model PCB 352C33 with no IP66 characteristics and dimensions of 18 × 11 × 17 mm;
    b. Strain gauge-based force washers—the selected model was the K-KMR+200K-01M5-Q with connectors D-SUB HD 15 polis, and the monitoring system was MX840, 8 channels. This washer has a nominal force of 200 kN based on the standard force applied to façade stresses. Force washers are connected to commercial data collectors.
- Monitoring systems for data collection:
    a. FBG interrogator MonadGator, in which the wavelength range is 1575–1582 nm; noise level: $\sigma < 1$ pm; sampling speed: 2 kHz; FBG's per channel: 1; and the number of channels available is 1;
    b. FBG interrogator switchgator, in which wavelength range is 1516–1583 nm; noise level: $\sigma < 1$ pm; sampling speed: 19.23 kHz; FBG per channel is 8; and the available number of channels is 8;
    c. NI 9234 for accelerometer monitoring;
    d. For the strain gauge-based force, it was the QUANTUM X MX840B monitoring system.
- Prefabricated façade—a unitized façade system for multifactional façades is selected to improve solutions in the same product development.
- Method statement for testing activities conducted in a laboratory environment to validate façade system modules based on EN 13830:2015 [16] and EN 14019:2016 [38] for curtain walling—impact resistance—performance requirements, as referenced in Appendix A. These tests involved the use of a fan positioned at 600 mm and rain-simulating nozzles targeting façade joints, delivering a continuous flow rate of 2 L/min·sqm at 400 mm from the façade. To replicate rain in a controlled laboratory setting, a system employing nozzles at typical joint locations on the façade was used. Two types of rain tests were conducted:
    a. Dynamic Rain Test: this test simulates wind gusts, generating pulsating pressure variations every 3 s, fluctuating between 750 Pa and 250 Pa to mimic the dynamic nature of wind-induced pressure changes.
    b. Static Rain Test: this test aimed to assess behavior under constant rain conditions, maintaining a constant pressure of 600 Pa throughout the test duration.

    Table A1 in Appendix A also includes the fail/pass criteria for each parameter.

### 2.3. Experimental Design

This chapter describes the design of the testing activities, focusing on the sensor's integration within the façade prototype and the test sequence. The façade prototype is composed of 6 prefabricated modules with dimensions of 1400 × 3450 mm. Indeed, the realized 1:1 scale façade mock-up total dimension is 6.90 × 4.50 mt, and the technology used is aluminum frames and double skin glaze. The façade modules were assembled off-site while the sensors were integrated on-site once the façade was installed in the laboratory. The sensor integration was deeply investigated, considering the sensor characteristics and façade components or orientations. In particular, the position of the sensor within the façade was defined according to the following:

- The test standards (EN 13830 [16]), which defined the façade positions and parameters to assess the façade behavior. Indeed, the positions correspond to the most stressful façade position in the central part of aluminum profiles and glazed panels.
- Façade axis. Both FBG and accelerometers were positioned with different orientations with the aim of testing the façade behavior in all directions. As a reference for sensor monitoring, the different axes were considered, such as *X*—left, right; *Y*—up, down; and *Z*—inside, outside.
- Avoiding impact position test—the standard EN 14019 and EN 12600 [39] determine several façade positions where to conduct the impact test; the sensors were not positioned there to avoid damage.

Table 2 shows the list of sensors integrated within the façade prototype for the testing activities.

**Table 2.** Summit of integration sensor within the façade and key information.

| Quantity | Type of Sensor | Measured Physical Quantity | Data Collection System | Application on the Façade | Axis | Sensor Model | Sample Rate [Hz] | Acquisition System [bit] | Sensitivity |
|---|---|---|---|---|---|---|---|---|---|
| 6 | Monoaxial accelerometers | Acceleration | NI 9234 [40] | Internal position | *X*, *Y*, *Z* | PCB 352C33 | 5000 | 24 | 100 mV/g |
| 1 | Triaxial accelerometers | Acceleration | NI 9234 | External position | *X*, *Y*, *Z* | PCB 354C03 | 5000 | 24 | 1000 mV/g |
| 8 | Forced washers | Bolt Tightness | QUANTUM X MX840B [41] | Façade bolt brackets | | K-KMR+200K | 30 | 24 | 2 mV/V Fnom = 200 kN |
| 6 | FBGs (channel 2) | Strain | Switchgator | Internal on aluminum profile | *X* | 0.15 nm FBG | 1000 | 18 | - |
| 3 | FBGs (channel 3) | Strain | Switchgator | External on glass surface | *Z* | 0.15 nm FBG | 1000–19,230 (for impact tests) | 18 | - |
| 1 | FBGs (channel 4) | Temperature | Monadgator | External on glass surface | - | 0.15 nm FBG | <1 | 14 | - |
| 6 | FBGs (channel 5) | Strain | Switchgator | Internal on aluminum profile | *Z* | 0.15 nm FBG | 1000–10,230 (for impact tests) | 18 | - |

The FBG sensors are period refractive index modulation in fiber and are completely solid state. The sensitivity is, therefore, not limited by the FBG sensor but by the measurement system connected to it. At the maximum sample rate of 19.2 kHz, the switchgator interrogator can measure strain changes of 1 microstrain or, when measuring temperature, a temperature change of 0.1 °C. By resampling to lower speeds, this sensitivity is improved by the square root of the resampling factor.

#### 2.3.1. FBG Integration within the Façade

According to the previous outcomes, the fiber optic cables were applied to the glass surface and the aluminum profiles in specific positions. The FBG sensors monitor the direction of its application; thus, two fiber cables were installed to monitor the x and y direction, while one monitored the *z* direction. Figure 4 shows the cable path and the FBG positions within the façade.

- Channel 2—central glazed panel for temperature;
- Channel 3—slightly central glazed panel for strain (to avoid the impact test);
- Channel 5—aluminum central profiles ($x$ direction);
- Channel 6—aluminum central profiles ($z$ direction).

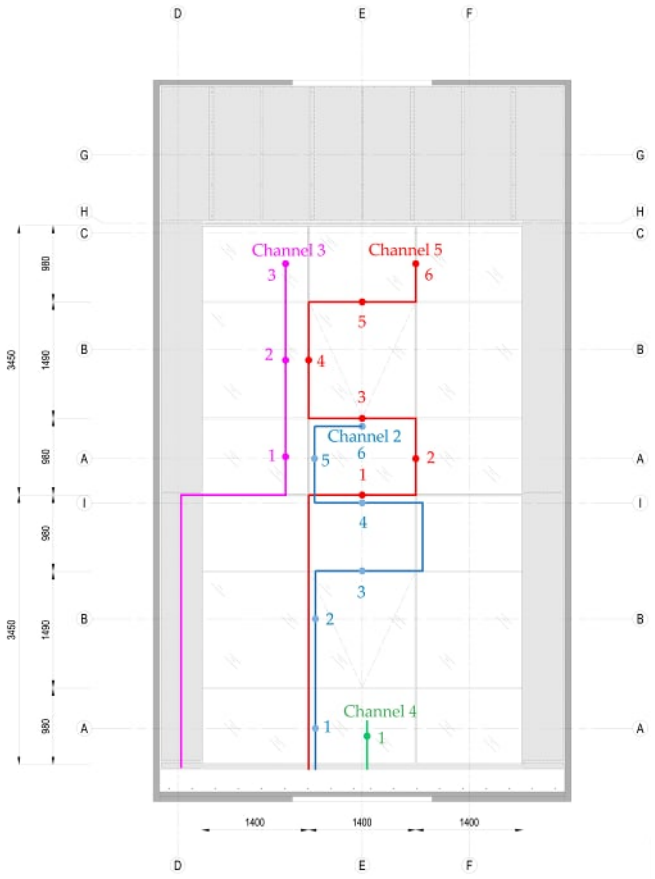


**Figure 4.** Scheme of FBGs channel position.

2.3.2. Accelerometers Integration within the Façade

Figure 5 shows the accelerometer positions, including both external (colored in blue) and internal ones (colored in green). The internal monoaxial accelerometers were located on the aluminum profile corresponding to the FBGs sensors. Indeed, 6 accelerometers were placed beside 6 FBG sensors (the sequence follows channel 5, FBG positioning). Both sensors were positioned in the central part of aluminum mullions and transoms. Considering the middle upper façade modules, there were 6 positions to monitor (upper mullions and transom, openable vent mullions and transom, and lower mullion and transom). For each position, 1 accelerometer and 1 FBG were placed.

2.3.3. Force Washers' Integration within the Façade

Figure 6 shows the No. 8 force washer positions located in the façade brackets bolt to monitor the behavior of each bracket position.

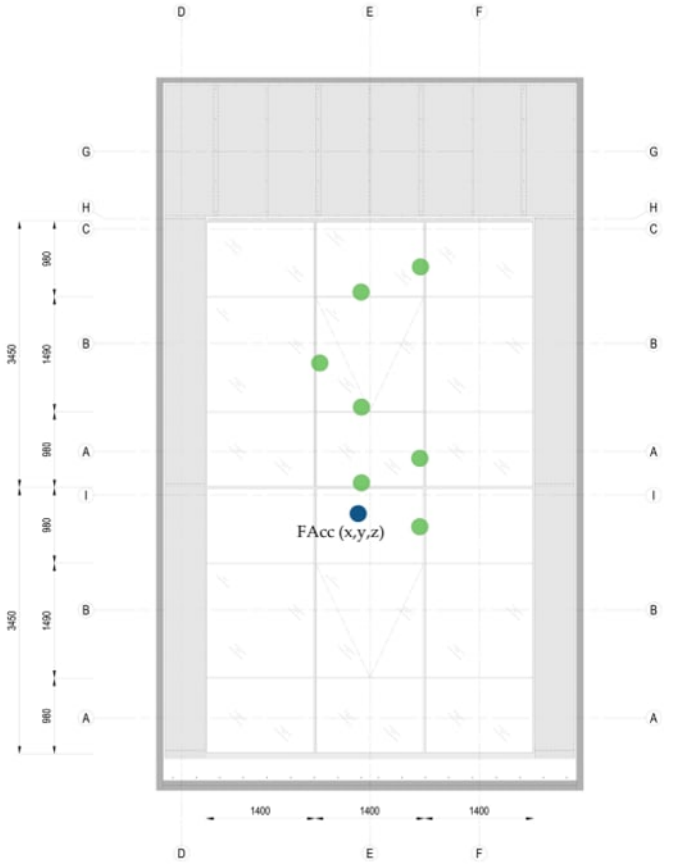


**Figure 5.** Accelerometer positions—façade external view.

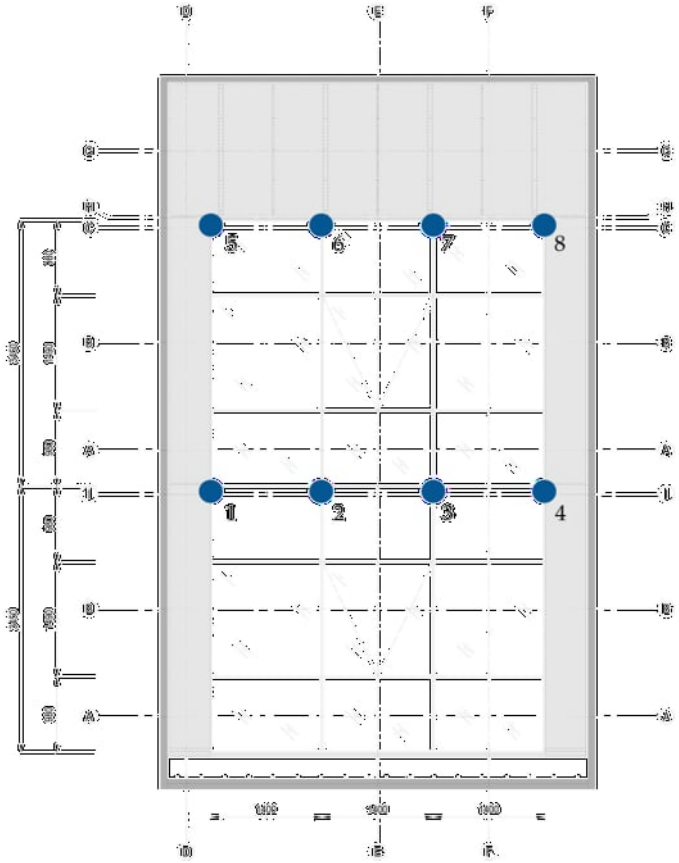


**Figure 6.** Force washers' positions.

### 2.4. Testing Methods

The test aims to monitor the façade behavior and validate the integration of sensors, both regarding the InComEss architecture and the defined kit of conventional sensors. Therefore, the outcomes of previous phases were validated in a controlled lab environment by collecting data from integrated sensors for structural health monitoring (SHM) analysis. The defined set of SHM sensors integrated into a façade prototype was tested under controlled weather conditions following the curtain wall standard EN 13830. During the test, a defined tests sequence was conducted to stress the façade's behavior. The series included air infiltration and exfiltration (+600/−600 Pa), wind pressure and depressure (+1750/2000 Pa for serviceability and +2625/−3000 Pa for safety), and rain in static and dynamic regimes (+600 Pa static test and dynamic water penetration test with a fan pulsing every 3 s from 750 Pa to 250 Pa). The tests were conducted with a fan at 600 mm and with a water source simulating rain in correspondence of façade joints with a flow rate of 2 L/min·sqm and at 400 mm from the façade.

Additionally, mechanical tests such as building movement (horizontal and vertical) and impacts at different times and forces were performed. The full test lasted three days and was performed following a determinate sequence of parameters, as reported in Appendix A. During each test, the façade was constantly monitored and checked in real-time while the sensor's data were collected, considering the test duration and parameters, to facilitate the analysis of the results. The full test sequence is reported in Appendix A (Table A1).

### 2.5. Sample Preparation

The sample preparation involved manufacturing and installation of façade modules and then integrated sensors within the façade. Figure 7 shows the off-site process of façade manufacturing, and Figure 8 shows the on-site installation.

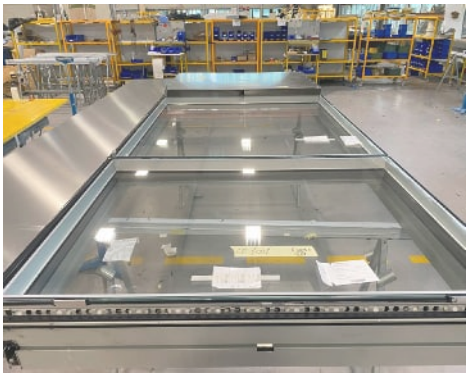

**Figure 7.** Façade manufacturing process.

**Figure 8.** Façade installation process.

For FBG, 4 different cables were installed within the façade: 2 in the glass panel and 2 on the aluminum profiles. Indeed, two cables were fixed on the glass surface through epoxy resin DP125 for bonding on glass (Figure 9), while DP410 was used for bonding on aluminum profiles (Figure 10).

**Figure 9.** FBGs sensors applied on the glass surface for temperature monitoring.

**Figure 10.** FBGs application on the aluminum profile for strain monitoring.

Accelerometers were installed on the curtain wall façade to acquire vibrational phenomena. A triaxial accelerometer was integrated in the external façade side, while 6 monoaxial accelerometers were positioned in the internal façade's side along the central module of the façade as shown in Figures 11 and 12. The triaxial sensor, positioned in the ventilated cavity (thick 67 mm), is fully integrated and not visible from the outside due to its compact dimension (27 × 21 × 11 mm), while the internal monoaxial sensors are visible and not completely integrated into the façade aluminum profiles due to their dimensions.

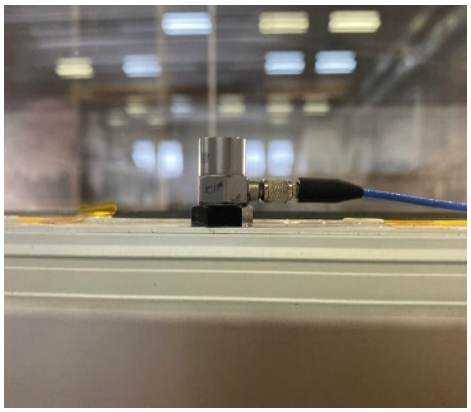

**Figure 11.** Accelerometer applied on aluminum transom.

**Figure 12.** Accelerometer applied on aluminum mullion.

Strain gauge-based force washers were installed on the façade bolts. There were 8 sensors installed, one on each façade bracket. The integration of force washers is shown in Figures 13 and 14.

**Figure 13.** Zoom on the force washer installed on the bracket's bolt.

**Figure 14.** Façade bracket with force washer installation.

## 3. Results and Test Analysis

In the following paragraphs, the results obtained during the test and the relative analysis are reported.

### *3.1. Modal Analysis (Pre/Post)*

Two modal analyses were conducted to assess any changes in structure that might have occurred due to the conformance tests explained in Appendix A. The procedure for the evaluation of the structure was applied to the central module of the wall façade, and the geometry was configured based on the dimension of the module of interest: 54 nodes were created, as shown in Figure 15.

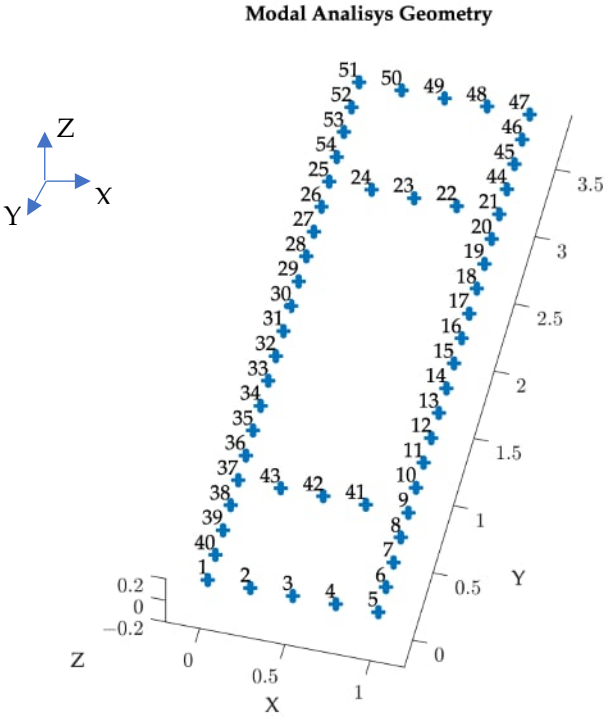


**Figure 15.** Modal analysis geometry consists of 54 nodes representing the modulus of the facade used for performing modal analysis.

An instrumental hammer was used for the excitation of the surface, and the dynamic response at the nodes reported in Figure 15 was measured with monoaxial accelerometers installed for measuring in Z, moved all over the nodes. The force exerted by the hammer and the acceleration were collected by means of a SIEMENS acquisition system (SCADAS). At each node, the frequency response function was calculated as a response over force ratio. The sum of all the FRFs acquired is reported in Figure 16.

A modal analysis was performed on the FRF dataset collected to estimate the dynamic parameters of the structure under test (natural frequencies, damping loss factors, and mode shapes). A comparison between those parameters was estimated in the modal tests performed before and after the stress tests were performed. To compare mode shapes, the Modal Assurance Criterion (MAC) was used; to compare the variation in the natural frequencies, the Natural Frequency Difference (NFD) was estimated. The MAC and the SFD are reported in Figures 17 and 18, respectively.

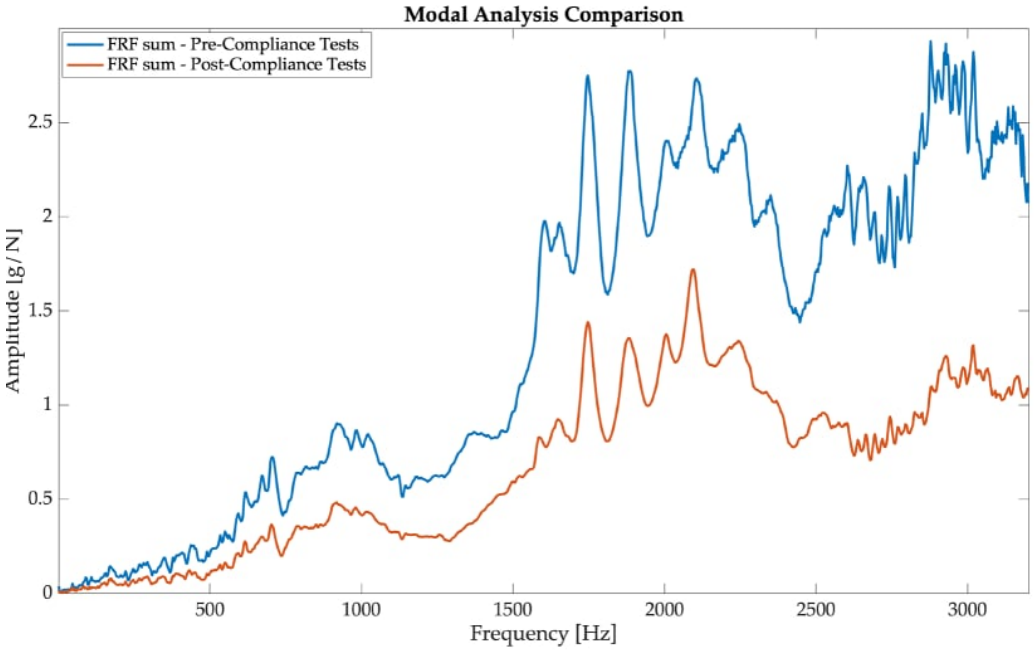


**Figure 16.** FRF sum comparison between pre- and post-compliance tests.

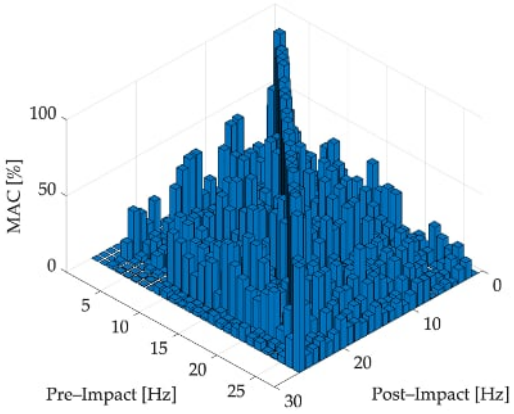


**Figure 17.** MAC (Modal Assurance Criterion) between the two performed modal analysis.

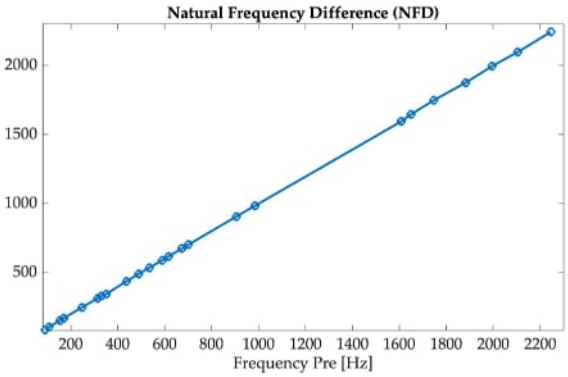


**Figure 18.** NFD (Natural Frequency Difference) between the two performed modal analysis.

Two modes were selected to have an example of the structure movements at selected frequencies, as reported in Figure 19.

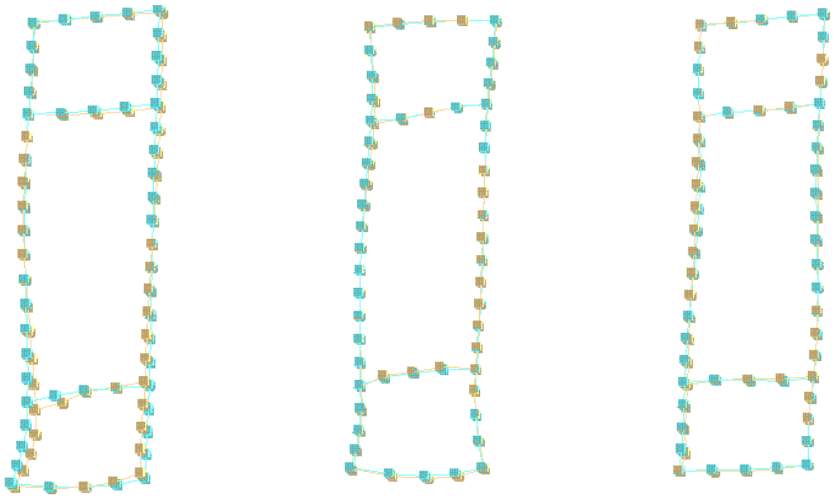

**Figure 19.** Three modal shapes comparison between pre-compliance test and post-compliance test: Yellow markers represent the mode shape estimated before the compliance test and the cyan ones represent the mode shape estimated after the compliance test.

The natural frequencies of all the mode shapes identified with the modal analysis performed on the FRF dataset acquired on the structure before and after the compliance tests are reported in Table 3.

**Table 3.** Modal frequencies pre-compliance test (on the left), post-compliance test (on the right).

| 0–400 Hz | | 400–1000 Hz | | 1000–3000 Hz | |
|---|---|---|---|---|---|
| **Pre-Test** | **Post-Test** | **Pre-Test** | **Post-Test** | **Pre-Test** | **Post-Test** |
| 46.9 | 45.6 | 436.24 | 435.11 | 1608.31 | 1593.50 |
| 90.2 | 82.5 | 489.64 | 489.37 | 1650.3 | 1644.79 |
| 106.6 | 103.7 | 534.23 | 533.5 | 1746.9 | 1746.79 |
| 154.2 | 152.14 | 589.13 | 587.5 | 1882.86 | 1874.07 |
| 169.3 | 168.14 | 615.8 | 614.87 | 1993.2 | 1995.06 |
| 313.9 | 312.19 | 672.64 | 672.34 | 2105.16 | 2096.57 |
| 329.5 | 328.9 | 701.09 | 700.95 | 2246.17 | 2241.69 |
| 351.22 | 343.04 | 984.54 | 982.11 | - | - |

### *3.2. Accelerometers*

In this section, the most relevant results are reported. As mentioned above, the accelerometer results could be comparable, with no significant differences among them. Therefore, in this article, the reported results consist of the data collected and analyzed from the external accelerometer's 'z' direction called FAcc—Z.

The data analysis reveals that relevant and significant results for the façade were obtained. The SHM can be performed considering the fixed installation of accelerometers on a wall curtain façade, as explained in Section 2.5.

At first, the analysis of the signal over time was performed to understand the global response of the accelerometers subjected to the compliance tests. In fact, a Root Mean Square (RMS) analysis of the signal over time was performed for each test day, as reported in Figure 19. In the following figure (Figure 20), the error bar is shown on RMS data for each day. This value was calculated by applying the accelerometer sensitivity value of ±10% to the accelerometer signals. The error band is outlined by a dashed line surrounding the accelerometer signal curve.

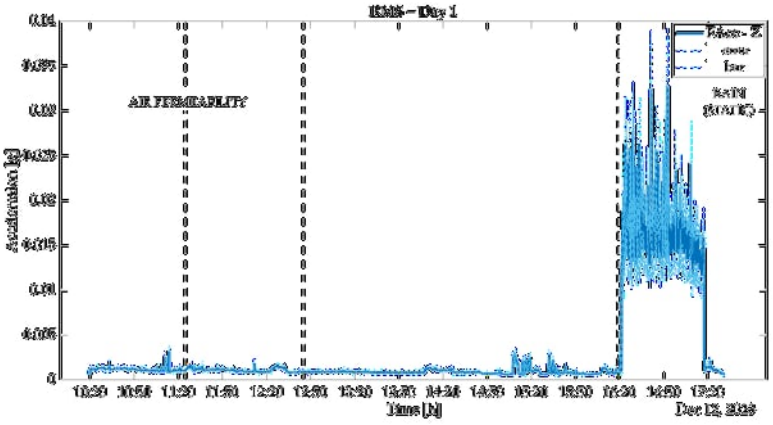

(**a**)

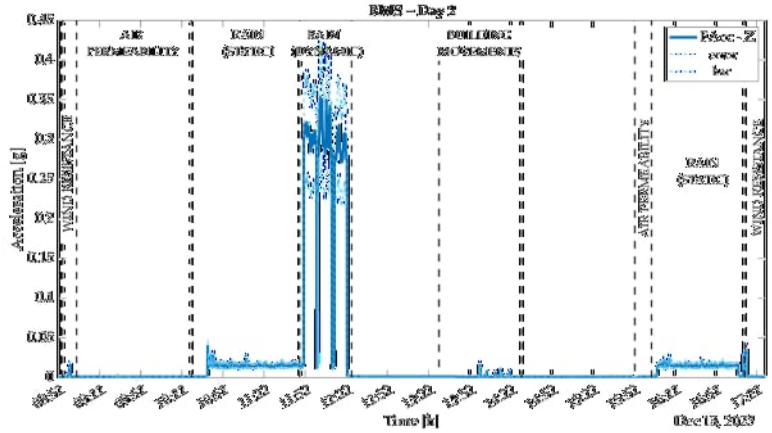

(**b**)

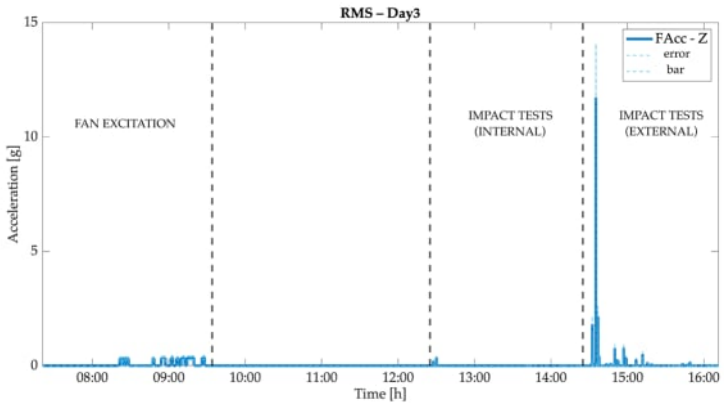


(**c**)

**Figure 20.** Signal RMS analysis. In sequence, top figure: RMS of day 1 (**a**); middle figure: RMS of day 2 (**b**); bottom figure: RMS of day 3 (**c**).

The structure excitation was evaluated for each day; the graph corresponding to each excitation event is reported in time on the left and in frequency on the right.

The tests performed during day 1 were acquired and are shown in Figure 21. During this day, air permeability and rain were performed. The power spectrum estimation function was used to reduce the signal noise and better evaluate information. Each 10 s time history was divided into 0.8 s chunks with a 50% overlap to obtain 25 averages.

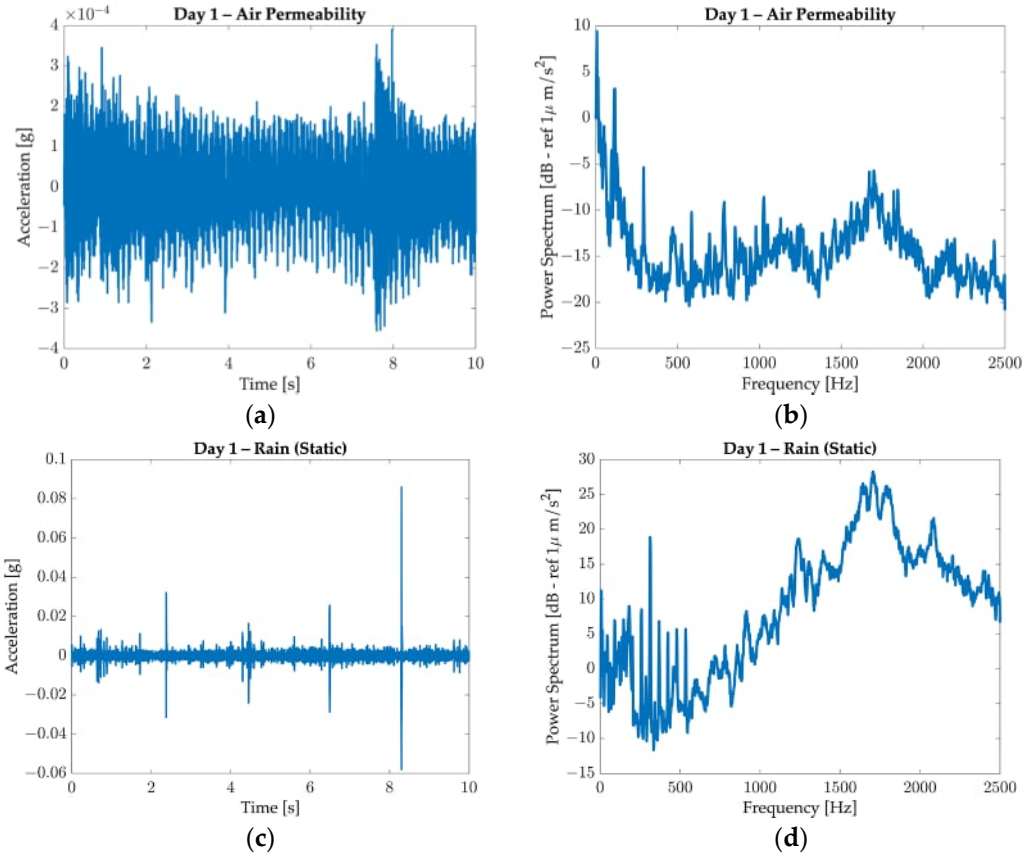


**Figure 21.** Day 1 tests: respectively, story time and power spectrum for each test: air permeability acceleration/time (**a**); air permeability power spectrum /frequency (**b**); rain (static) acceleration/time (**c**); rain (static) power spectrum /frequency (**d**).

The tests performed during day 2 were acquired and are shown in Figure 22, are presented following the chronological order of the appearance of events. During this day, wind (repeated), air permeability (repeated), rain (repeated), and building movements were performed. To reduce the signal–noise ratio, the power spectra of the signals were calculated using a frequency-domain averaging procedure. The 10 s time histories were divided into 0.8 s chunks with a 50% overlap to obtain 25 averages.

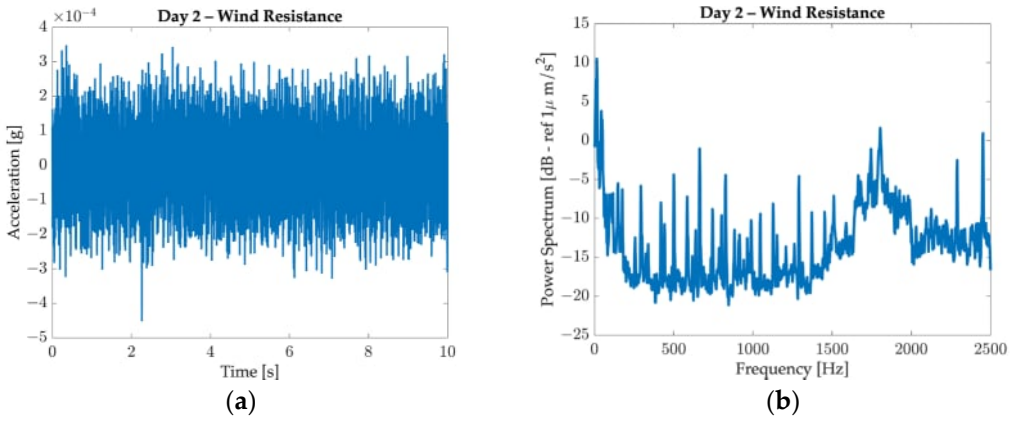


**Figure 22.** *Cont.*

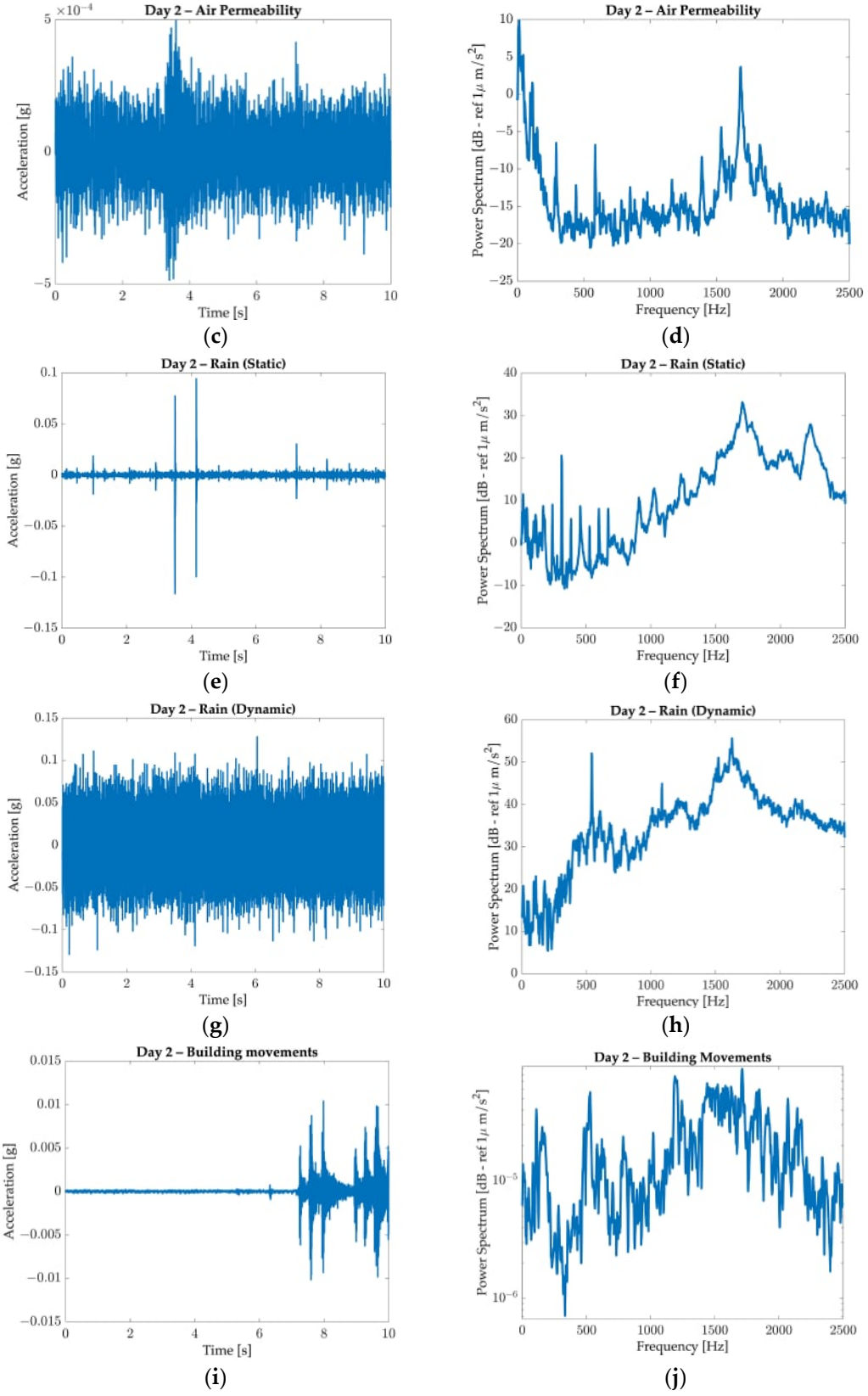


**Figure 22.** *Cont.*

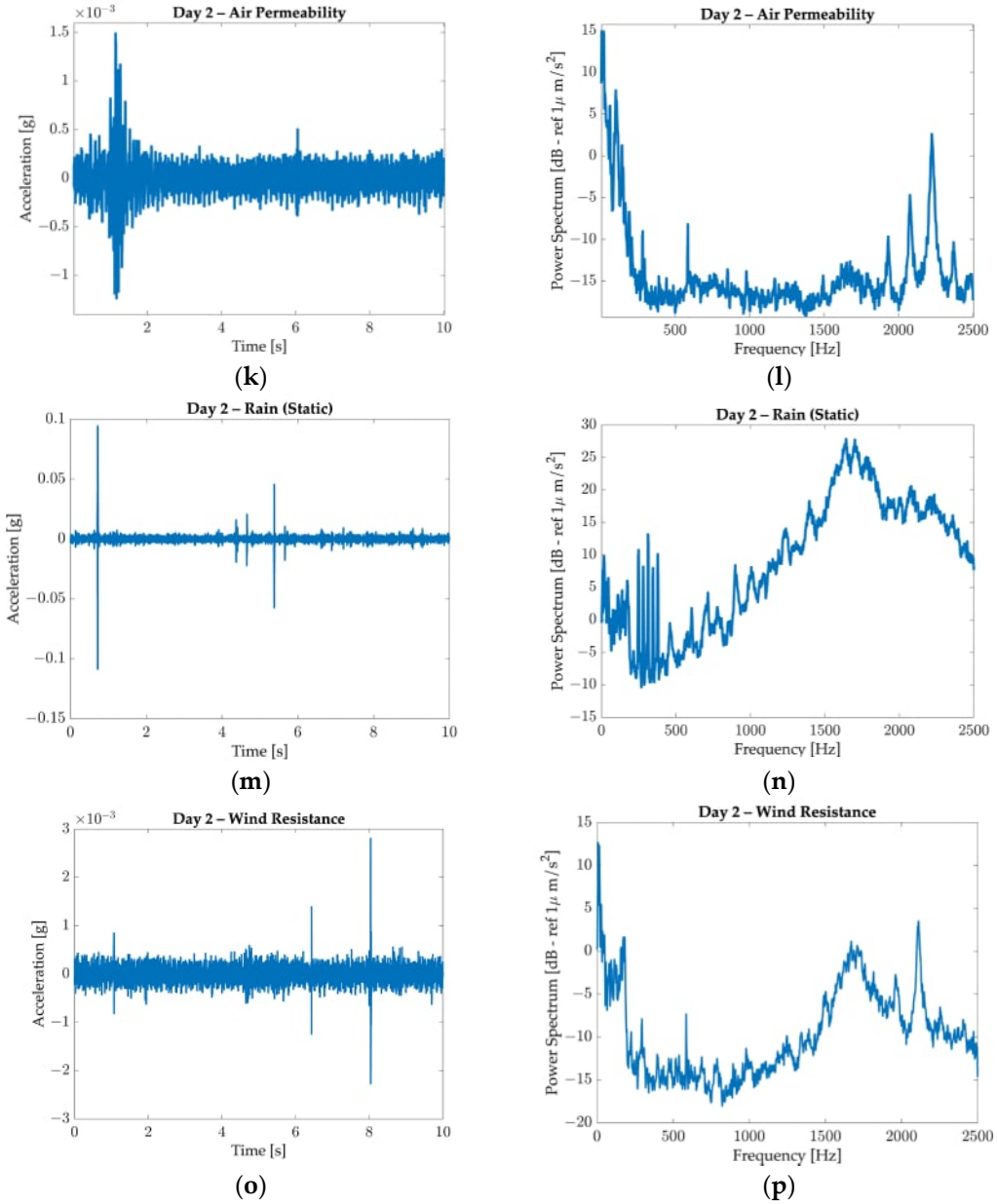


**Figure 22.** Day 2 tests: respectively, story time and power spectrum for each test: wind resistance acceleration/time (**a**); wind resistance power spectrum/frequency (**b**); air permeability acceleration/time (**c**); air permeability power spectral power spectrum/frequency (**d**); rain (static) acceleration/time (**e**); rain (static) power spectrum/frequency (**f**); rain (dynamic) acceleration/time (**g**); rain (dynamic) power spectrum/frequency (**h**); building movements acceleration/time (**i**); building movements power spectrum/frequency (**j**); air permeability acceleration/time (**k**); air permeability power spectrum/frequency (**l**); rain (static) acceleration/time (**m**); rain (static) power spectrum/frequency (**n**); wind resistance acceleration/time (**o**); wind resistance power spectrum/frequency (**p**).

The time history registered during the building movement test Figure 22i is evidenced by several transients. The power spectrum of each transient signal was calculated and then averaged to improve the signal-to-noise ratio.

The tests performed during day 3 were acquired and are shown in Figure 23 and are presented following the chronological order of the appearance of events. During this day, fan excitation and impact tests were performed. The power spectrum estimation function was used to reduce the signal noise and better evaluate information. Each 10 s time history was divided into 0.8 s chunks with a 50% overlap to obtain 25 averages.

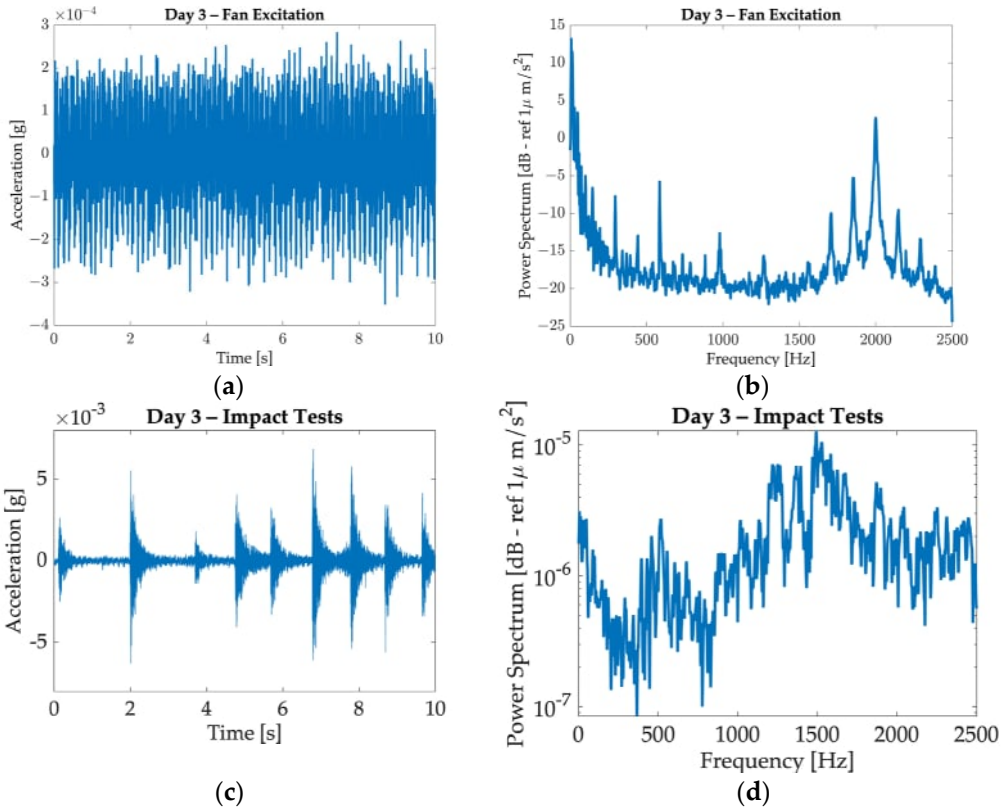


**Figure 23.** Day 3 tests: respectively, story time and power spectrum for each test: fan excitation acceleration/time (**a**); fan excitation power spectrum/frequency (**b**); impact test acceleration/time (**c**); impact test power spectrum/frequency (**d**).

The time histories registered during the impact tests show transient signals typical of impact excitation. The power spectra of these time histories were computed by selecting only three transient signals and averaging their power spectra to improve the signal-to-noise ratio.

The physical phenomenon is demonstrated with the example shown in Figure 24, in which two comparable tests—rain (static)—between two different days (day 1 and day 2) are presented. By comparing the power spectrum acquired during the first rain test (blue line) and the one acquired during the second rain test (red line), it is evident that the resonances excited by the simulated environmental dynamic load (represented by the impacting rain) are shifted towards lower values. This allows the inference that the structure underwent a stiffness decrease, which can be due to structural yielding.

After conducting the tests, it became evident that the structure is stressed during dynamic tests, as monitored by the RMS level of the accelerometers. These dynamic tests allow for the extraction of a frequency response function, revealing various modes of vibration and any changes in the structural response during testing. The responses of the accelerometers can be correlated with those of the other examined sensors.

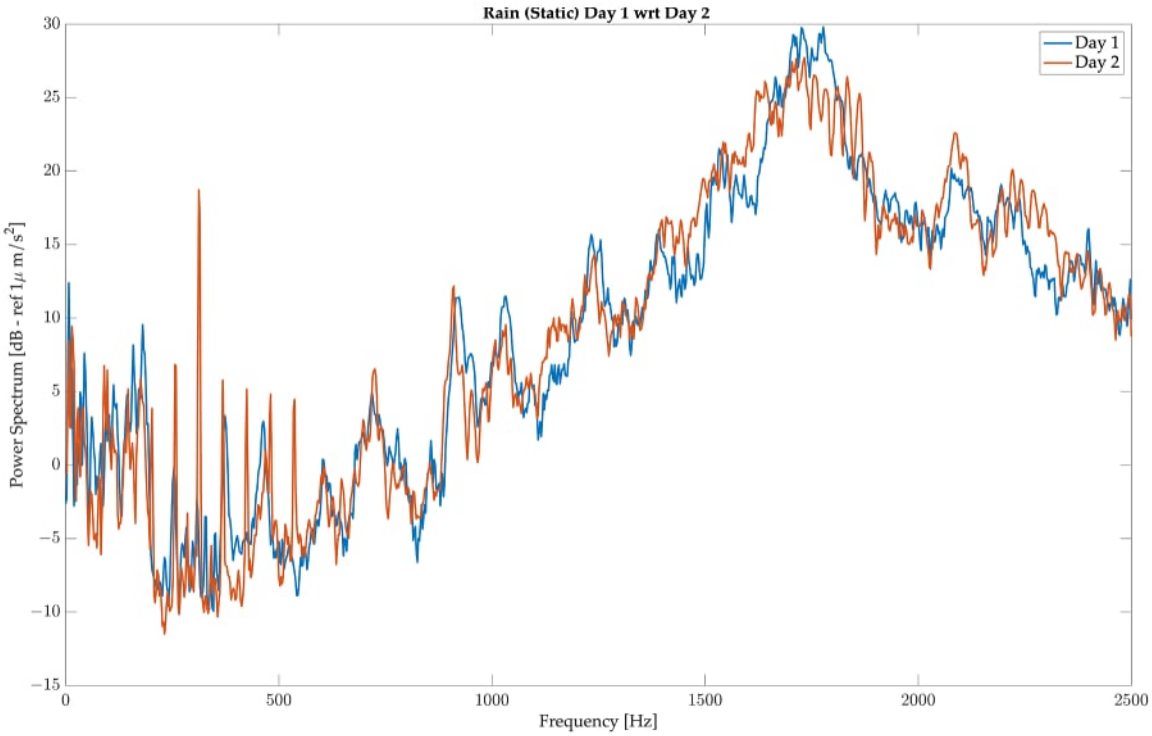


**Figure 24.** Power spectrum comparison between rain (static) test of day 1 and test of day 2.

### *3.3. Force Washers*

This paragraph reports structure behavior during the stress test analysis of the forces. The results obtained are evident in the graphs below (Figure 25). The error bar is delineated by a light blue dashed line surrounding the force washer's signal curves. This band was computed considering the uncertainty related to the sensitivity deviation declared by the washer constructor, which is 1.5%.

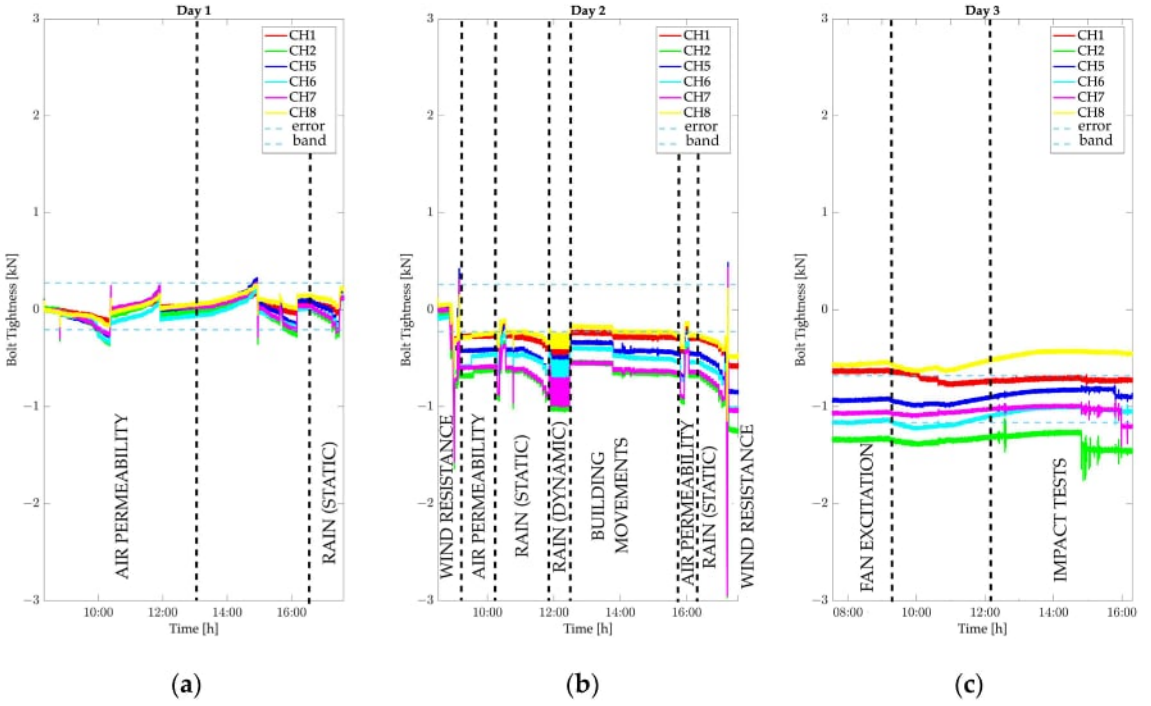


**Figure 25.** Strain gauge-based force washer data collected during the 3 days: day 1 (**a**); day 2 (**b**); day 3 (**c**).

By observing the trend of the bolt's tightness during day 1, it is possible to notice that the tightness at the end of the test is equal to the tightness measured before starting the test; this means that the structure did not experience any modification. On the contrary, during the second day, a negative trend of the bolt's tightness is evident. Table 4 reports the value of the tightness measured by all the washers at the beginning and at the end of the tests performed during day 2 and their difference. It is possible to see that all the washers experience a decrease in tightness, particularly those connected to channels 2 and 7 (see Figure 4) for the force channels position. An important drop in the bolt tightness is visible immediately after the first test (wind resistance). As for day 1 and day 3, the tightness of the bolts remains almost constant.

**Table 4.** Load values of the load cells during day 2.

| Channel | Tightness at the Beginning of the Test on Day 2 | Tightness at the End of the Test on Day 2 | Delta |
|---|---|---|---|
| 1 | 0.4 | −0.6 | 0.64 |
| 2 | −0.06 | −1.3 | 1.2 |
| 5 | 0.02 | −0.8 | 0.82 |
| 6 | −0.08 | −1.02 | 0.94 |
| 7 | −0.004 | −1.03 | 1.026 |
| 8 | 0.04 | −0.4 | 0.44 |

The force washers allow for the visualization of trends in the load curves of individual tests, enabling the identification of instances when the grab brackets experience stress in shear or compression, as well as any loosening of the anchor bolts. Continuous monitoring of the clamping forces will be highly beneficial for the health monitoring of the entire structure and for triggering alerts when the clamping forces fall below the specified limits.

### *3.4. FBG Sensors*

FBGs for temperature—Figure 26 displays the results obtained by the FBG sensor for temperature (Channel 4) associated with the InComEss architecture. A noticeable increase in temperature was recorded during the first day of testing, indicating the correct procedure for data collection. The markable timestamps are as follows: 11.50 h—temperature decrease recorded during the air exfiltration test (−600 Pa) (i); 12.10 h—temperature increase of 0.5 degrees can be observed during the test since a heat lamp was placed near the temperature sensor (ii); 16.30 h—rapid temperature increases from 16 to 18 degrees due to the rain test likely due to the water temperature (iii).

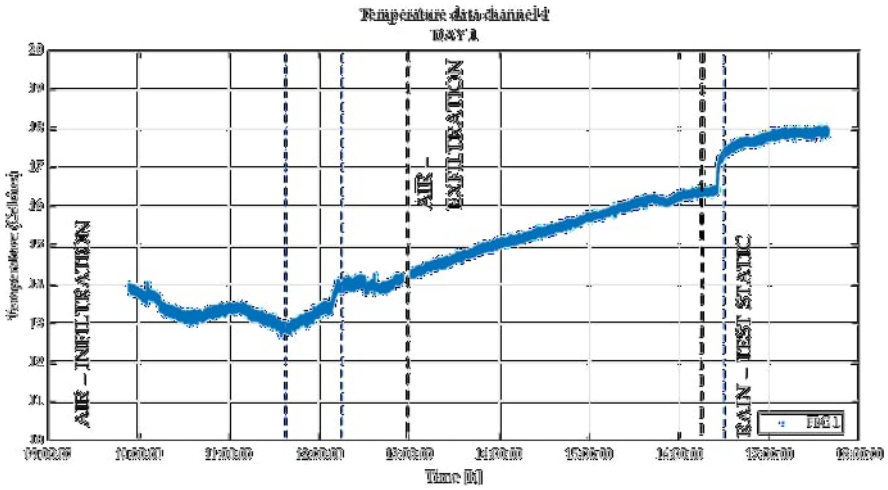


**Figure 26.** Day 1 FBG for temperature—Channel 4.

The temperature on this test day was much more stable throughout the second day, as recorded by the temperature sensor reported in Figure 27.

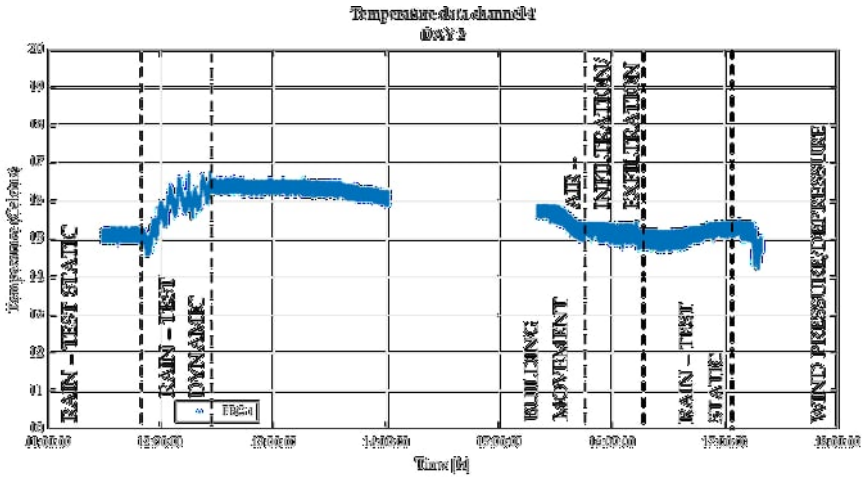


**Figure 27.** Day 2 FBG for temperature—Channel 4.

In this paragraph, the FBG for strain's test results are reported. In Figure 28, the strain results obtained by the cable applied on the glass panel during the first day can be observed. The test started with air infiltration followed by exfiltration, repeated twice. The glass surface reached negative values of strain during the increasing pressure and positive ones during the negative pressure. Indeed, the FBG sensors in the first case were compressed, while in the second, they were expanded.

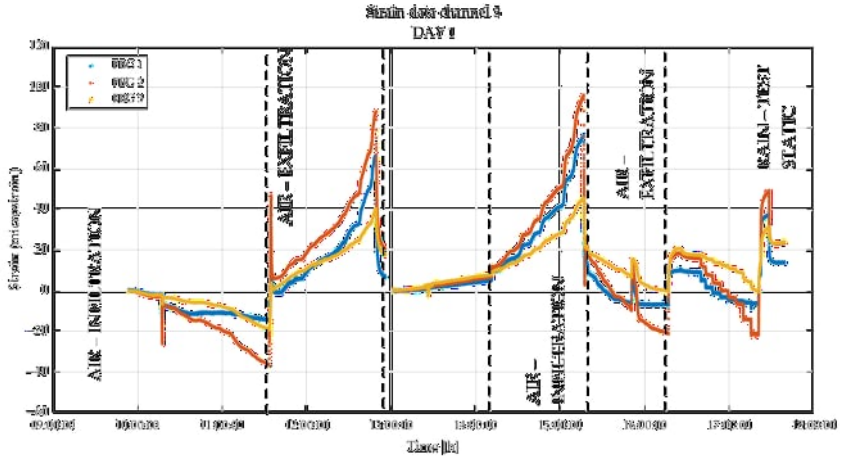


**Figure 28.** Day 1 FBG for strain—Channel 3.

The strain levels on channel 5 (the cable on the aluminum profile) are minor because the sensors are applied on the aluminum profile where the façade strain due to deformation is contained (Figure 29).

The highest strain levels were measured at the end of the second day in channel 3 (z) when the wind pressure and depressure were executed; indeed, in less than 5″, the façade was stressed from 0 to +2625 Pa, and from 0 to −3000 Pa (Figures 30 and 31).

Figure 31 displays the result obtained for channel 5 (x, y) during day 2.

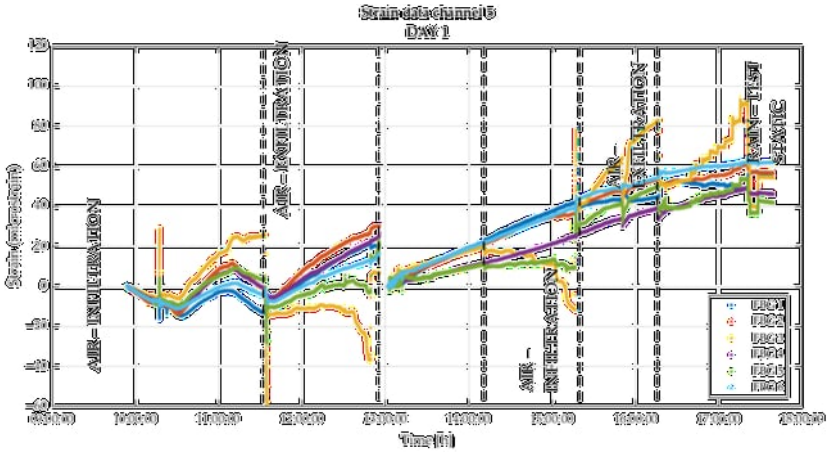

**Figure 29.** Day 1 FBG for strain—Channel 5.

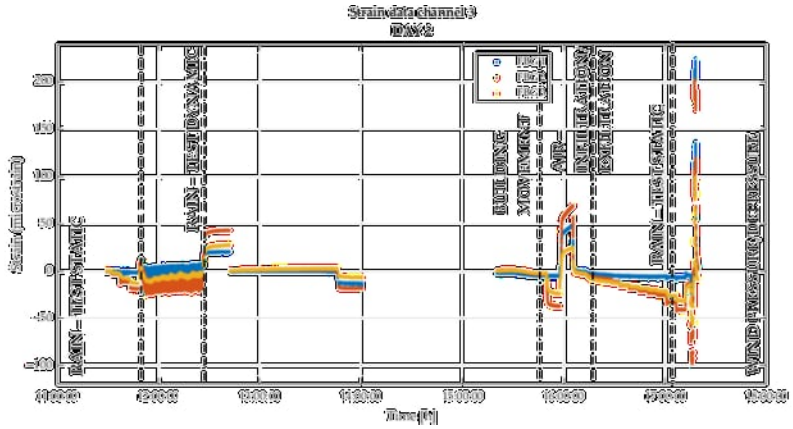

**Figure 30.** Day 2 FBG for strain—Channel 3.

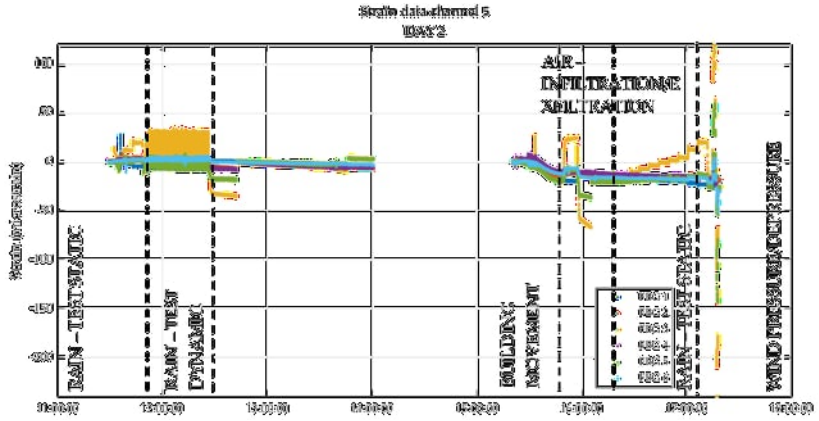

**Figure 31.** Day 2 FBG for strain—Channel 5.

Figure 32 reports the result obtained for channel 2 during day 2. Strain results obtained from channel 2 (*z* direction monitoring) are higher than channel 5 (x, y). This can clearly be observed in the rain—dynamic test, which executes from 11:50 h to 12:20 h, and the rain—test static, which executes from 16:20 h to 17:20 h, where the strain level is raised in steps following the pressure curve increasing(+600 Pa).

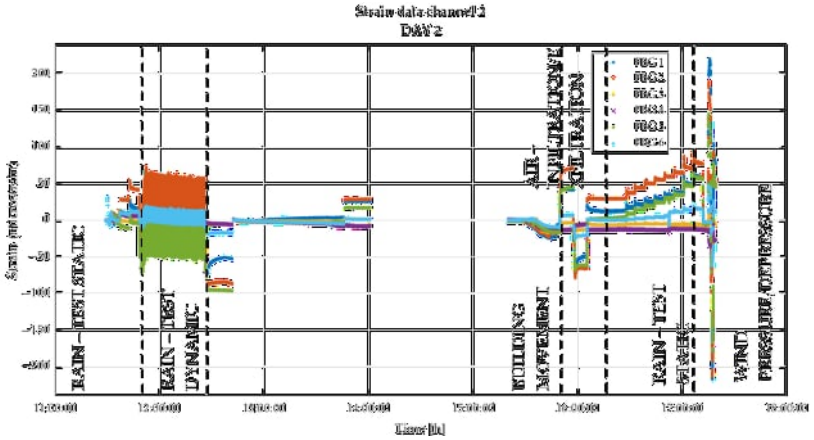


**Figure 32.** Day 2 FBG for strain—Channel 2.

## 4. Discussion

The results demonstrate the efficacy of the developed technique, which is capable of monitoring various parameters. However, it is important to mention that during the test, the façade passed all the assessing criteria defined by the standard. Even though the façade did not undergo damage or deformation, the installed kit demonstrated its potential to be applied in SHM. Indeed, it is sensitive to minor structural variations, suggesting its potential for early damage detection.

Several key findings regarding the performance of different sensor types for building envelope health monitoring under various loading conditions were highlighted by the activities to validate sensing technologies:

- Accelerometers monitor dynamic evidence and impulsive effects acting on the structure and can highlight any critical effects and whether the structure has, therefore, been compromised. Structural variation can be highlighted by performing a comparison between different modal analyses or spectral response variations. From the accelerometers, several considerations can be made from the data collected. From the modal analyses performed before and after the monitoring of the phenomena acting on the glass façade, it was possible to notice a decrease in the modal frequencies of the structure after the exemption of the tests on the wall. This is evidenced by the results obtained in Section 3.2. Regarding the analysis of the structural vibration monitored with the accelerometers attached to the structure, two types of observations can be made: The first one is based on the RMS level of the acceleration that allowed for sensing a significant signal increase when the building was subjected to rain (dynamic), impacts, wind, building movements, and fan excitation. Also, a static rain and air permeability test was sensed by the accelerometers thanks to their high sensitivity (100.5 mV/g), even though the dynamic effects of those loads are limited due to their static nature.
- The second observation is the monitoring of the dynamic behavior of the building, which was monitored by the power spectra estimated from the time histories measured by the accelerometers. The spectra show different signatures depending on the type of test that the building is subjected to. For example, in the fan excitation, the typical harmonic pattern is visible, consisting of the fan blade passing frequency and its high-order harmonics. Another piece of evidence is the deviation detected between the power spectra acquired on the first day of static rain and the same test realized on the second day, see Figure 24. Also, in this case, a decrease in the resonance frequencies of the building was observed, which confirms what is evidenced by the modal analysis.
- Conversely, force washers effectively monitored structural health under static and dynamic loads. They accurately measured applied loads, providing valuable insights into the façade's stress response. Interestingly, washers with embedded sensors revealed normal behavior under typical service loads (600 Pa), regaining initial torque after

stress as demonstrated at the end of tests in the 3 days. However, wind pressure tests (2625 Pa positive, −3000 Pa negative) showed permanent torque changes, indicating high-stress conditions. These sensors detected changes in the washer tightening torque, signifying critical stress levels requiring additional maintenance. This demonstrates the potential of integrating such sensors into façades for continuous monitoring of wind-vulnerable areas, confirming the force loads' suitability for SHM applications. This type of sensor made it possible to visualize the changes during all three days of the tests, and it enabled the capture of static phenomena more prominently. On the second day, it was possible to see that the tests tended to degrade the tension on the screws of the structure from the initial state. Also, considering the uncertainty band of the sensors, it is possible to evidence that some events produced an important tension variation on the screw, at least on some of them and particularly during the tests performed on the second day.

- FBG for temperature—Since the temperature increased all day, the FBG sensors in the other fibers responded to the temperature. The noise contributions in this temperature measurement originate mostly from the FBG interrogator. This causes a noise band up to ~0.3 °C. Resampling of the data to a lower frequency could reduce the noise band. Other noise contributions to the temperature sensor are negligible since the temperature sensor is mounted without strain. FBG sensors react to temperature and strain, so drift in the strain measurements can originate from temperature changes. However, is it possible to correct this when the temperature is known or when a second FBG is used as a temperature sensor for more accurate results? The obtained results validate the feasibility of integrating FBGs into the building envelope to measure temperature, aiming to prevent thermal shock damage. In comparison to conventional sensors such as thermocouples, FBGs offer a valuable alternative due to their compact dimensions, both for the sensor and connectors, and the ability to incorporate multiple tens of sensors in a single fiber. Similar considerations could be applied to the following:
- FBGs for strain and vibration—The obtained results could be compared to those obtained from the conventional force washers. Indeed, the outcomes show the strain and vibration registered during the test provoked by accidental impacts or dynamic pressure. The FBG integration within the façade represents a potential solution due to their characteristic with a particular focus on their dimensions compared to conventional force washers, which have larger dimensions. FBG sensors are solid-state sensors of glass and have no moving or active components. Therefore, the lifetime of the sensors is not critical. Furthermore, no effects are expected on the structural integrity since the sensors are passive and the fiber is less than 1 mm in diameter.
- With respect to the state of the art, this paper presents a methodology based on the use of different types of sensors for measuring a wide number of physical parameters to make identifying possible damages in the SHM field more robust.

## 5. Conclusions

The data-driven approach presented in this paper unlocks a deep understanding of how building envelopes respond to various stresses, including wind, seismic activity, material strain, temperature changes, and other dynamic loads. The research conducted demonstrated the potential of various sensor types for SHM in building envelopes. Considering the nature of different environmental events, a multivariant approach is the best solution for SHM. The facade, in this case, overcame all standard tests, but the different sensors detected minimal structural variation. Modal analysis is useful even if a critical event has been registered and allows for printing the status of the structure in a specific time frame. The final considerations on the obtained results are as follows:

- From the modal analysis point of view, the maximum deviation of the natural frequencies experienced is 1.2% between the structure status at the beginning and at the end of the certification tests.

- This was also confirmed by the monitoring accelerometers and observing the power spectra of the time histories registered during rain (static) between day 1 and day 2 (Figure 16, where the shift towards lower natural frequency is evident)
- Force washers evidenced that between day 1 and day 2, the bolts undergo loosening, especially concerning the bolt registered by the sensor installed on channel 2 (a decrease in the tension of that bolt of about 8% was registered).
- Integration of FBGs into building envelopes for temperature monitoring prevents thermal shock damage, offering compact size and multiplexing capabilities. FBGs also excel in strain, ensuring longevity and structural integrity, with potential applications in façades to improve safety during the entire life of the structure.

The achieved results demonstrate that sensing façade for SHM can open new approaches in the following: preventive maintenance schedules within the building envelope, identifying potential issues before they become critical, thereby reducing downtime and costs and minimizing environmental impact, reducing unnecessary repairs and interventions by prioritizing targeted maintenance based on data-driven insights; prioritizing retrofitting requirements directing resources towards façade areas most in need of improvement for enhanced safety; guiding design improvements integrating real-world performance data into future building designs for increased resilience and sustainability. For future works, a threshold that identifies and detects anomalies will be studied for each variable. In addition, it is also necessary to optimize sensor placement, with a particular focus on integration within the façade, finding a balance between aesthetic harmony, sensor monitoring, and maintenance. Sensor integration should be conducted during manufacturing activities, with the aim of inserting them into the aluminum profile cavity and isolated chamber within double-glazed panels. Other applications could be investigated, such as embedding Fiber Bragg Gratings (FBGs) for temperature monitoring in glass PVB components during the glass lamination phase, aiming to prevent thermal shock glass defects and guarantee aesthetic harmony in the building envelope. Additionally, integrating FBGs for strain monitoring in structural silicone, which are responsible for supporting hundreds of kilograms of glass in minimal space, can ensure the façade's safety and serviceability.

**Author Contributions:** Conceptualization, A.P. and L.V.; methodology A.P. and L.V.; software, M.T.C. and G.P.; validation, A.P. and L.V.; formal analysis, A.P., L.V. and M.M.; investigation, A.P., L.V. and G.M.R.; resources, A.P., L.V., F.B., V.D., M.T.C. and G.P.; data curation, A.P., L.V., V.D., M.T.C. and G.P.; writing—original draft preparation, A.P. and L.V.; writing—review and editing, A.P., L.V., F.B., M.M., G.M.R., V.D., M.T.C. and G.P.; visualization, L.V., F.B., V.D., M.T.C. and G.P.; supervision, A.P.; project administration, A.P.; funding acquisition, A.P. All authors have read and agreed to the published version of the manuscript.

**Funding:** This research was funded by the European Union's Horizon 2020 Research and Innovation Program, grant number 862597.

**Institutional Review Board Statement:** Not applicable.

**Informed Consent Statement:** Not applicable.

**Data Availability Statement:** The original contributions presented in the study are included in the article, further inquiries can be directed to the corresponding author.

**Conflicts of Interest:** Authors Laura Vandi, Francesco Belletti and Alessandro Pracucci was employed by the company Focchi S.p.A. Author Vincent Docter was employed by the company PhotonFirst International. Author Alessandro Pracucci was employed by the company Levery S.r.l. Società Benefit. Author Maria Teresa Calcagni, affiliated with Università Politecnica delle Marche, was engaged with a service contract by the company Focchi S.p.A. The remaining authors declare that the research was conducted in the absence of any commercial or financial relationships that could be construed as a potential conflict of interest.

## Appendix A

**Table A1.** Laboratory environment's tests method statement.

| Sequence | Test | Activity—Range Values | Pass/Fail Criteria = | EU Reference | Test Time |
|---|---|---|---|---|---|
| 1A | Air—infiltration | Test Pressure: +600 Pa (Class A4) | Air leakage $\leq$ 1.5 $m^3/hm^2$ | EN 12152 [42], EN 12153 [43] | 45′ |
| 1B | Air—exfiltration | Test Pressure: −600 Pa (Class A4) | Air exfiltration rate $\leq$1.5 $m^3/hm^2$ at test pressures up to 100 Pa | | 1 h 15′ |
| 2 | Rain—test static | Test pressure: 600 Pa (Class R7) | No leakage at 600 Pa | EN 12154 [44], EN 12155 [45] | 55′ |
| 3A | Wind—pression | Test pressure: +1750 Pa | Mullion deflection limit: 3435/300 + 5 = 16.45 mm (ABC) Residual deformation: 005 *Max measured deformation or 1 mm) | EN 12179 [46] | 8′ |
| 3B | Wind—depression | Test pressure: −2000 Pa | | | 8′ |
| 4A | Air—infiltration | Test Pressure: +600 Pa (Class A4) | Air leakage shall not exceed that measured at point 1B by more than 0.3 $m^3/hm^2$ | EN 12152, EN 12153 | 8′ |
| 4B | Air—exfiltration | Test Pressure: −600 Pa (Class A4) | Air leakage shall not exceed that measured at point 2 by more than 0.3 $m^3/hm^2$ | | 8′ |
| 5 | Rain—test static | Test pressure: 600 Pa (Class R7) | No leakage at 600 Pa | EN 12154, EN 12155 | 1 h 5′ |
| 6 | Rain—test dynamic | Dynamic water penetration test with fan with a pulsing every 3 s from 750 Pa to 250 Pa | No leakage | CWCT 'Standard Method for building envelope' part 8. clause 8.7.2.1 | 36′ |
| 7A | Building movement—vertical | 1. Vertical offset of the intermediate unit: uz = ±7 [mm]—2 cycles | - | CWCT 'Standard Method for building envelope' part 17 | n.a. |
| 7B | Building movement—horizontal | 2. Horizontal offset of the intermediate beam: uz = ±7 [mm]—2 cycles | - | CWCT 'Standard Method for building envelope' part 17 | n.a. |
| 8A | Air—infiltration | Test Pressure: +600 Pa (Class A4) | Air leakage shall not exceed that measured at point 1B by more than 0.3 $m^3/hm^2$ | EN 12152, EN 12153 | 7′ 30′′ |
| 8B | Air—exfiltration | Test Pressure: −600 Pa (Class A4) | Air leakage shall not exceed that measured at point 2 by more than 0.3 $m^3/hm^2$ | | 7′ 30′′ |
| 9 | Rain—test static | Test pressure: 600 Pa (Class R7) | No leakage at 600 Pa | EN 12154, EN 12155 | 1 h |
| 10A | Wind—pression | Test pressure: 2625 Pa | Integrity: Residual deformation = 6.90 mm (3435 mm/500) | EN 12179 | 2′ |
| 10B | Wind—depression | Test pressure: −3000 Pa | | | 2′ |
| 11 | Fan excitation | Dynamic test | - | - | 1 h 35′ |
| 12A | Impacts test- hard body | 6 J (1.224 mm height with 0.5 kg steel ball) 10 J (1.020 mm height with 1.0 kg steel ball) | Negligible risk (TN76) | CWCT TN 76 | n.a. |
| 12B | Impact test—soft body | 120 J (245 mm height) 500 J (1020 mm height) | Negligible risk (TN76) | | n.a. |
| 12C | Impact test—double tyre | 343 J (700 mm height) | No part exceeding the mass of 50 g shall fall. No holing shall occur permitting a test block E2 according to EN 1630 (ellipse) to be passed through it; | EN 14019 and BS 12600 | n.a. |

## References


1. Wang, G.; Ke, J. Literature Review on the Structural Health Monitoring (SHM) of Sustainable Civil Infrastructure: An Analysis of Influencing Factors in the Implementation. *Buildings* **2024**, *14*, 402. [CrossRef]
2. Intelligent Buildings—An Overview | ScienceDirect Topics. Available online: https://www.sciencedirect.com/topics/engineering/intelligent-buildings (accessed on 29 January 2024).
3. Blum, D. *Data-Driven Smart Buildings: State-of-the-Art Review*; Energy in Building and Communities Programme; CSIRO: Newcastle, NSW, Australia, 2023; p. 103.
4. Kaboli, A.; Shirowzhan, S. *Advances and Technologies in Building Construction and Structural Analysis*; IntechOpen: London, UK, 2021; ISBN 978-1-83881-141-9.
5. Faridi, A.; Roy, K.; Singhal, V. *Damage Quantification in Beam-Type Structures Using Modal Curvature Ratio*; Innovative Infrastructure Solutions; Springer International Publishing: Berlin/Heidelberg, Germany, 2024.
6. Valinejadshoubi, M.; Bagchi, A.; Moselhi, O. Structural Health Monitoring of Buildings and Infrastructure. *Int. J. Civ. Environ. Eng.* **2016**, *10*, 9.
7. Ferreira, P.M.; Machado, M.A.; Carvalho, M.S.; Vidal, C. Embedded Sensors for Structural Health Monitoring: Methodologies and Applications Review. *Sensors* **2022**, *22*, 8320. [CrossRef] [PubMed]

8. Comisu, C.-C.; Taranu, N.; Boaca, G.; Scutaru, M.-C. Structural Health Monitoring System of Bridges. *Procedia Eng.* **2017**, *199*, 2054–2059. [CrossRef]
9. Deng, Z.; Huang, M.; Wan, N.; Zhang, J. The Current Development of Structural Health Monitoring for Bridges: A Review. *Buildings* **2023**, *13*, 1360. [CrossRef]
10. Li, S.; Chen, S. Field Monitoring and Prediction on Temperature Distribution of Glass Curtain Walls of a Super High-Rise Building. *Eng. Struct.* **2022**, *250*, 113405. [CrossRef]
11. Yang, B.; Zhu, H.; Wüchner, R.; Zhang, Q. Monitoring of Wind Effects on a Wind-Sensitive Hybrid Structure with Single-Layer Cable-Net Curtain Walls under Typhoon Muifa. *J. Build. Eng.* **2021**, *44*, 102960. [CrossRef]
12. Ogasawara, S.; Kanda, K.; Suzuki, Y. Damage Investigation of Non-Structural Components in Buildings with SHM System in the 2018 Osaka Earthquake. In Proceedings of the 17th World Conference on Earthquake Engineering, Sendai, Japan, 13–18 September 2020.
13. Brell-Cokcan, S.; Adams, T.J.; Kerber, E.; Dai, R.; Lee, H.J.; Kirner, L.T.; von Hilchen, M.; Adams, T.J. *Construction & Robotics: Research Driven Project, Volume 1: Research Paper/SS 2021*; RWTH Aachen University: Aachen, Germany, 2022; 179p.
14. Bouzan, G.B. Building Facade Inspection: A System Based on Automated Data Acquisition, Machine Learing, and Deep Learning Image Classification Methods. *ARPN J. Eng. Appl. Sci.* **2021**, *16*, 1516.
15. Giovanardi, M.; Baietta, A.; Belletti, F.; Magnani, S.; Casadei, O.; Pracucci, A. Exploiting the Value of Active and Multifunctional Façade Technology through the IoT and AI. *Appl. Sci.* **2024**, *14*, 1145. [CrossRef]
16. *EN13830-2022*; Curtain Walling. CEN—Comitè Europeen de Normalisation: Bruxelles, Belgium, 2022.
17. Armstrong, S.; Auty, M.; Aylward, T.; Campbell, J.; Claridge, P.; De Bleecker, H. *Standard Test Methods for Building Envelopes*; Centre of Window and Cladding Technology: Bath, UK, 2005; ISBN 1-874003-39-4.
18. Majumder, M.; Gangopadhyay, T.K.; Chakraborty, A.K.; Dasgupta, K.; Bhattacharya, D.K. Fibre Bragg Gratings in Structural Health Monitoring—Present Status and Applications. *Sens. Actuators Phys.* **2008**, *147*, 150–164. [CrossRef]
19. Bremer, K.; Wollweber, M.; Weigand, F.; Rahlves, M.; Kuhne, M.; Helbig, R.; Roth, B. Fibre Optic Sensors for the Structural Health Monitoring of Building Structures. *Procedia Technol.* **2016**, *26*, 524–529. [CrossRef]
20. Ur Rehman, S.; Usman, M.; Younus Toor, M.H.; Hussaini, Q. Advancing Structural Health Monitoring: A Vibration-Based IoT Approach for Remote Real-Time Systems. *Sens. Actuators Phys.* **2024**, *365*, 114863. [CrossRef]
21. Mazzei, M.; Lellis, A.M.D. Capacitive Accelerometers at Low Frequency for Infrastructure Monitoring. *Procedia Struct. Integr.* **2023**, *44*, 1212–1219. [CrossRef]
22. Arezzo, D.; Quarchioni, S.; Nicoletti, V.; Carbonari, S.; Gara, F.; Leonardo, C.; Leoni, G. SHM of Historical Buildings: The Case Study of Santa Maria in Via Church in Camerino (Italy). *Procedia Struct. Integr.* **2023**, *44*, 2098–2105. [CrossRef]
23. Lobianco, A.L.; Zoppo, M.D.; Ludovico, M.D. Correlation of Local and Global Structural Damage State for SHM. *Procedia Struct. Integr.* **2023**, *44*, 910–917. [CrossRef]
24. Li, J.; Hao, H. Substructure Damage Identification Based on Wavelet-Domain Response Reconstruction. *Struct. Health Monit.* **2014**, *13*, 389–405. [CrossRef]
25. Li, J.; Hao, H.; Lo, J. Structural Damage Identification with Power Spectral Density Transmissibility: Numerical and Experimental Studies. *Smart Struct. Syst.* **2015**, *15*, 15–40. [CrossRef]
26. Ziaja, D.; Nazarko, P. SHM System for Anomaly Detection of Bolted Joints in Engineering Structures. *Structures* **2021**, *33*, 3877–3884. [CrossRef]
27. InComEss. Available online: https://www.incomess-project.com (accessed on 29 January 2024).
28. Pracucci, A.; Vandi, L.; Belletti, F.; Melo, A.R.A.; Vlachos, M.; Amditis, A.; Calcagni, M.T.; Esteves, D.S. Integration of Piezoelectric Energy Harvesting Systems in Building Envelope for Structural Health Monitoring with Fiber Optic Sensing Technology. *Preprints* **2024**, 2024031168. [CrossRef]
29. Tommasino, D.; Moro, F.; De Pablo Corona, E.; Vandi, L.; Baietta, A.; Pracucci, A.; Doria, A. Optimization of a Piezoelectric Wind-Excited Cantilever for Energy Harvesting from Facades. In *Advances in Italian Mechanism Science*; Niola, V., Gasparetto, A., Quaglia, G., Carbone, G., Eds.; Mechanisms and Machine Science; Springer International Publishing: Cham, Switzerland, 2022; Volume 122, pp. 848–856. ISBN 978-3-031-10775-7.
30. Ye, X.-W.; Su, Y.-H.; Xi, P.-S. Statistical Analysis of Stress Signals from Bridge Monitoring by FBG System. *Sensors* **2018**, *18*, 491. [CrossRef]
31. Zhou, Z.; Ou, J. Development of FBG Sensors for Structural Health Monitoring in Civil Infrastructures. In *Sensing Issues in Civil Structural Health Monitoring*; Ansari, F., Ed.; Springer: Dordrecht, The Netherlands, 2005; pp. 197–207.
32. Čápová, K.; Velebil, L.; Včelák, J. Laboratory and In-Situ Testing of Integrated FBG Sensors for SHM for Concrete and Timber Structures. *Sensors* **2020**, *20*, 1661. [CrossRef] [PubMed]
33. Mieloszyk, M.; Majewska, K.; Zywica, G.; Kaczmarczyk, T.Z.; Jurek, M.; Ostachowicz, W. Fibre Bragg Grating Sensors as a Measurement Tool for an Organic Rankine Cycle Micro-Turbogenerator. *Measurement* **2020**, *157*, 107666. [CrossRef]
34. Gomasa, R.; Talakokula, V.; Kalyana Rama Jyosyula, S.; Bansal, T. A Review on Health Monitoring of Concrete Structures Using Embedded Piezoelectric Sensor. *Constr. Build. Mater.* **2023**, *405*, 133179. [CrossRef]
35. Lei, Y.-J.; Li, R.-J.; Zhang, L.-S.; Hu, P.-H.; Huang, Q.-X. Optical Accelerometers for Detecting Low-Frequency Micro-Vibrations. *Appl. Sci.* **2022**, *12*, 3994. [CrossRef]

36. Lee, H.; Oh, M.; Seo, J.; Kim, W. Seismic and Energy Performance Evaluation of Large-Scale Curtain Walls Subjected to Displacement Control Fasteners. *Appl. Sci.* **2021**, *11*, 6725. [CrossRef]
37. Aiello, C. In-Plane Seismic Response of a Glazed Curtain Wall: Full-Scale Laboratory Test and Non-Linear Modelling. In Proceedings of the 7th International Conference on Computational Methods in Structural Dynamics and Earthquake Engineering (COMPDYN 2019), Crete, Greece, 24–26 June 2019; Institute of Structural Analysis and Antiseismic Research School of Civil Engineering National Technical University of Athens (NTUA) Greece: Crete, Greece, 2019; pp. 269–281.
38. *EN 14019:2016*; Curtain Walling—Impact Resistance—Performance Requirements. Slovenski Inštitut za Standardizacijo: Ljubljana, Slovenia, 2016. Available online: https://standards.iteh.ai/catalog/standards/cen/1bfe4fa0-6bf4-4ae7-b2a2-0a87ced89e0d/en-14019-2016 (accessed on 12 February 2024).
39. La Norma Uni En 12600: Prova Del Pendolo–Metodo Della Prova Di Impatto E Classificazione Per Il Vetro Piano. Available online: https://www.ingenio-web.it/files/guida-alle-norme-tecniche-del-vetro-per-edilizia.pdf (accessed on 9 February 2024).
40. NI-9234 Specifications—NI. Available online: https://www.ni.com/docs/en-US/bundle/ni-9234-specs/page/specs.html (accessed on 13 March 2024).
41. HBK (Hottinger, Brüel & Kjær). QuantumX MX840B Universal Amplifier. Available online: https://www.hbm.com/en/2129/quantumx-mx840b-8-channel-universal-amplifier/?product_type_no=QuantumX%20MX840B/MX440B:%20Universal%20Data%20Acquisition%20Module (accessed on 9 February 2024).
42. *UNI BS EN 12152_2002*; Facciate Continue Permeabilità All'aria Requisiti Prestazionali e Classificazione. 2003.
43. *UNI EN 12153:2002*; Facciate continue-Permeabilità all'aria-Metodo Di Prova. 2002.
44. *UNI BS EN 12154_1999*; Curtain Walling—Watertighness-Performance Requirments and Classification. 1999.
45. *UNI EN 12155:2002*; Facciate Continue-Tenuta All'acqua-Prova Di Laboratorio Sotto Pressione Statica. 2002.
46. *UNI EN 12179:2002*; Facciate Continue-Resistenza al Carico Del Vento-Metodo Di Prova. 2002.

*energies*

MDPI

*Article*

# Integration of Piezoelectric Energy Harvesting Systems into Building Envelopes for Structural Health Monitoring with Fiber Optic Sensing Technology

**Alessandro Pracucci [1,2,*], Laura Vandi [1], Francesco Belletti [1], Amanda Ramos Aragão Melo [3], Marios Vlachos [4], Angelos Amditis [4], Maria Teresa Calcagni [5] and David Seixas Esteves [3]**

1 Focchi S.p.A., 47824 Poggio Torriana, Italy; l.vandi@focchi.it (L.V.); f.belletti@focchi.it (F.B.)
2 Levery s.r.l. Società Benefit, 47814 Bellaria Igea Marina, Italy
3 CeNTI—Centro De Nanotecnologia E Materiais Tecnicos, Funcionais E Inteligentes, 4760-034 Vila Nova de Famalicão, Portugal; amelo@centi.pt (A.R.A.M.); desteves@centi.pt (D.S.E.)
4 ICCS—Institute of Communication and Computer Systems, 15773 Athens, Greece; marios.vlachos@iccs.gr (M.V.); a.amditis@iccs.gr (A.A.)
5 Department of Industrial Engineering and Mathematical Sciences, Università Politecnica delle Marche, 60126 Ancona, Italy; m.t.calcagni@pm.univpm.it
* Correspondence: a.pracucci@focchi.it or a.pracucci@levery.it

**Abstract:** This paper presents a study about the integration of Piezoelectric Energy Harvesting Systems (PE-EHSs) into building envelopes for powering Fiber Bragg Grating (FBG) sensors, enabling efficient and low-consumption monitoring with the objective of leveraging structural health monitoring (SHM). The research includes preliminary tests conducted in a real environment to validate the PE-EHS when fully integrated into a ventilated façade, capturing mechanical vibrations generated mainly by wind loads. Based on these activities, the final configuration of PE-EHSs is defined to provide a complete system for façade monitoring. This integrated system includes the piezoelectric generator (PEG), supercapacitor (SC), Power Conditioner Circuit (PCC), Fiber Optic Sensing (FOS) interrogator, and the IoT gateway transmitting measurement data within an Internet of Things (IoT) monitoring platform. This configuration is tailored to address the challenges related to the structural integrity of building envelopes. Results demonstrate a potential for a stand-alone solution in the façade sector but raise issues for certain limitations, requiring further investigation. In particular, the study emphasizes constraints related to the energy production of PE-EHSs for façade integration. It highlights the necessity to carefully consider these limitations within the broader context of their applicability, providing insights for the informed deployment of piezoelectric energy harvesting technology in building envelope monitoring.

**Keywords:** piezoelectric energy harvesting systems; structural health monitoring; fiber Bragg grating sensors; building envelopes; façade integration; energy production; stand-alone system



**Citation:** Pracucci, A.; Vandi, L.; Belletti, F.; Melo, A.R.A.; Vlachos, M.; Amditis, A.; Calcagni, M.T.; Esteves, D.S. Integration of Piezoelectric Energy Harvesting Systems into Building Envelopes for Structural Health Monitoring with Fiber Optic Sensing Technology. *Energies* **2024**, *17*, 1789. https://doi.org/10.3390/en17071789

Academic Editors: Umberto Berardi and Francesc Pozo

Received: 6 February 2024
Revised: 14 March 2024
Accepted: 28 March 2024
Published: 8 April 2024



## 1. Introduction

The smart built environment is an increasing topic within the industry sector capable of enabling dynamic control and operation in buildings, thanks in particular to a data-driven approach to building environments using the Internet of Things (IoT) [1–5] to enable the so-called intelligent building [6]. Within the EU, the adoption of smart solutions is collaborating in the construction market to achieve strategic results defined by European strategies, policies, and directives [7–11] for smart operations in the building, increasing the capability to collect data in order to adopt actions about energy optimization, comfort deployment, and overall efficient building management [12,13]. The integration of smart components raises an issue related to their energy demand within the building, and the adoption of renewable energy sources within buildings has gained significant traction in achieving

energy independence and sustainability at the building scale [14]. Building microgrids and nanogrids are emerging as key solutions for managing and utilizing renewable energy sources within building environments, enabling the integration of diverse renewable energy sources, such as solar photovoltaics (PVs), wind turbines, and micro-hydropower systems, alongside traditional grid connections and energy storage solutions [15–17]. Intelligent buildings integrated with renewable resources are the trend of next-generation buildings, along with the necessity to manage energy load capacity, which refers to the maximum amount of electrical power a building can safely draw from the grid at any given time. Traditionally, buildings relied solely on the main grid, leaving them vulnerable to power outages and limited control over energy costs, but microgrids offer a promising solution for smart buildings. These localized power systems combine diverse renewable energy sources, such as solar panels and wind turbines, with energy storage systems. By integrating these resources, microgrids can significantly reduce reliance on the main grid, enhancing energy security and potentially lowering costs. Several studies highlight the synergy between smart buildings and microgrids, highlighting the challenges of designing microgrids for buildings and emphasizing the need to balance local load capacity and renewable energy sources. The potential of even smaller nanogrids for smart buildings within the broader context of smart cities is gaining space [15], underlining the continuous development of innovative solutions for managing energy load capacity and promoting the integration of renewable energy sources into smart buildings. In this scenario, the integration of renewable resources into intelligent buildings aligns with the growing interest in utilizing microgrids for energy efficiency and savings in intelligent buildings. However, unlike traditional transmission or distribution networks, intelligent buildings with microgrids face unique challenges due to the uncertainties and uncontrollable nature of renewable energy sources like wind turbines and photovoltaic arrays. Their output depends heavily on factors like temperature, solar radiation, and wind speed. In this scenario, while balancing renewable energy sources at the building scale with microgrids and energy grids is a well-established scenario [18–20], the smart component with IoT embedded in building products addresses self-powered solutions adopting energy harvesting [21–23]. In this context, the role of active modules in providing building envelopes with capabilities is a path of research widely researched within smart building components [24–27], and the role of energy harvesting can boost their adoption. The façade integration of smart components can include components such as shading, actuators for openable vents supplied by the building energy system and connected to the Building Management System (BMS), but also active technology such as PVs or solar collectors, as well as IoT, sensors, and AI edge solutions. While active components require a relevant amount of energy for their powering and the connection to the building grid and its renewable energy sources is mandatory, the integration of IoT, sensors, and AI embedded into the façade opens the research to market analysis for the development of systemic solutions capable of providing self-powered systems capable of reading data, providing data, and analyzing these data for users' utilization. In this frame, it appears to be an opportunity for the exploitation of energy harvesting solutions in the façade. Although multiple projects have investigated this goal using Building Integrated Photo Voltaic (BIPV) products [28,29] in particular, the introduction of energy harvesting based on Piezoelectric Energy Harvesting Systems (PE-EHSs) can represent a valuable option for building envelope integration. The scientific community has deeply investigated piezoelectric cantilevers, even for smart building applications [30–32]. However, the adoption of a PE-EHS cantilever in the façade is a challenge that needs to be further addressed. Indeed, based on the exploitation of the wind load and rain drops [33–35], its applicability has demonstrated some limitations due to energy constraints and overall architectural limitations and integration [36–39]. This paper presents alternative solutions investigated to integrate PE cantilevers into building envelopes with the purpose of validating their ability to function effectively even under challenging environmental conditions, such as the unstable and non-parallel airflow patterns commonly encountered within building façades. By addressing these non-ideal boundary conditions, this study aims to broaden

the applicability of piezoelectric energy harvesting in the context of smart buildings, paving the way for a more robust and versatile approach to self-powered building components.

The utilization of energy harvesting from piezoelectric cantilevers opens an opportunity for self-powered monitoring systems. In recent years, the utilization of sensing technologies to address structural health monitoring (SHM) for civil construction has emerged [40], and it is also moving to building applications, thanks to the versatility of the sensing technologies adopted [41–43]. With a focus on building envelopes, the importance of integrating sensors into façades lies in the opportunity to provide data about physical parameters useful for addressing actions for building maintenance for high-rise buildings that are exposed to more stressful conditions. The introduction of embedded sensors within building envelopes for SHM guarantees continuous monitoring, and the utilization of miniaturized technologies such as fiber optic sensors (FOSs) using specific Fiber Bragg Grating (FBG) to collect data [44] can represent an opportunity to have small-size and low-energy-consumption technology embedded.

In line with this research scenario, one of the targets of the EU-funded InComEss project [45] is to develop and evaluate the performance of the PE-EHS to harness its energy production for the energy supply of a structural health monitoring system by integrating FBG/FOS. The InComEss system architecture aims to exploit the PE-EHS to supply energy to an FOS monadgator, which reads FBG data and communicates with a Power Conditioner Circuit (PCC) integrated with a Printed Circuit Board (PCB) powered by a local supercapacitor (SC). The PCC/PCB is connected via an IoT gateway to a cloud-based Internet of Things (IoT) monitoring platform for data collection and analysis. The goal is to demonstrate the feasibility of wireless sensor networks (WSNs) for SHM. Within the overall project expected results, the paper presents the results achievable by the PE-EHS within the overall InComEss system for contributing to the scientific scenario in support of analysis useful for establishing a stand-alone solution for structural health monitoring of façades using low-consumption sensing technology-based fiber optic sensors and the associated low-power wireless interrogator. The research aims to integrate piezoelectric cantilevers into building envelopes, ensuring both technological and architectural integration. The primary advancement within the scientific framework is to investigate whether piezoelectric cantilevers can effectively operate as energy harvesters for smart components within building envelopes, even under challenging conditions, such as unstable and non-parallel airflow, and considering architectural limitations, such as fully embedded and non-visible integration required by the market, which are typical boundary conditions for façades.

The paper is structured as follows: Section 2 outlines the methods used for the identification of PE-EHS configurations and the InComEss system architecture, along with the tests conducted for validation. Section 3 presents the outcomes from preliminary testing activities to the final laboratory test, displaying collected data and graphical representations for PE-EHSs and overall InComEss system architecture validation. Section 4 highlights the successful aspects of PE-EHSs and the InComEss system architecture while also addressing gaps identified due to research and test limitations. Section 5 summarizes the main achievements related to the paper's goal of analyzing EH-PHS opportunities in supporting SHM sensor systems as stand-alone solutions and suggests future directions for in-depth investigations leading to marketable solutions.

## 2. Materials and Methods

This section outlines the methods and materials adopted for the implementation of the research activities presented in this paper.

The methods are focused on the stages deployed for the PE-EHS configurations within the InComEss system architecture with the following development stages:

- Analysis and design of the InComEss architecture system and components for integration into the façade—The InComEss system architecture is composed of a set of components analyzed to understand the impact of façade integrability. PE-EHS, FBG along FOS, FOS monadgator, PCC/PCB, and supercapacitor are the physical

components to be embedded in the façade. Additionally, the digital component, represented by the IoT gateway for data gathering and transmitting in the IoT platform, is analyzed for its design for façade structural health monitoring. The aim is to adapt and integrate the InComEss architecture within the façade components and relative requirements. This paper underlines the study of PE-EHSs. An in-depth investigation of possible applications within the façade's components is carried out to define the possible configuration of PE-EHSs, considering several key factors, including aesthetic considerations to ensure visual integration, energy efficiency for sustainable performance, replicability for widespread application, and maintenance considerations to facilitate long-term functionality and ease of upkeep. Multiple distinct configurations are developed with the primary objective of identifying the optimal integration for the façade system;

- Preliminary PE-EHS testing activities—The PE-EHS configurations designed are tested preliminarily in small real environments with the objective of analyzing their voltage production and defining the PE-EHS configurations for the ventilated façade integration. The comprehensive evaluation of these tests addresses the final configuration and specific testing activities to be developed in a controlled lab environment;
- Final PE-EHS configurations and tests in a laboratory of the InComEss architecture system—The PE-EHS final configurations are identified. Testing activities in the controlled lab environment include collecting voltage data for analysis of piezoelectric energy production and overall system performance to identify the results achievable by the overall system in different façade stress conditions. The InComEss architecture system's components (PE-EH, FBG-FOS, PCC/PCB, IoT gateway, and IoT platform) are validated individually and together to evaluate the stand-alone system reliability. In particular, the PCC circuit's capability to charge the supercapacitor is tested based on the voltage generated by the PE-EHS integrated into the ventilated façade. The FOS monadgator power consumption is monitored during testing activity. The air velocity employed in the tests during laboratory activities is chosen to reflect the typical wind load forces experienced by high-rise buildings, which serves as the primary reference point for this research. Initial tests using a fan within a range of 5 m/s to 8 m/s are conducted to identify a suitable minimum air velocity. Ultimately, a minimum velocity of 5 m/s is adopted for subsequent testing. Furthermore, to ensure consistency with standardized practices and serviceability of the façade, the wind load range during the experiments corresponds to air velocities ranging from 9.03 m/s to 31.30 m/s. These values align with the specifications outlined in the EN 13830 standard [46], which governs test service conditions for façades. By adhering to this established standard, the obtained results maintain relevance and applicability to real-world building environments;
- Results and test analysis—The laboratory tests for the PE-EHS are analyzed based on testing conditions to comprehend the piezoelectric configuration's potential for voltage generation. The InComEss system and its integration into the façade are analyzed to wrap up potentialities and limitations for the application. For the lab test, knowing this voltage (U) and the capacitance (C), the stored energy (E) generated by the PE-EHS is calculated as follows:

$$E = \frac{1}{2} C U^2,$$

hence, for time (t) t = 1 s, the value of time, the power (P) will be

$$P = \frac{E}{t} \quad (1)$$

The results achieved for different configurations are compared for the voltage generated and reported. The primary challenge encountered by the piezoelectric cantilever is the generation of an electrical current in the nanoampere (nA) range, which poses significant

difficulties for measurement using a PCB. Consequently, the output voltage is utilized as a benchmark for comparison.

The materials adopted for the research activities are as follows:

- InComEss components—The research is based on component development within the project [45]:
  - A PE patch [47,48] is a Macro-Fiber Composite (MFC) PZT, model M8514P2, with a dimension of 18 × 100 mm bonded to a substrate carrier beam made of 1 mm ($t_b$) FR-4 made by glass-reinforced epoxy laminate material and with a dimension of 35 × 110 mm ($W_b \times L_b$). The bluff body is a hollow cylinder made of a polymeric material with a diameter of 10 mm ($D_f$) and a length of 70 mm ($L_c$). The InComEss system architecture's energy generation is achieved by integrating a piezoelectric cantilever, constructed from Poly(vinylidene fluoride (PVDF) tapes, into a façade. Given the challenge of inducing significant deformation through vibration alone on a piezoelectric patch with dimensions of 18 cm in length and 5 cm in width, a polymeric wheel designed to rotate with wind is developed and subjected to simulation. The strategy entails attaching permanent magnets to both the wheel and the piezoelectric cantilever, leveraging magnetic repulsion to induce deformation as the wheel turns under typical direct wind conditions (2–5 m/s). The design process utilizes SolidWorks for the wheel's conception, while Ansys is employed for simulation purposes, with the goal of maximizing output voltage. Through initial analysis and simulation, several solutions are validated, including the reduction in blade inclination from 45° to 30°, the integration of an air channel within the façade's ventilated cavity to focus airflow and enhance the initial force generated, and the reduction in the wheel's weight to enable its activation by lower air pressures. These adjustments are implemented and tested on the cantilevers to determine their impact. For the development of the piezoelectric tapes used on the cantilever, PVDF homopolymer pellets, specifically Kynar 720 from Arkema, are converted into tapes using a twin-screw extruder coupled with a flat die. After that, silver ink is applied to both sides of the tapes to create electrodes. The tapes were then poled using a DC power supply to achieve a target piezoelectric coefficient (d33) of up to 20 pC/N. After polarization, the tapes are aligned on a fiberglass composite to construct the piezoelectric generator, with the aim of optimizing the mechanical-to-electrical energy conversion efficiency. The output voltage, both in laboratory and real-world conditions, is measured to evaluate the piezoelectric performance of the developed PVDF cantilever and wheel, utilizing different energy measuring systems for voltage (reported in the Section 2). These output voltages serve as a basis for comparison because, for the façade integration, a dedicated PCB is developed, which is solely capable of voltage acquisition. Consequently, the output voltage provides a comparative analysis between the ideal scenario (laboratory conditions) and the real-world simulation on a ventilated façade;
  - An FOS monadgator based on a low-energy-consumption solution to data gathering and transmission of the InComEss system architecture is used. The FOS monadgator-powered consumption is measured for a full cycle (start-up, FBG data collection, data transfer);
  - A supercapacitor based on the screen-printing method with a capacitance of 125 mF and a voltage of 5 V is used. The equivalent series resistance (ESR) of this module is 26 Ohm;
  - A PCB/PCC is used to have all the components integrated and communicate with each other. The Power Conditioning Circuit is composed of a rectifier to transform the alternate voltage of the piezoelectrics into a direct current and an actively controlled switched regulator to convert the voltage into a usable value. The load resistance is variable since the PCC is powering an active circuit.

There is a minimum voltage needed to start harvesting energy; below that threshold, the PCC does not operate. Based on in-field data analysis, a current of ~4 mA is necessary to reach a ~5 V threshold to charge the supercapacitor, and consequently, the resistance is R = U/I = 5 V/0.004 A = 1250 Ohm. The PCC needs a power of 20 mW to run. No more technical information can be disclosed due to confidentiality issues;
    - An IoT gateway, which has been recently proposed for a real-time vehicle monitoring application [49], is customized to support the integration with the FOS node for data collection and transmission to the IoT platform;
    - An IoT platform is customized for façade structural health monitoring, visualization, exploring, and alerting.
- Energy measuring system for voltage:
    - For configurations A1, A2, and C2 in a real environment at Focchi premises, a custom-built data acquisition system specifically designed for the project is used. The system consists of a low-voltage drop diode bridge rectifier that converts the AC that usually comes from the PEG into a DC voltage. This DC voltage is used to charge up a low-leakage foil capacitor. The rising voltage across this capacitor is measured using a very-high-input impedance op amp so that no discharging effect as a result of the measurement chain occurs. No more technical information can be disclosed due to confidentiality issues;
    - For configuration D in a real environment at CENTI premises, a BK Precision 2194 oscilloscope is used;
    - For configuration D in lab tests, a data-logger Keysight 34907A with 16 bits of digital input and output, 3 active channels, and 7 Hz for the channel is used.
- Prefabricated façade—A unitized façade system for a multifactional façade is selected [25] to improve solutions in the same product development;
- Test activities and method statement—In preliminary test activities, real conditions in a small environment or wind velocity generated by a fan of 2–3 m/s are used. In the laboratory tests, a specific method statement is adopted based on stress conditions of the façade using wind airflow and rain forces; see Appendix A. The tests are conducted with a fan at 600 mm and with nozzles simulating rain in correspondence with façade joints with a continuous flow rate of 2 l/min·sqm and at 400 mm from the façade. The PE-EHS is situated behind the façade cladding, replicating its intended integration within a ventilated façade system. While wind load conditions are adopted to check the PE-EHS voltage generated by airflow within the chamber, the rain exposure induces vibrations in the external cladding, exploiting this dynamic interplay between rain-induced vibrations in the cladding and the PE-EHS, in addition to utilizing the airflow within the ventilated cavity. To simulate rain within the controlled laboratory environment, a system employing a series of nozzles corresponding to the typical joint locations in a façade is utilized. Two types of rain tests are conducted:
    - Dynamic Rain Test: This test simulates wind gusts by generating pulsating pressure variations every 3 s. The pressure fluctuates between 750 Pa and 250 Pa, mimicking the dynamic nature of wind-induced pressure changes;
    - Static Rain Test: This test aims to understand the behavior under constant rain conditions. A constant pressure of 600 Pa is maintained throughout the test duration.

These simulated rain tests provided valuable insights into the performance of the PE-EHS under conditions representative of real-world façade scenarios, complementing the wind tunnel and airflow-based testing.

## 3. Results

### *3.1. Preliminary PE-EHS Configurations and Tests*

Based on the InComEss system architecture conceptualization (Figure 1) and façade integration purposes, the PE-EHS cantilever was designed to demonstrate its integrability within a prefabricated ventilated façade.

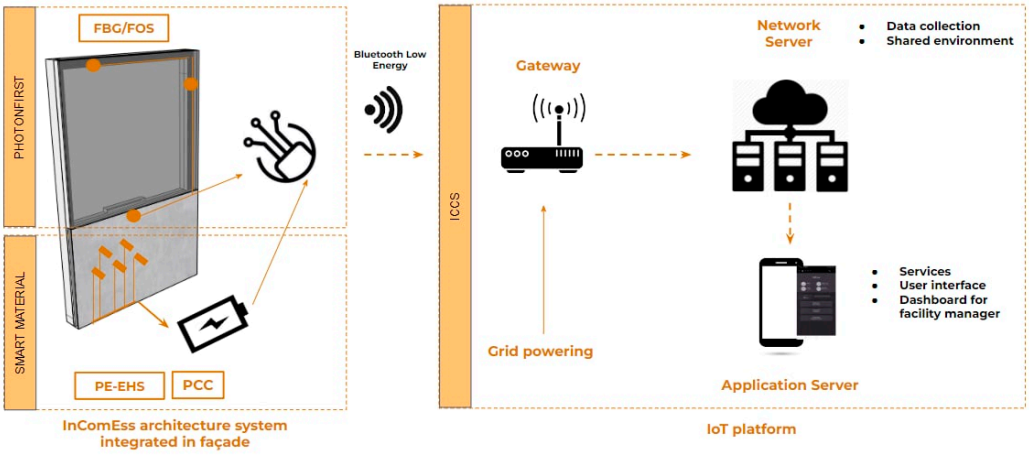


**Figure 1.** Scheme of InComEss system architecture with components integrated into façade and communication to IoT platform.

The ventilated façade [50,51] is a building envelope system that consists of a double-layered wall with an air cavity separating an outer cladding layer from the main building structure. This air cavity allows for natural ventilation, facilitating the circulation of air within the cavity and removing heat build-up during warm seasons. In colder climates, the air cavity acts as an additional layer of insulation, reducing heat loss and improving building energy efficiency. Beyond their thermal benefits, ventilated façades enhance acoustic insulation, dampening external noise and contributing to a more comfortable indoor environment. Additionally, the outer cladding provides aesthetic appeal, offering architects a broader design palette for creating striking and visually appealing building exteriors. Furthermore, ventilated façades can improve durability by protecting the primary wall from harsh weather conditions, extending the building's lifespan and reducing maintenance needs. The PE-EHS cantilevers are strategically positioned within the cavity; they can harness ambient wind-induced vibrations or pressure fluctuations to generate electricity. The design of these integrated cantilevers requires analysis of various factors. The placement and orientation of the cantilevers optimized to maximize exposure to these vibrations while ensuring structural integrity and aesthetics within the façade design are presented here.

The airflow entering the ventilated façade cavity plays a critical role in the functionality of the integrated piezoelectric cantilevers. Ideally, the airflow should possess certain characteristics to optimize energy harvesting, such as sufficient velocity with a minimum wind speed that is necessary to generate meaningful vibrations in the cantilevers, enabling them to produce a usable amount of electricity or stability and directionality due to the fact that turbulent or non-parallel airflow patterns can significantly reduce the efficiency of energy harvesting. Therefore, understanding the behavior of the airflow entering the ventilated cavity is essential for designing and optimizing the integration of piezoelectric cantilevers. Figure 2 shows the behavior at different airflow velocities to the façade (2.5 m/s and 10 m/s) of the airflow within the ventilated cavity. The model demonstrates that the airflow inside the ventilation space remains consistently laminar, presenting an opportunity to maintain a constant frequency in the vibration of PE-EHS cantilevers. Consequently, the PE cantilevers are specifically designed to align with the cavity within the façade.

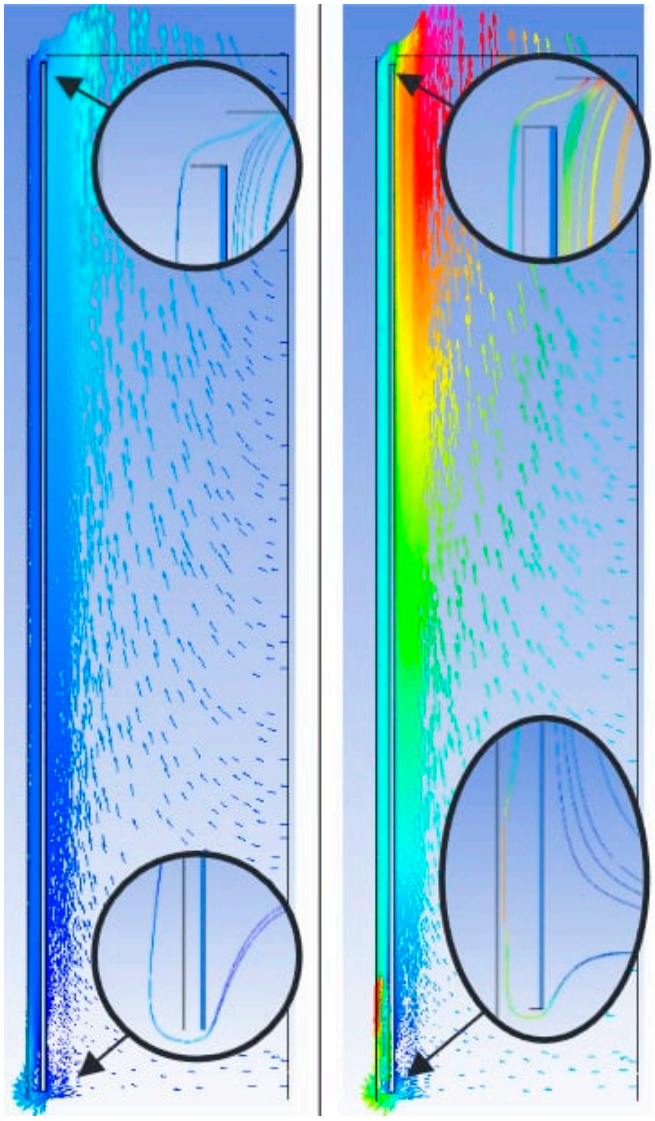

**Figure 2.** Speeds of air inflow simulating the wind [50]: wind at 2.5 m/s in the left; wind at 10 m/s in the right.

The early-stage conceptualization is based on the utilization of PE-EHSs based on cantilever- and vortex-induced vibration [52]. This configuration is founded in the physical field of fluid–structure interaction based on impacting bluff bodies subjected to a continuous flow of fluid; for façade application, the excitation mechanism of the vortex shedding phenomenon is enabled by the wind-induced vibration with vortices periodically shredded from the cylindrical bluff body. This design includes a PLA cylinder at the extremity of the PE, specifically conceived to be responsive to a wind speed of 1.5 m/s. The dimensions of the PE cantilever are 110 × 35 mm, while the designed cylinder features an outer diameter of 10 mm constructed from PLA material. In line with this concept (Figure 3), two configurations have been supposed for façade integrability (Figure 3a,b). While configuration "A1" is more conventional, concerns arise regarding its dimensions for façade integration. The cantilever, with a length of 110 mm, proves challenging to apply seamlessly into a façade. Consequently, an alternative configuration based on a vertical cantilever ("B1") was devised, featuring an overall width of 25 mm, making it more practical for integration into a façade, particularly one with a possible ventilated cavity of 35/40 mm. The consideration of a ventilated cavity stems from an architectural requirement for the complete integration of the PE-EHS within the façade, anticipating the concealment of

the PE-EHS visioning with a cladding material. For this reason, two more configurations have been defined for horizontal cantilever configuration with external cladding "A2" and vertical cantilever configuration with external cladding "B2". These configurations generate energy voltage by directly stimulating the cantilever with the wind flow, creating a vortex effect (configurations "A1" and "B1"), or by harnessing airflow entering the ventilated cavity of the façade (configurations "A2" and "B2").

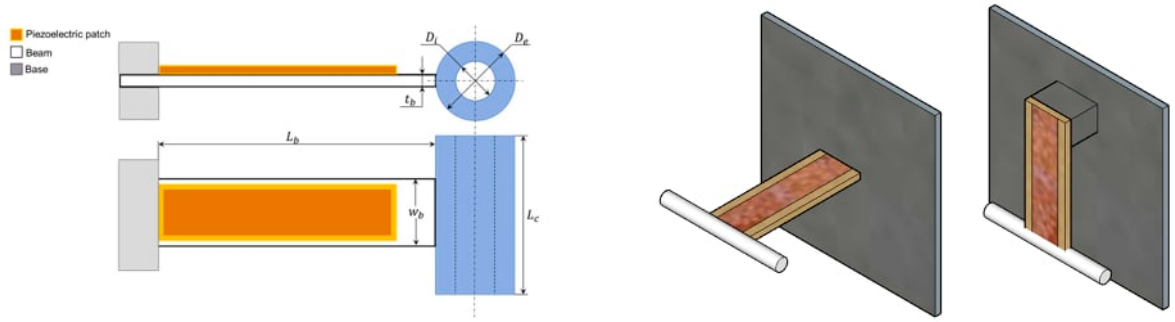


(**a**) (**b**)

**Figure 3.** Drawing of PE-EHS cantilever with cylinder for vortex (**a**). Configuration with horizontal PE cantilever and cylinder "A1" and configuration with vertical PE cantilever and cylinder "B1" (**b**).

The PE-EHS testing beds (Figure 4) were installed in Focchi premises in Italy (coordinates 44.04671, 12.41286) into an existing façade (real environment) at 5 m in height from the ground and with a range of wind direction of 0.5 m/s to 3 m/s monitored by an anemometer installed in the Focchi premise (11 m height) for a period of 2 weeks for each configuration (22 November 2021–04 December 2021, weather data available at [53,54]). Considering days without precipitation, Table 1 reports the average energy produced in a time stamp of 2 h for two different days with a wind velocity average of 2–3 m/s by vertical configuration "A". The results demonstrate a low voltage output from the PE-EHS, which is insufficient to power the FOS monadgator. The results obtained using configuration "B" were even lower and deemed nonrelevant and, therefore, not reported.

(**a**) (**b**)

**Figure 4.** Test beds in Focchi premises for PE-EHS tests for configurations "A" and "B": configurations installed (**a**); measuring system (**b**).

**Table 1.** Average voltage results achieved by PE-EHS "A1" and A2" configurations in one sample day over 2 weeks of testing with a wind range of 0.5 m/s to 3 m/s.

| PE-EHS "A1" Configuration | | PE-EHS "A2" Configuration | |
|---|---|---|---|
| **Time** | **PE Voltage [V]** | **Time** | **PE Voltage [V]** |
| 8:00 | 0.5476 | 8:00 | 0.5094 |
| 10:00 | 0.5473 | 10:00 | 0.3357 |
| 12:00 | 0.5449 | 12:00 | 0.5380 |
| 14:00 | 0.5442 | 14:00 | 0.5191 |
| 16:00 | 0.5419 | 16:00 | 0.4768 |
| 18:00 | 0.5417 | 18:00 | 0.5283 |

Based on the results obtained using configuration "B" but considering the integration into the façade's small cavity to be crucial for the InComEss architecture, an additional set of configurations was designed (Figure 5). These configurations were designed to investigate the chance of adopting the PE-EHS in a small cavity by harnessing not only the airflow entering the ventilated cavity of the façade but also the wind load on a façade's cladding realized in a metal sheet of 30/10 mm to exploit the related frequency of vibration.

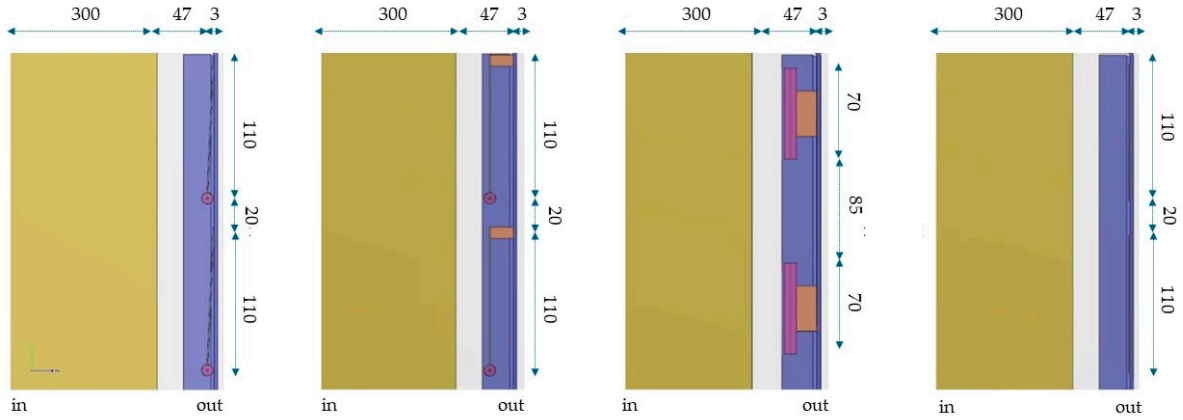


**Figure 5.** Set of possible configurations for the external cladding: PE-EHS vertical cantilever directly installed in the cladding (**a**); PE-EHS vertical cantilever distanced by cladding of 10 mm (**b**); PE-EHS horizontal cantilever distanced by cladding of 10 mm (**c**); PE-EHS patch glued at the cladding (**d**). Legend: façade's spandrel; ventilated cavity; cladding; PE-EHS cantilever and attachment block to the cladding; PE-EHS cantilever's cylinder for vortex effect.

The two configurations selected for further investigation that were considered to have a more promising combined effect for harnessing both airflow within the cavity and the vibration of the metal sheet cladding are configurations in Figure 5b, named "C1", and Figure 5c, named "C2". To validate these configurations, the one with the lower potential for electrical energy generation, configuration "C2", was tested in the Focchi premise (Figure 6). The test was conducted by installing a metal sheet cladding in an existing façade at 3 m in height from the ground and with a range of wind direction of 0.5 m/s to 3 m/s for a period of 2 weeks for each configuration (6 June 2023–20 June 2023, weather data available at [55]). Considering days without precipitation, Table 2 reports the average energy produced in a time stamp of 2 h for two different days with a wind velocity average of 2–3 m/s by configuration "C1". Despite the lower voltage output, which is insufficient to directly power the FOS monadgator, the results confirm that PE-EHS configuration "C1" can effectively address façade integration requirements within an air-ventilated cavity.

(**a**) (**b**)

**Figure 6.** Test beds in Focchi premises for PE-EHS tests for configuration "C2": the test bed installation (**a**); detail of the air cavity with PE-EHS installed (**b**).

**Table 2.** Average voltage results achieved by PE-EHS "C2" configuration in one day sample over 2 weeks of testing with a wind range of 0.5 m/s to 3 m/s.

| PE-EHS "C2" Configuration | |
|---|---|
| **Time** | **PE Voltage [V]** |
| 08:00 | 0.6195 |
| 10:00 | 0.6140 |
| 12:00 | 0.6299 |
| 14:00 | 0.6427 |
| 16:00 | 0.6400 |
| 18:00 | 0.6321 |

During the development of the PE-EHS, a paradigm shift was explored based on cantilever stimulation using magnetic forces activated by wheel rotation. The concept involved affixing permanent magnets to both the end of the cantilever and the wheel, thereby inducing a continuous and stable deformation of the cantilever throughout the wheel's rotation. To investigate the concept of using wheel rotation to induce mechanical deformation, multiple different wheel configurations were simulated and tested in CeNTI premises, moving from an initial wheel configuration to the final one (Figure 6). The first configuration was obtained through the adaptation of a typical side windmill. The concept was to gather as much wind as possible, covering the largest area. Due to the sheer size of the structure, the windmill was not capable of jumpstarting with low-velocity winds. With the reduction in size in mind, a four-legged wind blade with a thin support structure in the middle was developed using SolidWorks.

While the theoretical vortex-based cantilever is well established in the literature for its vortex simulation concepts, due to the complexity and innovative nature of this design, a three-dimensional fluid dynamics simulation tool [56] was employed to analyze the airflow patterns around the wheels.

The findings supported the idea that air diversion could effectively increase the force generated by the wheel, but it was necessary to adopt a lighter wheel to be able to start rotating under low wind velocities. To address this weight issue and minimize the risk of airflow stagnation, which could affect the wheel's rotation, a series of iterations were conducted to optimize the number of blades.

Figure 7 demonstrates the effect of wind on both types of wheels. The selected configuration for prototype implementation was configuration "D" (Figure 8b) since it allowed the reduction of the initial configuration's force from 0.268 N/m to the final

configuration's force at 0.160 N/m while reducing the weight from 0.548 Kg to 0.123 Kg. The consequence is that despite the lower force applied by the wind on the surface, the required force to start the turbine is lower due to the reduced weight.

(**a**) (**b**)

**Figure 7.** Wheel configurations designed by CENTI: initial wheel configuration (**a**); final wheel configuration (**b**). Each wheel has an outside diameter of 405 mm.

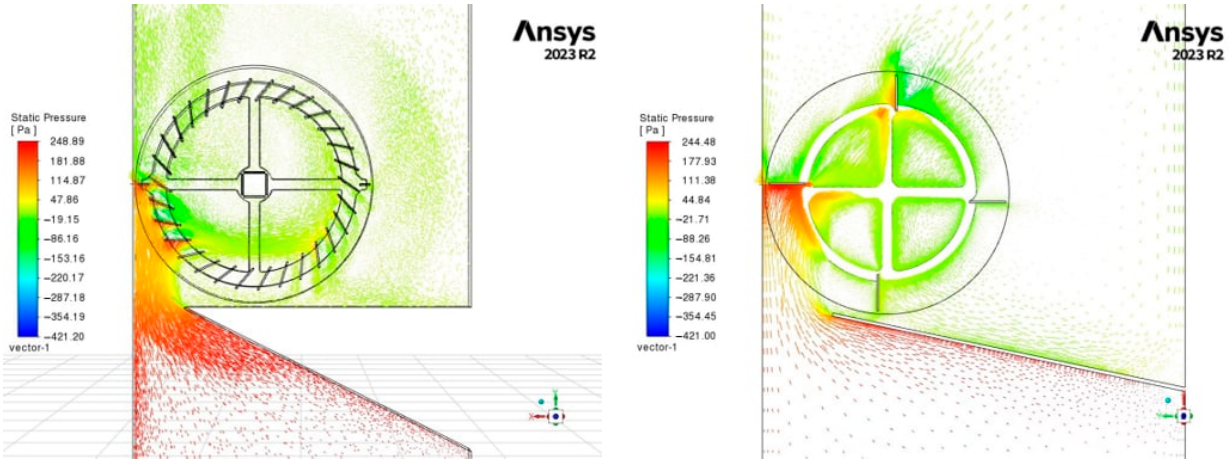


(**a**) (**b**)

**Figure 8.** Wheel rotation analysis activated by a pressure density at a 2 m/s inlet: simulation with initial wheel configuration (**a**); simulation with final wheel configuration (**b**).

The final wheel configuration, "D", (Figure 9) was tested in a wind tunnel setup (airflow minimum 2 m/s in the direction parallel to wheel rotation forces), integrating the PE-EHS cantilever with permanent magnets to overcome the challenges of the blind spot at the tips of both the blades and the cantilever. This setup is based on the utilization of the repulsion and attraction forces between the permanent magnets, along with the elastic properties of the PVDF-based one.

The final wheel configuration was tested in a wind tunnel setup (airflow minimum 2 m/s in the direction parallel to wheel rotation forces), integrating the PE-EHS cantilever with permanent magnets to overcome the challenges of the blind spot at the tips of both the blades and the cantilever. This setup is based on the utilization of the repulsion and

attraction forces between the permanent magnets, along with the elastic properties of the cantilever, to generate continuous motion of the cantilever synchronized with the rotation of the wheel. This design aims to optimize the energy harvesting process by efficiently converting the kinetic energy of wind into electrical energy.

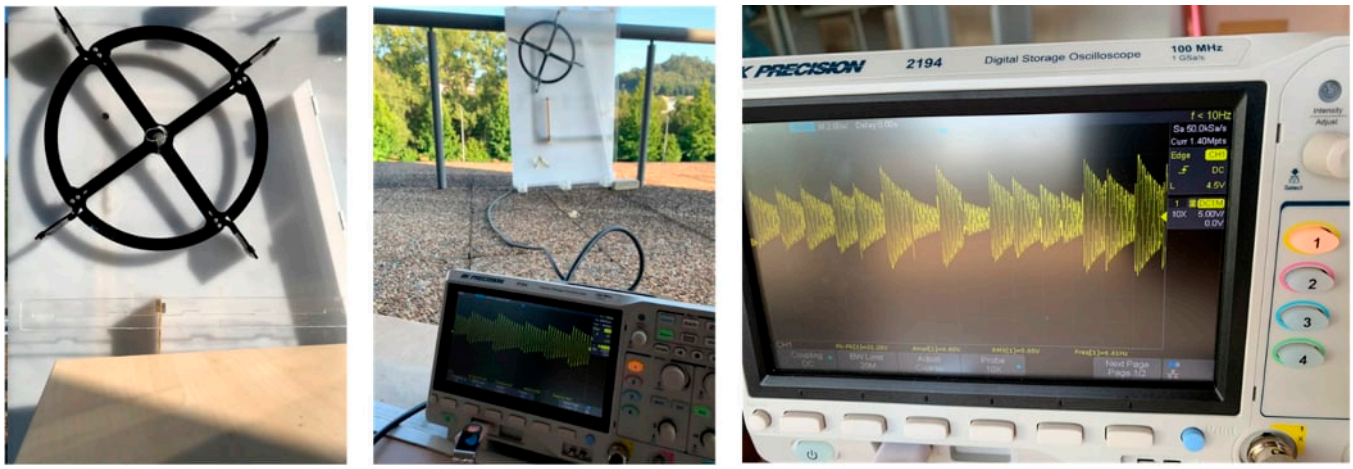


(**a**) (**b**) (**c**)

**Figure 9.** Test beds in Centi premises for PE-EHS tests with wheel configurations: wheel configuration in laboratory (**a**); test bed on Centi roof for real environment test (**b**); wheel configuration voltage results (**c**).

The results demonstrate a peak voltage of 20 V and an average close to 5 V, demonstrating effective operation in controlled laboratory conditions with an airflow from 2 m/s to 5 m/s with wind entering the cavity directly so that airflow is aligning perpendicularly to the blade surfaces. However, the result also showed that in cases where the airflow did not enter the cavity directly, the wheel failed to rotate.

Based on the voltage achieved with the PE-EHS configuration using a wheel, this final configuration is the one adopted in the InComEss system architecture for integration into the façade and for testing in the laboratory under façade stress conditions.

### *3.2. Final PE-EHS Configurations and Tests of InComEss System Architecture*

The PE-EHS wheel configuration was designed and prototyped for integration into the prefabricated façade so as to be part of the InComEss architecture system developed and implemented for the final laboratory tests. The integrability of the wheel was demonstrated during the façade manufacturing stages (Figure 10), allowing for integration into a cavity with a dimension of 60 mm and its proper installation in a laboratory testing facility (Figure 11).

In addition to PE-EHS configuration "D", also the PE-EHS configurations "C1" and "C2" were installed in the façade to collect information in the lab environment about the energy generation from the combined effect already preliminary investigated. For this purpose, an acquisition system for the PE-EHS was specifically set up to collect data about energy voltage production independent of the InComEss architecture (Figure 12).

Before the test commenced, as described in Appendix A, the performance of PE-EHS configuration "D", intended to power the InComEss system, was evaluated. A laboratory fan was positioned at two distances from the air inlet cavity: 1490 mm and 490 mm. The air velocity varied from 5 to 8 m/s. The aim was to assess the achievable performance and determine if the generated voltage was sufficient to power the FOS monadgator. However, the results (Figures 13 and 14) were not promising and showed inconsistencies, with a wide range of variation from 0.05 V to 5 V based on fan air source generation. Consequently, the decision was made to power the InComEss system using the laboratory's local energy grid.

(**a**) (**b**)

**Figure 10.** EP-EHS wheel configuration installed in the façade: metal sheet cladding with an air channel and wheel integrated (**a**); EP-EHS wheel configuration's ventilated air cavity in the façade (**b**).

**Figure 11.** The PE-EHS cantilever, configured within the wheel setup, installed in the façade within a laboratory testing facility. The airflow within the cavity triggers the rotation of the wheel, and the magnets positioned at its extremities generate a magnetic force with the magnet located at the end of the PE cantilever, thereby enabling vibration.

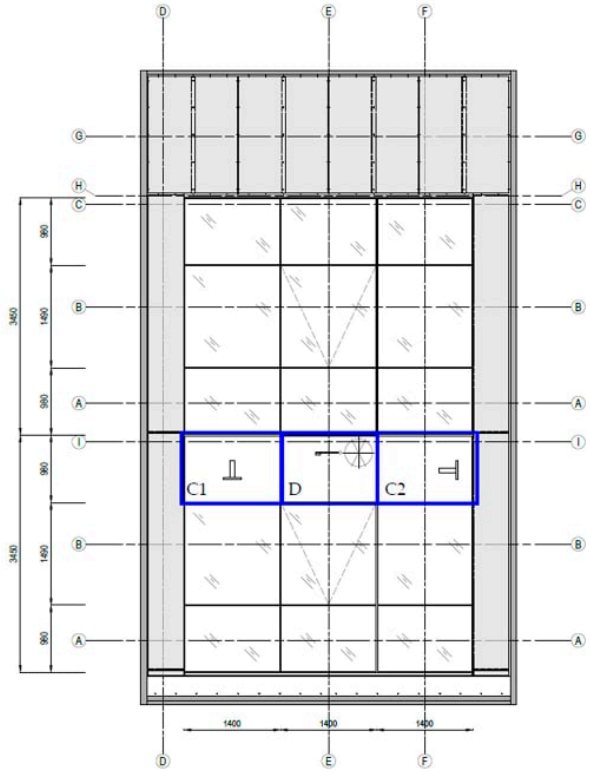


(**a**)

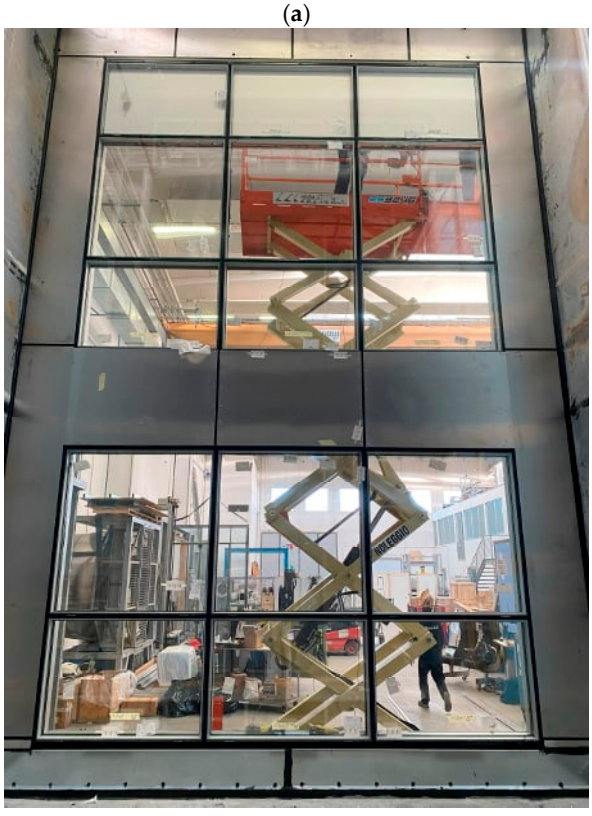

(**b**)

**Figure 12.** The PE-EHS configurations "C1", "C2", and "D" integrating into façade spandrel within ventilated air cavity: façade prototype design for testing in laboratory (**a**); façade prototype ready for testing activity (**b**).

To ensure the proper functioning of the InComEss architecture, a comprehensive testing procedure was conducted to validate each single technology before the overall system functionality testing. The components were individually evaluated using standard equipment, such as multimeters, batteries, and grid energy supply. The PCC was first tested by supplying it with power from the laboratory's local energy supply and with a battery. This activity allowed monitoring of the charging time of the supercapacitor using a multimeter, confirming that the PCC circuit recharged the supercapacitor. Similarly, the monadgator was tested using the external power supply to validate its capability to measure FBG sensors, demonstrating the functionality of both the FBG sensor and the monadgator. Next, the Bluetooth low-energy (BLE) wireless connection between the monadgator and the IoT gateway (ICCS) was evaluated. For this validation, an Arduino Nano, integrated by PHTN into the PCC, facilitated the rapid start-up of the monadgator and execution of FBG wavelength measurements. Thanks to a broadband light source (laser) operating for 70 milliseconds, the FBG sensor was read, and data were acquired by the Arduino. The data were transmitted via BLE to the IoT gateway. The Arduino was powered by the PCC, which was charged using energy harvested from connected energy harvesters. Once the circuit reached sufficient charge, the Arduino initiated FBG sensor measurements via the monadgator. The entire measurement cycle, including wireless data transfer, required less than 150 milliseconds and consumed 0.08 W/s of energy. The measured values were successfully displayed on the gateway's LCD screen, indicating that the BLE connection was operational. Finally, the 4G connection between the gateway and the IoT platform was tested, and its functionality was confirmed (Figure 16).

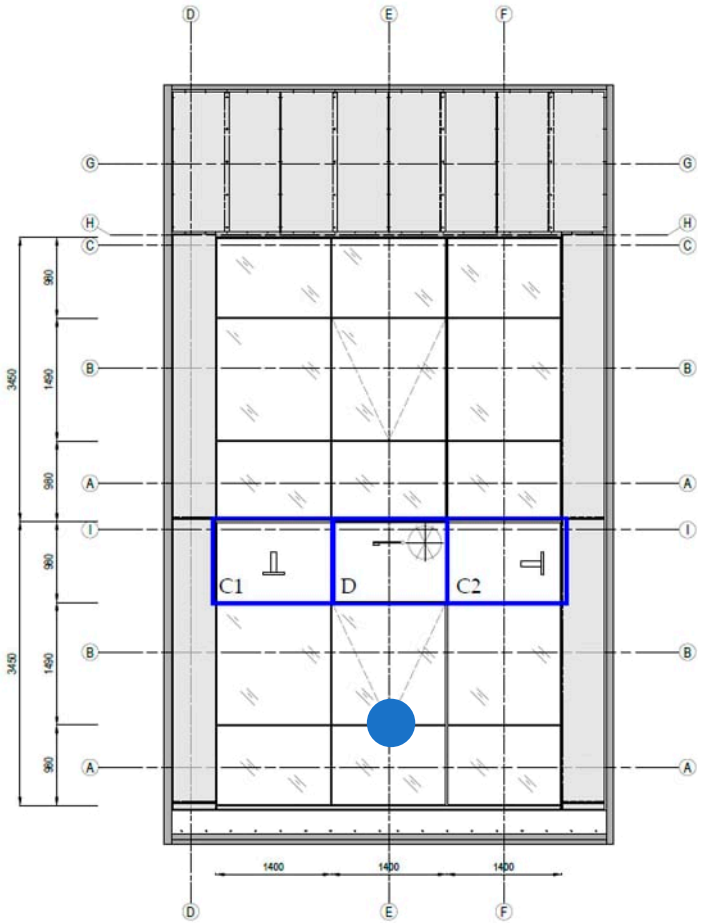


(**a**)

**Figure 13.** *Cont.*

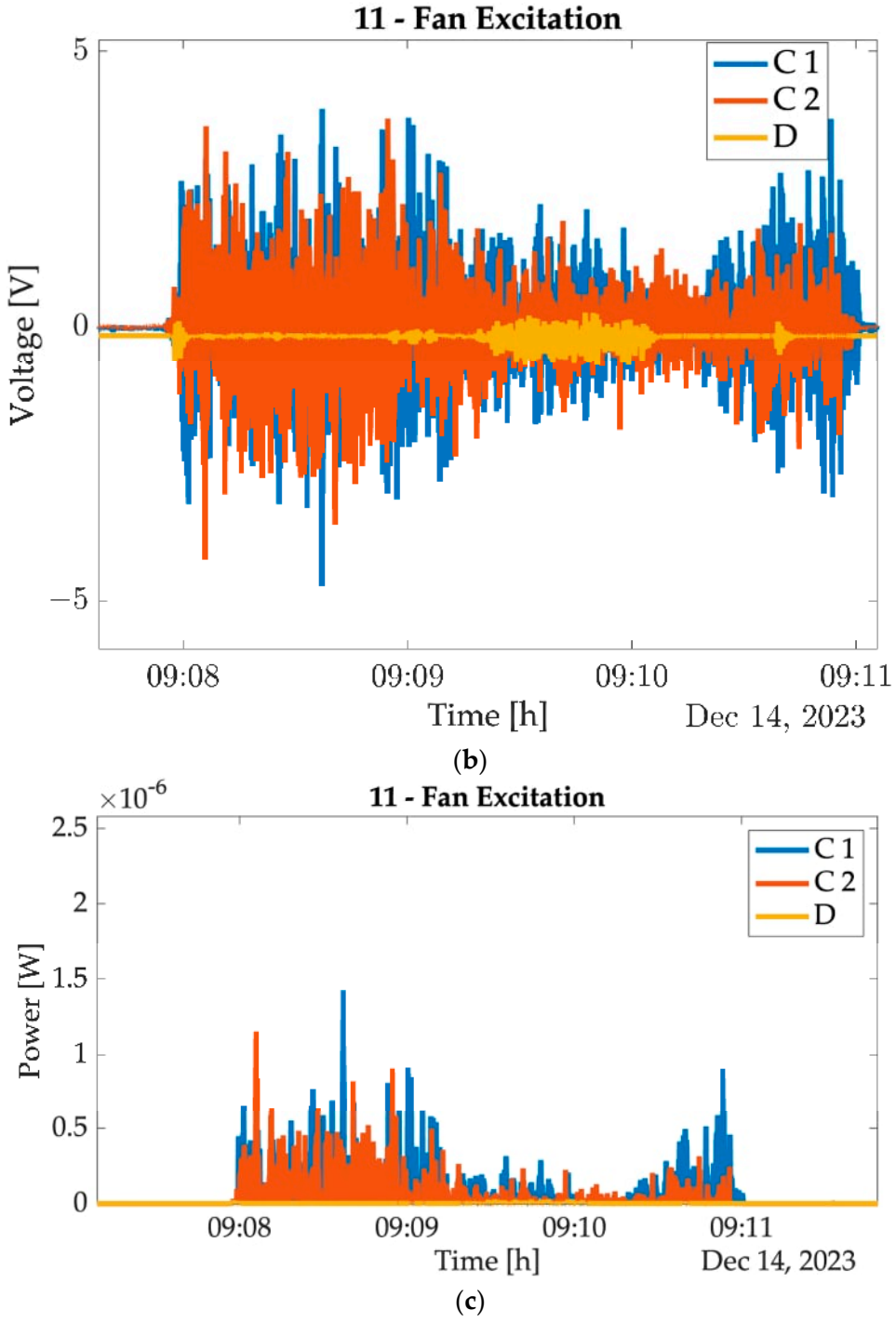


**Figure 13.** Preliminary voltage validation of the PE-EHS wheel configuration installed in the façade in a laboratory testing facility: fan placed at 1490 mm from the cavity inlet with an air velocity from 5 to 8 m/s (**a**); PE-EHS voltage generated (**b**); PE-EHS power generated (**c**).

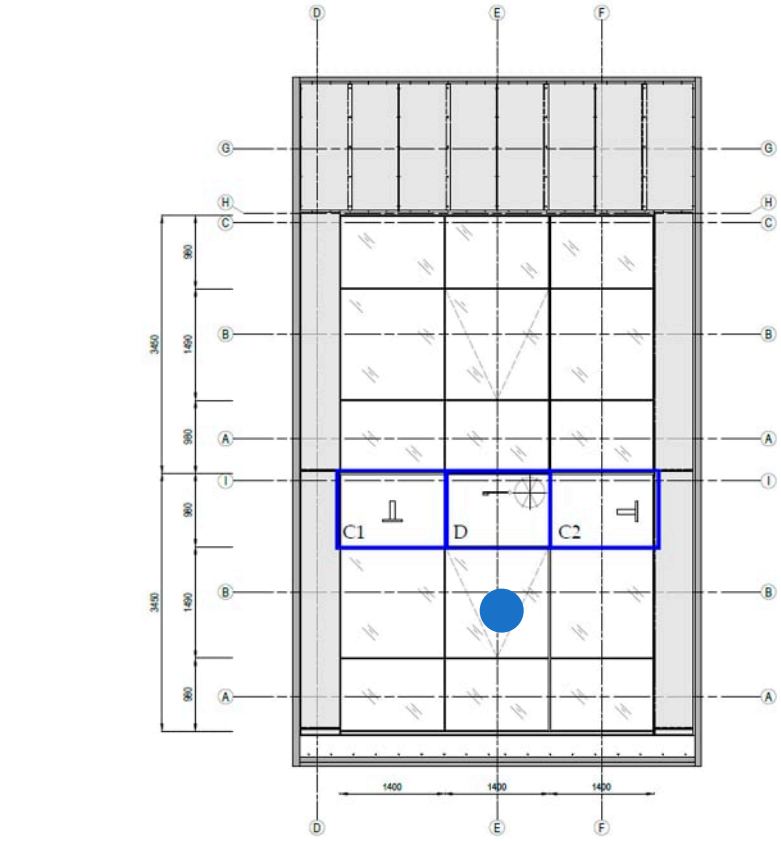


(**a**)

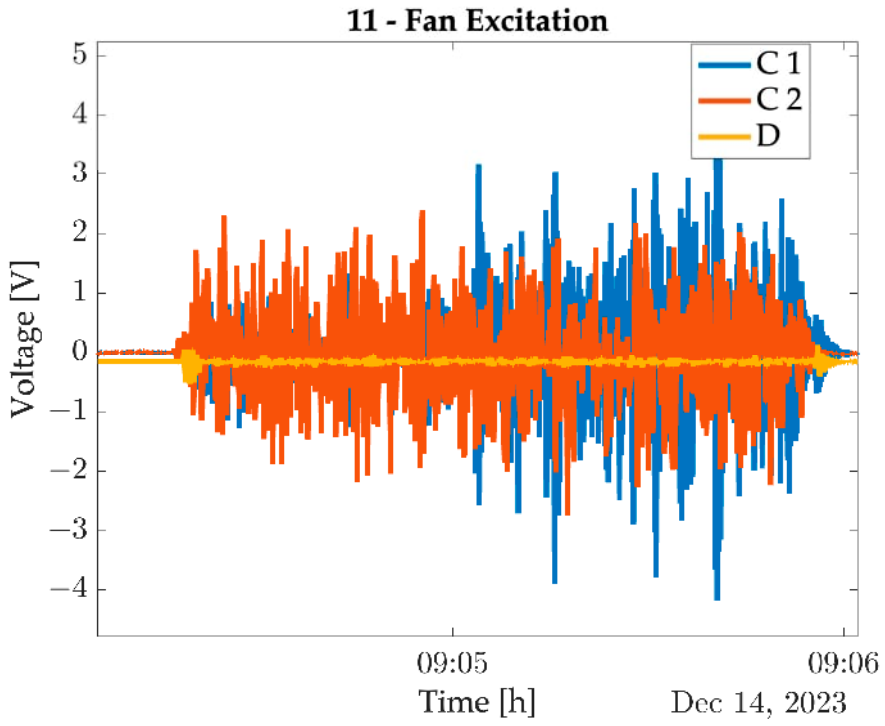


(**b**)

**Figure 14.** Preliminary voltage validation of the PE-EHS wheel configuration installed in the façade in a laboratory testing facility: fan placed at 490 mm from the cavity inlet with an air velocity from 5 to 8 m/s (**a**); PE-EHS voltage generated (**b**); PE-EHS power generated (**c**).

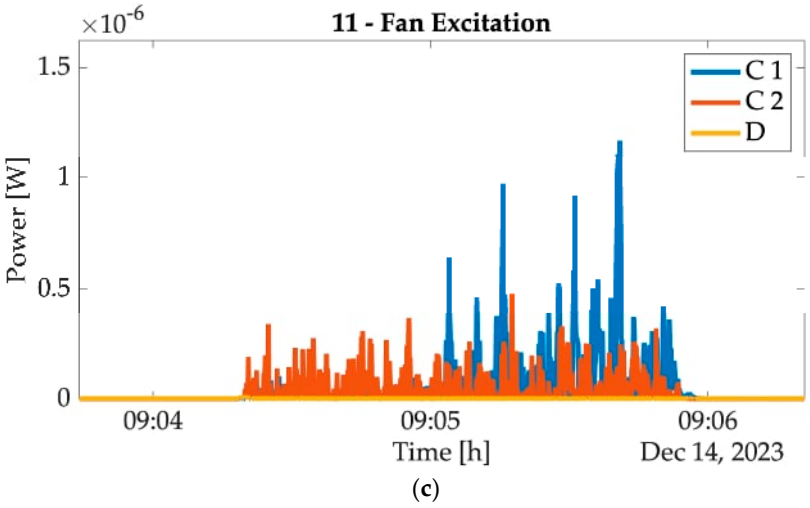


(**c**)

**Figure 14.** *Cont.*

Before testing activities, the laboratory environment was also used to test the overall InComEss system architecture functionality (Figure 15).

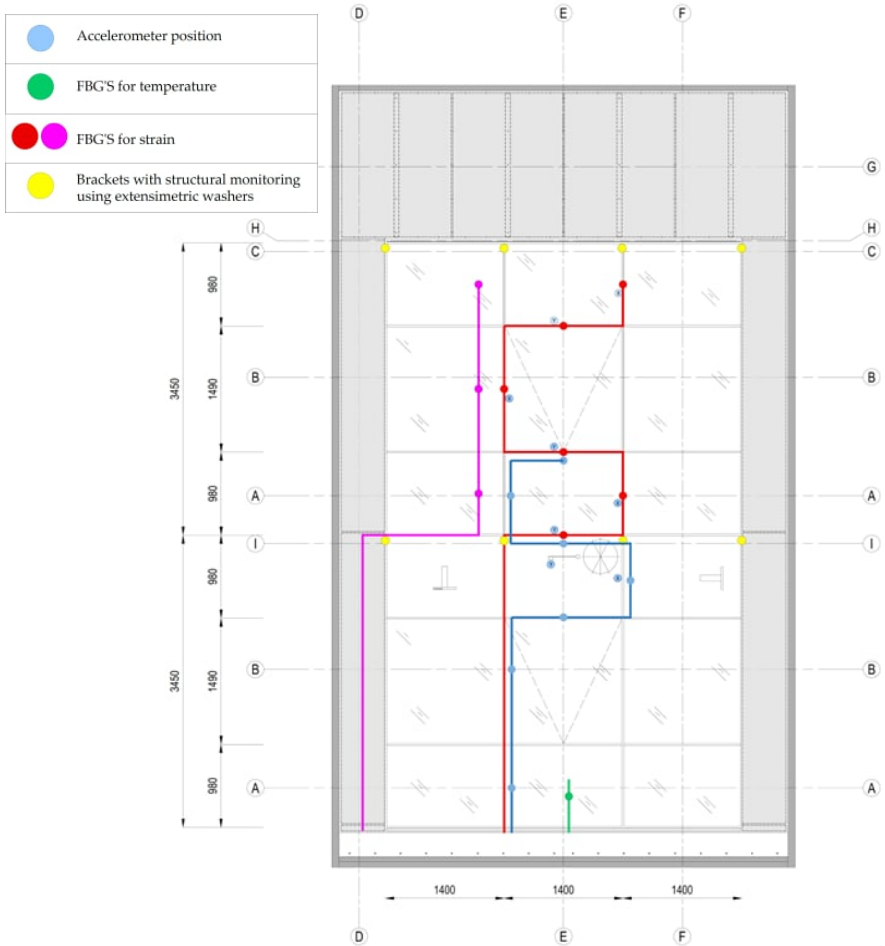


**Figure 15.** The prototype integrating the InComEss architecture system's components into the façade.


**Figure 16.** IoT gateway and IoT platform: IoT gateway with LED screens device reading and data communication to the IoT platform.

The InComEss's IoT gateway acts as a bridge between the sensor field (edge) and the application user's interface (cloud), connecting wireless sensor networks (WSNs) and the IoT platform. Its primary role is to aggregate sensor data from various WSNs. It also functions as short-term storage for collected data to ensure lossless transmission while offering data processing and transformation/harmonization capabilities. The gateway transmits data using both wired and wireless protocols like Ethernet, Wi-Fi, and LTE. Among its competitors, the Raspberry Pi 4 Model B was chosen as the physical IoT gateway due to its numerous advantages. It has built-in Wi-Fi and Ethernet for transmitting data to the cloud or backend servers, Bluetooth communication for connecting with WSNs and gathering measurements, and the ability to readily extend to other protocols like LTE and LoRaWAN. Additionally, a powerful operating system can be installed, offering flexibility for software usage and development. The IoT gateway software primarily consists of Python (version 3.10.11) scripts utilizing various libraries and EdgeXFoundry (version 3.1), simplifying and accelerating deployment. A Python script based on the Bleak library (version 0.21.1) was developed to discover WSN devices and retrieve advertised sensor data. The measurement data were then harmonized and sent to EdgeXFoundry in JSON format using appropriate REST API endpoints. Data were temporarily stored in EdgeXFoundry's REDIS database and then exported to the desired MQTT topic. To enable LTE communication, an extra 4G component (Waveshare 4G HAT) was added. This component features a SIM card port and sits atop the Raspberry Pi 4 Model B. Upon configuration, the Waveshare 4G HAT allows the IoT gateway to communicate with the cloud using wireless LTE. A 50,000 mAh power bank serves as the power supply for the IoT gateway, which is housed in an IP66 protective enclosure for dust and water resistance.

The IoT platform is the data's final destination. Its primary function is to present measurement data in a user-friendly and meaningful way using graphs and charts. It functions as a robust web user interface (UI) leveraging well-known and widely used software libraries for data visualization and representation. The platform is implemented using popular languages like HTML, PHP (version 8.1.6), and Javascript. HighCharts Javascript library (version 11.4.1) is used for data visualization, while the Datatables JQuery plug-in (version 2.0.3) is used for data exploration. Measurement data arrive at the IoT platform through the MQTT message broker. A client within the IoT platform acts as a subscriber to the WSNData topic. The MQTT client collects messages, parses them, and then

permanently stores them in a remote relational or time-series database on the IoT platform side. This database makes the measurement data readily available for both visualization and control purposes. Users can send feedback to the sensor field through the IoT platform to execute control actions or activate actuators to prevent undesirable situations.

During tests (see Appendix A), the PE-EHS energy production was collected for the configurations integrated into the façade. The results achieved during the tests conducted are reported in Figures 17–20. For the understanding of the results, a variable curve for wind pressure against the façade with values from 50 Pa to 600 Pa and intervals of 50 Pa must be considered. These air pressures refer to an air velocity from 9.03 m/s to 31.30 m/s on the façade.

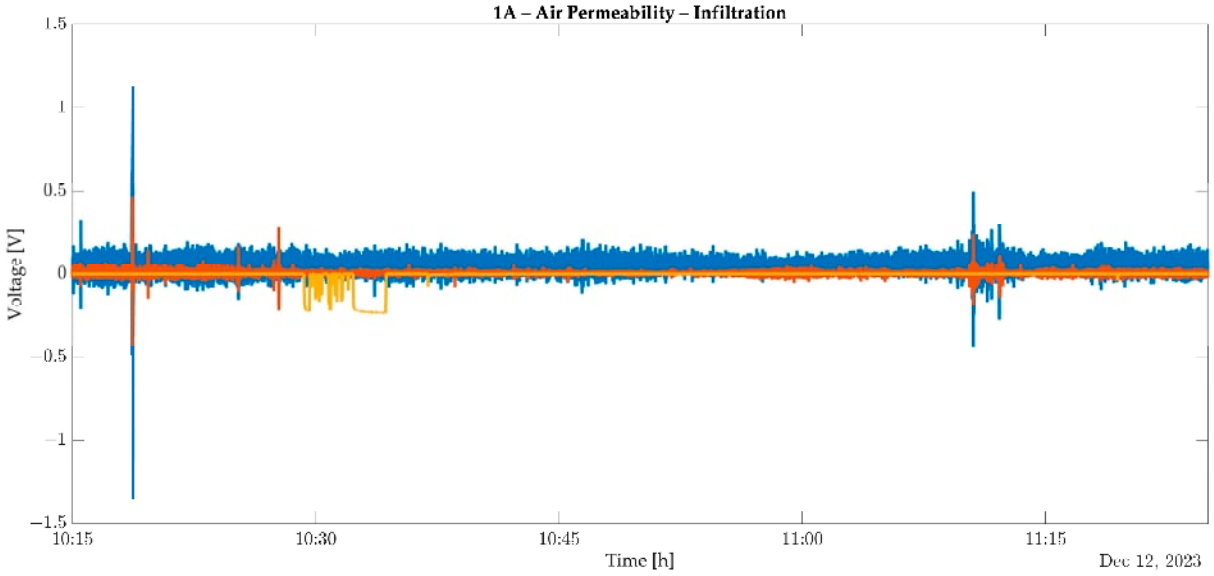


(**a**)

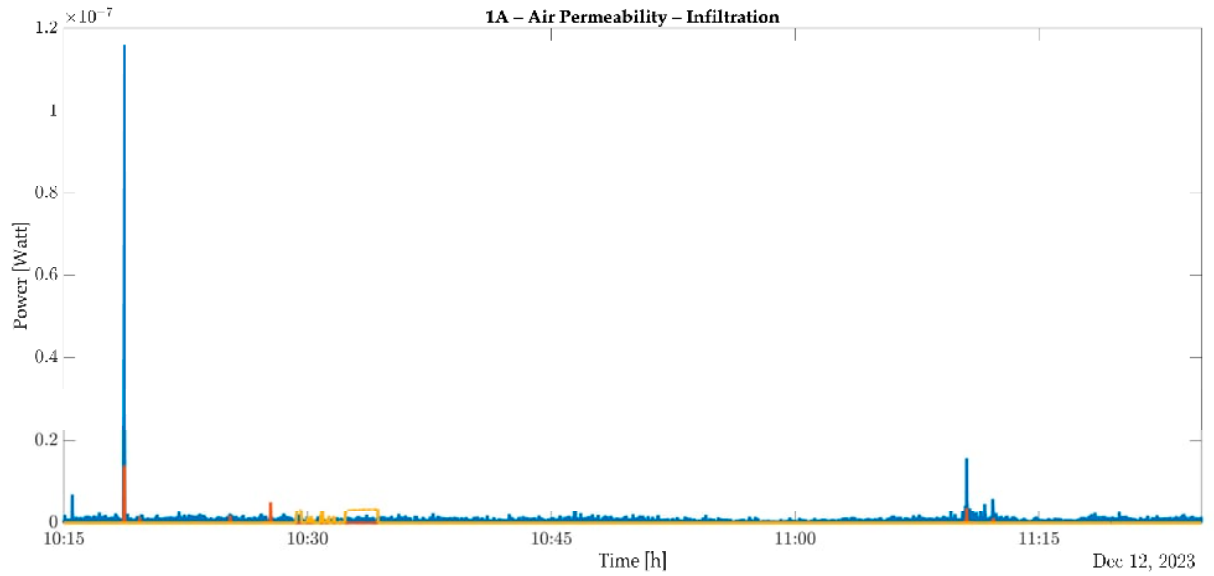


(**b**)

**Figure 17.** PE-EHS results during test "1A—Air Permeability—infiltration": PE-EHS voltage generated (**a**); PE-EHS power generated (**b**).

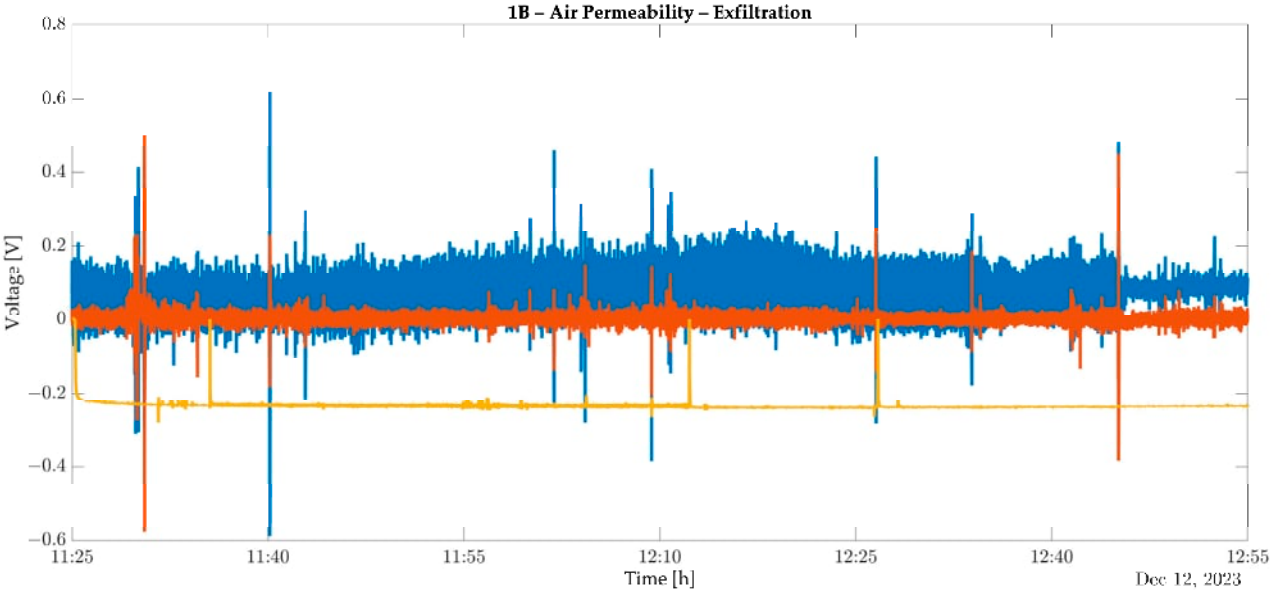


(**a**)

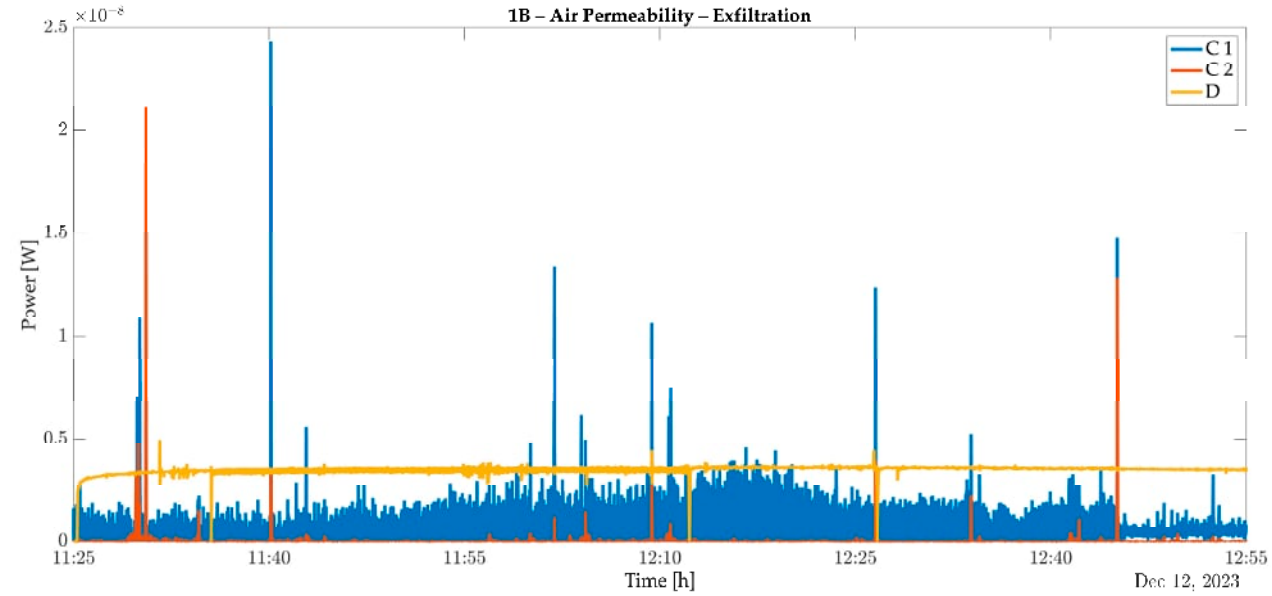


(**b**)

**Figure 18.** PE-EHS results during test "1B—Air Permeability—exfiltration": PE-EHS voltage generated (**a**); PE-EHS power generated (**b**).

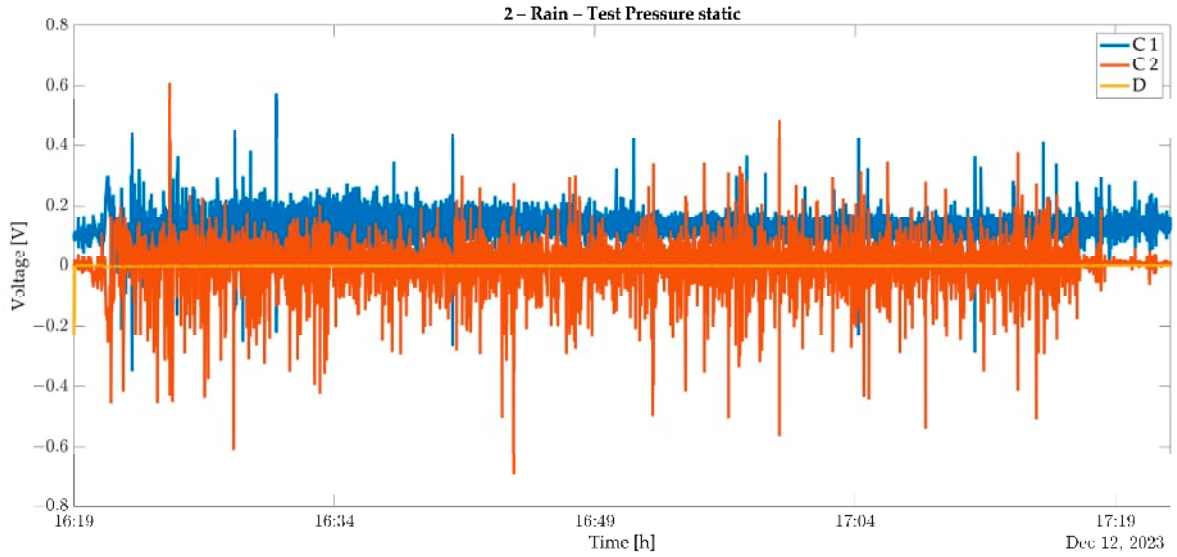


(**a**)

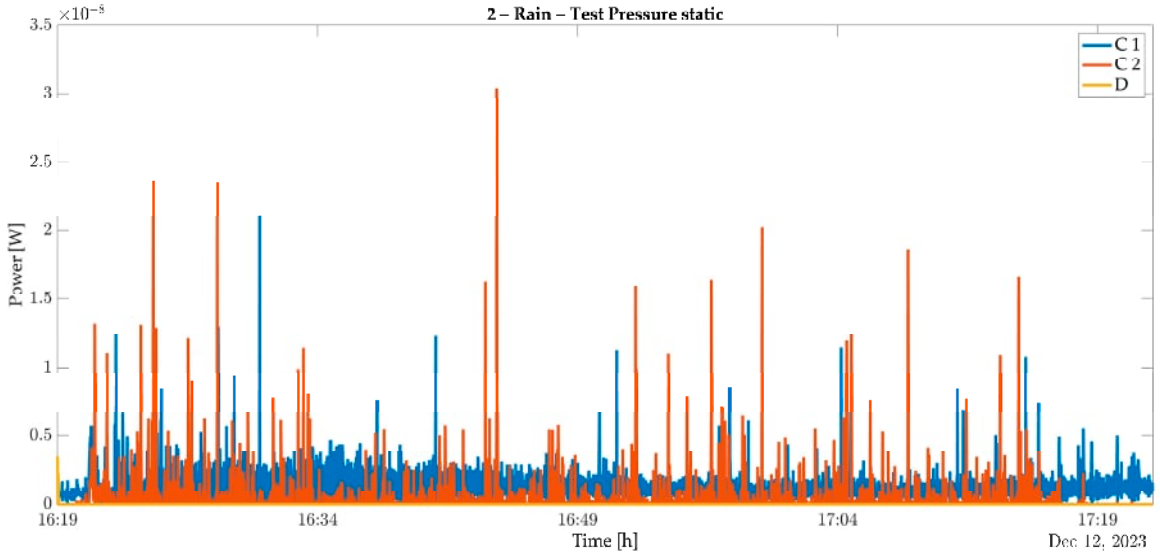


(**b**)

**Figure 19.** PE-EHS results during test "2—Rain—Static": PE-EHS voltage generated (**a**); PE-EHS power generated (**b**).

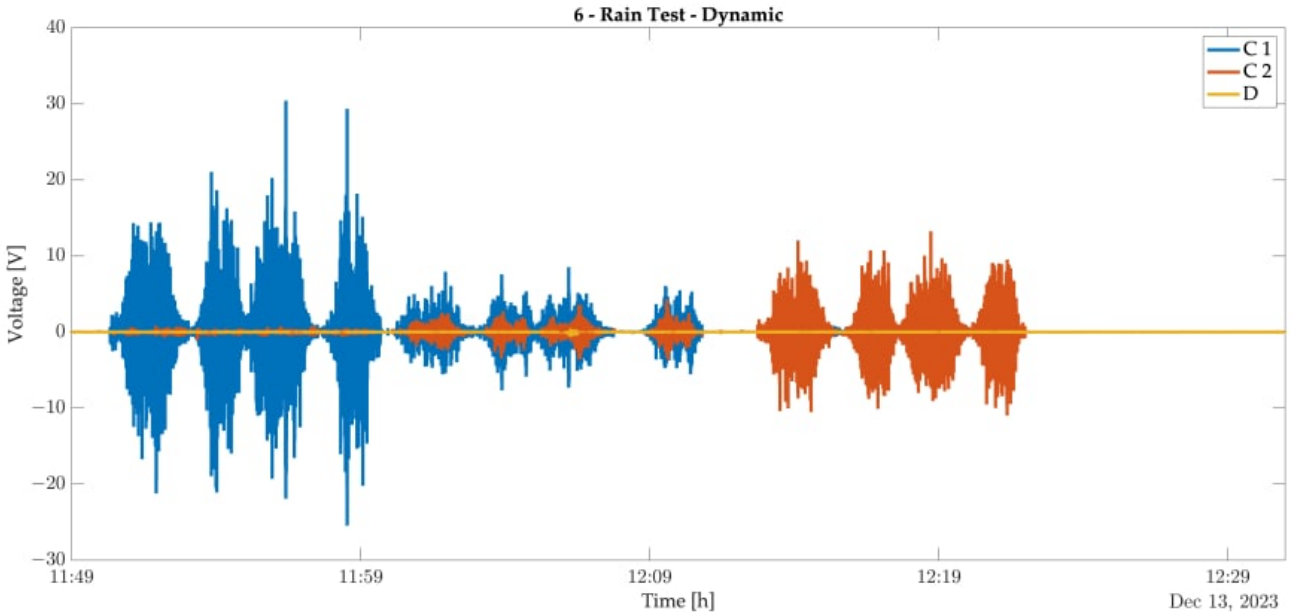


(**a**)

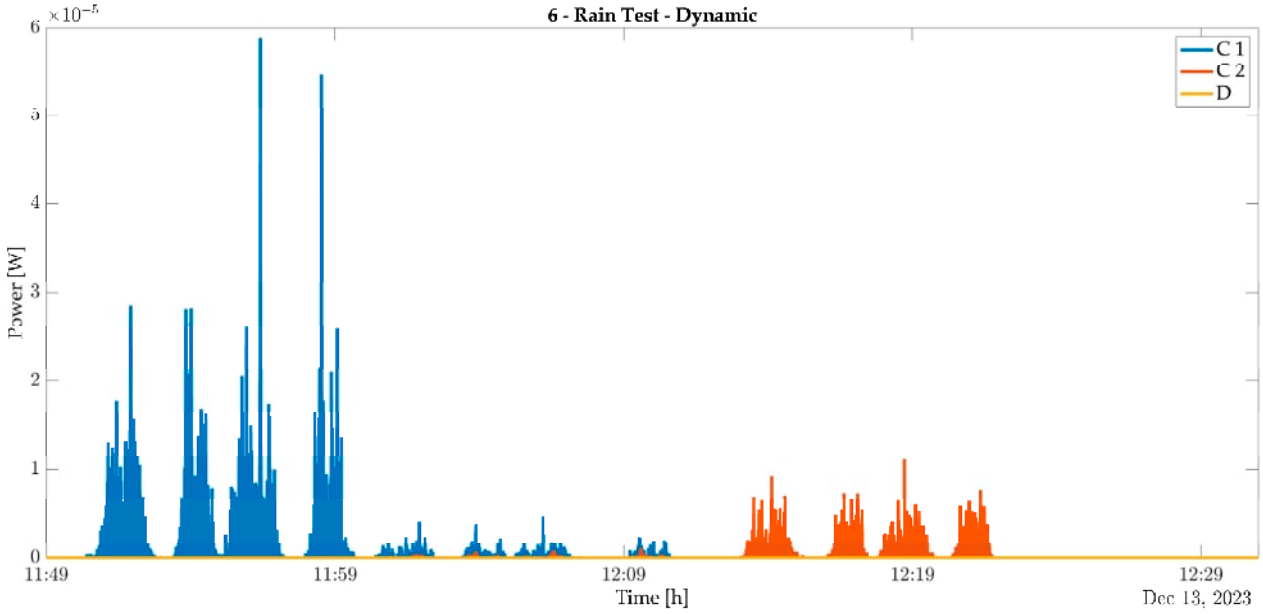


(**b**)

**Figure 20.** PE-EHS results during test "6—Rain—Dynamic": PE-EHS voltage generated (**a**); PE-EHS power generated (**b**).

In all the tests, configurations "C1" and "C2" were demonstrated to be more efficient than configuration "D". However, voltage generation in tests with only air load against the façade achieved an average value of 0.5 V, too low to run an FOS monadgator. On the other side, interesting results were achieved when the façade was stimulated with a dynamic load of wind and rain: the results achieved an average voltage close to 6–8 V. The EP-EHS results will be specifically discussed in the next chapter. The results achieved demonstrate that during the testing activities, the InComEss system performed properly for what concerns the data collection and transmission from the FBG and FOS monadgator, PCC/PCB, and IoT gateway to the IoT platform within.

To facilitate understanding of the different PE-EHS configurations, the configurations are outlined in Table 3. For the lab test, the configurations reported the highest voltage generation during test "6—Rain—Dynamic".

**Table 3.** PE-EHS configurations comparison. PE-harvested power is calculated considering the InComEss's PCC and a time period. Legend: DAF = direct airflow within the ventilated cavity; IAF = indirect airflow within the ventilated cavity; RE = rain excitation of cladding; AFS = airflow speed.

| # | Description | Working Principle | | | Testing Facility | AFS [m/s] | PE Voltage [V] |
|---|---|---|---|---|---|---|---|
| | | DAF | IAF | RE | | | |
| A1 | PE-EHS cantilever with cylinder to enable vortex effect without cladding | X | | | Focchi premises | 0.5–3 | Max. 0.55<br>Min. 0.54 |
| A2 | PE-EHS cantilever with cylinder to enable vortex effect with cladding | X | | | Focchi premises | 0.5–3 | Max. 0.54<br>Min. 0.34 |
| C1 | PE-EHS vertical cantilever with cylinder to enable vortex effect and position in external cladding to exploit cladding vibration | X | | X | Lab chamber fan excitation 490 mm | 5–8 | Max. 4.18<br>Min. 4.30 |
| | | | | | Lab chamber fan excitation 1490 mm | 5–8 | Max. 4.74<br>Min. 3.96 |
| | | | | | Lab chamber (Rain—dynamic) | 9.03–31.30 | Max. 30.45<br>Min. 25.46 |
| C2 | PE-EHS horizontal cantilever with cylinder to enable vortex effect and position in external cladding to exploit cladding vibration | X | | X | Focchi premises | 0.5–3 | Max. 0.64<br>Min. 0.61 |
| | | | | | Lab chamber fan excitation 490 mm | 5–8 | Max. 2.75<br>Min. 2.40 |
| | | | | | Lab chamber fan excitation 1490 mm | 5–8 | Max. 4.27<br>Min. 3.78 |
| | | | | | Lab chamber (Rain—dynamic) | 9.03–31.30 | Max. 13.25<br>Min. 11.00 |
| D | PE-EHS cantilever with magnet activated by magnet installed in a wheel rotating | | X | | CENTI premise | 2–5 | Max. 20<br>Min. 4 |
| | | | | | Lab chamber fan excitation 490 mm | 5–8 | Max. 0.54<br>Min. 0.13 |
| | | | | | Lab chamber fan excitation 1490 mm | 5–8 | Max. 0.71<br>Min. 0.27 |
| | | | | | Lab chamber (Rain—dynamic) | 9.03–31.30 | Max. 0.65<br>Min. 0.45 |

## 4. Discussion

The test results for InComEss architecture and PE-EHSs provide insights, even if not completely satisfying. The results demonstrate the following:

- PE-EHS integration into a façade:
  - The feasibility of integrating PE-EHS within a building envelope's ventilated cavity is confirmed by configurations "C1", "C2", and "D", as the lab integration into a full-scale façade demonstrates. This opens doors for real-world implementations;
  - Balancing architectural requirements with energy harvesting efficiency remains a challenge. While exposed configurations may offer higher energy output, as demonstrated in the preliminary test in the case of perpendicular airflow against the wheel's blades, they often fall short of aesthetic acceptability. Finding an optimal balance is crucial.
- PE-EHS energy generation:
  - In the lab test, configurations "C1" and "C2" demonstrate the potential to combine the vortex effect with cladding vibration for enhanced energy harvesting, especially during wind–rain events. The voltage generated would have been capable of activating the PCC (5 V) and starting to charge the supercapacitor. Additionally, these configurations are promising because their combination, parallel with 2/3 PE-EHS, could increase the power generation and consequently activate within wind conditions comparable to the fan test;

- Configuration "D" showed unexpected performance variations compared to preliminary tests. The discrepancies observed between the wind tunnel and laboratory testing environments can be attributed largely to the wind direction during testing. Performance appears sensitive to wind direction and airflow stability, confirming preliminary tests' boundary conditions even under higher wind loads. In the controlled setting of the wind tunnel, the wind direction aligned perfectly with the rotational direction of the wheel, maximizing its efficiency. However, in the laboratory environment, the fan simulates real-world wind conditions where the wind typically blows perpendicular to the façade. This necessitates the airflow entering the ventilated cavity from the bottom, leading to a reduction in air velocity compared to the wind tunnel scenario. This difference in air velocity directly impacts the performance of the proposed PE-EHS system activated by wheel rotation. In laboratory tests with non-parallel and turbulent airflow, the wheel struggled to initiate rotation at wind velocities between 5 and 8 m/s. This highlights the need for a more stable wind regime, even at lower speeds. This is also the reason why configuration "D" did not achieve the expected 5 V planned for the PCC. Lower air velocity translates to reduced rotational force on the wheel, consequently decreasing the efficiency of energy harvesting. Addressing this challenge is crucial for ensuring the system's effectiveness in real-world applications, with further activities needed to optimize wheel design to improve further responsiveness and performance at lower air velocities and to investigate alternative airflow channeling strategies within the ventilated cavity to enhance air velocity and maintain efficient wheel rotation despite the perpendicular wind direction recommended to identify blind spots and improve performance in variable wind conditions.

- InComEss system architecture:
  - The data collection and transmission functionality of the InComEss architecture for building envelope monitoring was successfully demonstrated using a battery-replacing energy harvesting solution based on the PE-EHS;
  - The low energy generated by the PE-EHS did not allow for validation of the self-powered system to supply the FOS monadgator and enable continuous data collection. Additional PE-EHS units are required to achieve self-powered functionality. The PE-EHS can produce sufficient voltage in an open circuit, but this voltage drops significantly once connected to the PCC due to its low internal resistance. This was observed in lab testing for C1, where the peak voltage dropped from 14 V to 1.4 V upon connection to the PCB, falling short of the minimum required voltage to charge the supercapacitor and power the FOS. The wheel configuration never reached this voltage during testing. The maximum power generated was 4 mA $\times$ 1.4 V = 5.6 mW, which needed 20 mW, not enough to start the charging of the supercapacitor and consequently run the FOS monadgator. Power management was part of the InComEss project, but the selection of alternative on-market power management with lower power consumption could support lower starting voltages and, consequently, the adoption of PE-EHSs.

- Testing procedure:
  - While the testing procedure appears adequate for SHM sensing (not the focus of this paper), it requires further refinement, small environments, further tests, and parameter optimization for PE-EHS evaluation. Addressing the identified challenges and establishing robust testing protocols is crucial for future iterations.

## 5. Conclusions

This study successfully demonstrates the potential of PE-EHS integration within building envelopes for low-wind energy harvesting and SHM applications. However, addressing the identified challenges through further research and design improvements is essential for achieving widespread adoption. While confirming the valuable investigation of stand-alone solutions to enable smart components for building envelopes using PE-EHSs as energy harvesting technology, more specific investigations must include wind directions and instability of the airflow. More specific analysis should be included before tests in a real-scale façade to identify boundary conditions for PE-EHS applications within nonstable wind direction, confirming the issue of blind spot affecting its rotation that emerged during the preliminary testing phase. This activity should be mainly conducted with more comprehensive simulations and wind tunnel testing to evaluate performance under various wind conditions and directions. It is also useful to investigate alternative configurations to improve low wind speed performance and, in particular, work on solutions to reduce wind pressure loss and consequently exploit air velocity more efficiently. Further research and development efforts focused on these areas hold promise for bridging the gap between controlled and real-world testing conditions, ultimately leading to a more robust and adaptable PE-EHS system for ventilated façades. Additionally, a cost analysis should be conducted to understand the economic sustainability of the introduction of multiple PE-EHSs instead of a replaceable battery or a connection with the building's electrical grid system.

Despite the PE-EHS research activities should be further investigated, this research demonstrates how relevant it can be to enable self-powered structural monitoring system. While traditional renewable energy sources like solar panels or wind generators may offer a higher energy generation capacity for building nanogrids, PE-EHSs provide a valuable alternative for powering individual smart components that do not necessitate or cannot be readily connected to the nanogrid. This self-powered approach offers increased flexibility and can be particularly advantageous in scenarios with limited space or challenging installation conditions for traditional solutions. Further research and development efforts focused on optimizing PE-EHS efficiency and integrating it with diverse building elements hold significant promise for fostering a more sustainable and interconnected smart building ecosystem to address challenges that emerged for maximizing the energy harvesting potential of piezoelectric cantilevers within ventilated façades, paving the way for powering a range of smart building components in a sustainable and self-sufficient manner.

The investigated concept of PE cantilevers with magnets activated by a rotating wheel equipped with magnets holds significant promise for optimizing PE-EHS applications within ventilated façades, potentially leading to a more reliable and efficient method of powering smart building components. Further research and development are needed to refine the design and evaluate its performance under real-world conditions. However, this paradigm shift has the potential to unlock new possibilities for harnessing renewable energy within the built environment.

While the ventilated cavity offers a favorable environment for integrating PE-EHSs within building façades, it also presents a challenge. The pressure drop experienced as airflow transitions from the external environment to the cavity is beyond our direct control. However, this challenge can potentially be addressed through specific design strategies for the ventilated cavity. The channel solution designed within the cavity to manipulate airflow and optimize energy harvesting potential has this purpose, but it asks for further implementation. However, it is important to remember that a key benefit of ventilated façades lies in their ability to leverage temperature differences to induce natural ventilation. Therefore, further investigations are warranted to explore and potentially integrate this aspect into the design, potentially mitigating the impact of low wind pressure conditions using temperature differences to have naturally ventilated air. This thermal-based ventilation analysis should specifically guide the design of the wheel.

The InComEss architecture validated during the test demonstrates that a data-driven approach can enable a comprehensive understanding of how the building envelope structure behaves under mechanical and thermal stresses due to wind load, seismic actions, material stress, temperature fluctuations, and other dynamic loads. The data analysis could allow to make informed choices within the SHM field regarding maintenance schedules, retrofitting requirements and overall design improvements, foreseeing unexpected failures, and minimizing the environmental impact associated with structural repairs. However, a critical point that necessitates further investigation is the PE configuration, optimizing the design and performance of the PE to ensure it generates sufficient current even under the current limitations of the PCC. Similarly, it is necessary to investigate alternative approaches to enhance the overall system's energy output and identify solutions to achieve the desired power levels effectively. This could involve exploring different PCC designs or implementing alternative methods for power management.

In conclusion, this research proposes a promising paradigm shift in PE-EHS technology for ventilated façades, offering a potentially more reliable and efficient approach to powering smart building components. While challenges exist, the proposed solutions and future research directions outlined hold significant promise for realizing the full potential of this innovative technology in the context of sustainable building design.

**Author Contributions:** Conceptualization, A.P., L.V., D.S.E. and A.R.A.M.; methodology, A.P.; IoT design (gateway, platform), hardware and software development, M.V. and A.A.; validation, A.P., L.V., F.B., D.S.E. and A.R.A.M.; formal analysis, A.P. and L.V.; investigation, A.P., L.V., D.S.E. and A.R.A.M.; resources, A.P., L.V., F.B., D.S.E. and A.R.A.M.; data curation, A.P. and L.V.; writing—original draft preparation, A.P.; writing—review and editing, A.P., L.V., F.B., D.S.E., A.R.A.M., M.V., M.T.C. and A.A.; visualization, A.P., L.V., F.B., D.S.E., M.T.C. and A.R.A.M.; supervision, A.P.; project administration, A.P.; funding acquisition, A.P. All authors have read and agreed to the published version of the manuscript.

**Funding:** This research was funded by the European Project "InComEss" under the European Union's Horizon 2020 Research and Innovation Programme, grant number 862597.

**Data Availability Statement:** No data are available due to privacy restrictions.

**Acknowledgments:** The authors thank the Mechanical and Thermal Measurements Group from Università Politecnica delle Marche for their active support and involvement during laboratory testing activities.

**Conflicts of Interest:** Author Maria Teresa Calcagni, affiliated with Università Politecnica delle Marche, was engaged with a service contract by the company Focchi S.p.A. The remaining authors declare that the research was conducted in the absence of any commercial or financial relationships that could be construed as a potential conflict of interest.

## Appendix A

**Table A1.** Laboratory environment's test method statement. n.a.—not available.

| Sequence | Test | Activity—Range Values | Test Time |
|---|---|---|---|
| 1A | Air—infiltration | Test pressure: + 600 Pa (Class A4) | 45′ |
| 1B | Air—exfiltration | Test pressure: −600 Pa (Class A4) | 1 h 15′ |
| 2 | Rain—test static | Test pressure: 600 Pa (Class R7) | 55′ |
| 3A | Wind—pression | Test pressure: +1750 Pa | 8′ |
| 3B | Wind—depression | Test pressure: −2000 Pa | 8′ |
| 4A | Air—infiltration | Test pressure: + 600 Pa (Class A4) | 8′ |
| 4B | Air—exfiltration | Test pressure: −600 Pa (Class A4) | 8′ |

**Table A1.** *Cont.*

| Sequence | Test | Activity—Range Values | Test Time |
|---|---|---|---|
| 5 | Rain—test static | Test pressure: 600 Pa (Class R7) | 1 h 5′ |
| 6 | Rain—test dynamic | Dynamic water penetration test with fan with a pulse every 3 s from 750 Pa to 250 Pa | 36′ |
| 7A | Building movement—vertical | 1. Vertical offset of the intermediate unit: uz = ±7 [mm]—2 cycles | n.a. |
| 7B | Building movement—horizontal | 2. Horizontal offset of the intermediate beam: uz = ±7 [mm]—2 cycles | n.a. |
| 8A | Air—infiltration | Test pressure: +600 Pa (Class A4) | 7′30″ |
| 8B | Air—exfiltration | Test pressure: −600 Pa (Class A4) | 7′30″ |
| 9 | Rain—test static | Test pressure: 600 Pa (Class R7) | 1 h |
| 10A | Wind—pression | Test pressure: 2625 Pa | 2′ |
| 10B | Wind—depression | Test pressure: −3000 Pa | 2′ |
| 11 | Fan excitation | Dynamic test | 1 h 35′ |
| 12A | Impact test—hard body | 6 J (1.224 mm height with 0.5 kg steel ball)10 J (1.020 mm height with 1.0 kg steel ball) | n.a. |
| 12B | Impact test—soft body | 120 J (245 mm height)500 J (1020 mm height) | n.a. |
| 12C | Impact test—double type | 343 J (700 mm height) | n.a. |

## References


1. Blum, D.; Candanedo, J.; Chen, Z.; Fierro, G.; Gori, V.; Johra, H.; Madsen, H.; Marszal-Pomianowska, A.; O'Neill, Z.; Pradhan, O.; et al. *Data-Driven Smart Buildings: State-of-the-Art Review*; CSIRO: Newcastle, Australia, 2023; 103p.
2. Karimi, R.; Farahzadi, L.; Sepasgozar, S.M.E.; Sargolzaei, S.; Sepasgozar, S.M.E.; Zareian, M.; Nasrolahi, A.; Karimi, R.; Farahzadi, L.; Sepasgozar, S.M.E.; et al. Smart Built Environment Including Smart Home, Smart Building and Smart City: Definitions and Applied Technologies. In *Advances and Technologies in Building Construction and Structural Analysis*; IntechOpen: London, UK, 2021; ISBN 978-1-83881-141-9.
3. Politecnico di Milano; Energy & Strategy Group. *Smart Building Report 2022*; Efficienza Energetica e Trasformazione Digitale nel Settore degli Edifici; Dipartimento di Ingegneria Gestionale Collana Quaderni AIP: Milan, Italy, 2022.
4. Verbeke, S.; Aerts, D.; Reynders, G.; Ma, Y.; Waide, P. *Final Report on the Technical Support to the Development of a Smart Readiness Indicator for Buildings: Summary*; Publications Office of the European Union: Luxembourg, 2020; ISBN 978-92-76-19978-6.
5. Zaffagnini, T.; Pracucci, A. Dalla Città Intelligente Alla Responsive City. Applicativi IoT e Tecnologie Innovative Human-Centric Based per Edifici Intelligenti Di Nuova Generazione. *L'Ufficio Tec.* **2023**, *1–2*, 17.
6. Intelligent Buildings—An Overview | ScienceDirect Topics. Available online: https://www.sciencedirect.com/topics/engineering/intelligent-buildings (accessed on 29 January 2024).
7. Smart Readiness Indicator. Available online: https://energy.ec.europa.eu/topics/energy-efficiency/energy-efficient-buildings/smart-readiness-indicator_en (accessed on 29 January 2024).
8. Energy Performance of Buildings Directive. Available online: https://energy.ec.europa.eu/topics/energy-efficiency/energy-efficient-buildings/energy-performance-buildings-directive_en (accessed on 29 January 2024).
9. European Parliament. *Directive (EU) 2018/of the European Parliament and of the Council of 30 May 2018 Amending Directive 2010/31/EU on the Energy Performance of Buildings and Directive 2012/27/EU on Energy Efficiency*; European Parliament: Strasbourg, France, 2018.
10. Actions to Digitalise the Energy Sector. Available online: https://ec.europa.eu/commission/presscorner/detail/en/ip_22_6228 (accessed on 29 January 2024).
11. Overview Article-Smart Buildings and Smart Technologies in Europe: State of Play and Perspectives | BUILD UP. Available online: https://build-up.ec.europa.eu/en/resources-and-tools/articles/overview-article-smart-buildings-and-smart-technologies-europe-state (accessed on 29 January 2024).
12. The EU Smart Building Innovation Platform | SMARTBUILT4EU Project | Fact Sheet | H2020. Available online: https://cordis.europa.eu/project/id/956936 (accessed on 29 January 2024).
13. Intelligent Building Energy Assets Control for Comfort, Energy and Flexibility Optimisation | iBECOME Project | Fact Sheet | H2020. Available online: https://cordis.europa.eu/project/id/894617/it (accessed on 29 January 2024).
14. Zeng, Z.; Zhao, R.; Yang, H. Micro-Sources Design of an Intelligent Building Integrated with Micro-Grid. *Energy Build.* **2013**, *57*, 261–267. [CrossRef]

15. Shinisha, A.; Devi, S.; Murugasan, D.; Solomon Simon, E. Future Nano-Grid Technologies and Its Implementation Challenges for Smart Cities. *IOP Conf. Ser. Mater. Sci. Eng.* **2020**, *955*, 012002. [CrossRef]
16. Saeed, M.; Fangzong, W.; Kalwar, B.; Iqbal, S. A Review on Microgrids' Challenges & Perspectives. *IEEE Access* **2021**, *9*, 166502–166517. [CrossRef]
17. Shakeri, M.; Pasupuleti, J.; Amin, N.; Rokonuzzaman, M.; Low, F.W.; Yaw, C.T.; Asim, N.; Samsudin, N.A.; Tiong, S.K.; Hen, C.K.; et al. An Overview of the Building Energy Management System Considering the Demand Response Programs, Smart Strategies and Smart Grid. *Energies* **2020**, *13*, 3299. [CrossRef]
18. Khan, S.; Sudhakar, K.; Hazwan Yusof, M.; Sundaram, S. Review of Building Integrated Photovoltaics System for Electric Vehicle Charging. *Chem. Rec.* **2024**, *24*, e202300308. [CrossRef] [PubMed]
19. Fiorotti, R.; Yahyaoui, I.; Rocha, H.R.O.; Honorato, Í.; Silva, J.; Tadeo, F. Demand Planning of a Nearly Zero Energy Building in a PV/Grid-Connected System. *Renew. Energy Focus* **2023**, *45*, 220–233. [CrossRef]
20. Wei, W.; Ye, L.; Fang, Y.; Wang, Y.; Chen, X.; Li, Z. Optimal Allocation of Energy Storage Capacity in Microgrids Considering the Uncertainty of Renewable Energy Generation. *Sustainability* **2023**, *15*, 9544. [CrossRef]
21. Saavedra, E.; Mascaraque, L.; Calderon, G.; del Campo, G.; Santamaria, A. The Smart Meter Challenge: Feasibility of Autonomous Indoor IoT Devices Depending on Its Energy Harvesting Source and IoT Wireless Technology. *Sensors* **2021**, *21*, 7433. [CrossRef]
22. Sonbul, O.S.; Rashid, M. Towards the Structural Health Monitoring of Bridges Using Wireless Sensor Networks: A Systematic Study. *Sensors* **2023**, *23*, 8468. [CrossRef] [PubMed]
23. Shokoor, F.; Shafik, W. Harvesting Energy Overview for Sustainable Wireless Sensor Networks. *J. Smart Cities Soc.* **2023**, *2*, 165–180. [CrossRef]
24. Arnesano, M.; Bueno, B.; Pracucci, A.; Magnagni, S.; Casadei, O.; Revel, G.M. Sensors and Control Solutions for Smart-IoT Façade Modules. In Proceedings of the 2019 IEEE International Symposium on Measurements & Networking (M&N), Catania, Italy, 8–10 July 2019; pp. 1–6.
25. Giovanardi, M.; Baietta, A.; Belletti, F.; Magnani, S.; Casadei, O.; Pracucci, A. Exploiting the Value of Active and Multifunctional Façade Technology through the IoT and AI. *Appl. Sci.* **2024**, *14*, 1145. [CrossRef]
26. Pracucci, A.; Dugué, A.; Richet, N.; Abdullah, T.; Başer, E.; Caneva, S.; Deneyer, A.; Dias, P.; Diygu, C.; Fakhari, M.; et al. IWG5 White Paper. IWG 5 Buildings. 2023. Available online: https://www.iwg5-buildings.eu/wp-content/uploads/2023/09/IWG5_Active-Module_white-paper_v3_Final.pdf (accessed on 27 March 2024).
27. Guardigli, L.; Fornace, F.D.; Casadei, O.; Frani, F.; Nicolini, L.; Revel, G.M.; Arnesano, M. Development of a Curtain Wall Prototype with Dynamic Behaviour (SmartSkin). *TECHNE-J. Technol. Archit. Environ.* **2018**, *16*, 218–225. [CrossRef]
28. Pracucci, A.; Vandi, L.; Magnani, S.; Baietta, A.; Casadei, O.; Uriarte, A.; Vavallo, M. Prefabricated Plug-and-Play Unitized Façade System for Deep Retrofitting: The RenoZEB Case Study. In Proceedings of the The 9th Annual Edition of Sustainable Places (SP 2021), Rome, Italy, 29 September–1 October 2021; p. 9.
29. Infinite Building Renovation-Industrialised Envelope Solutions. Available online: https://infinitebuildingrenovation.eu/ (accessed on 16 June 2023).
30. Thulasi, V.; Lakshmi, P.; Sahithya, A. High Performance of W-Shaped Piezo Electric Energy Harvester for Smart Building Application. *Integr. Ferroelectr.* **2024**, *240*, 149–162. [CrossRef]
31. Zhou, W.; Du, D.; Cui, Q.; Lu, C.; Wang, Y.; He, Q. Recent Research Progress in Piezoelectric Vibration Energy Harvesting Technology. *Energies* **2022**, *15*, 947. [CrossRef]
32. Wang, B.; Zhang, C.; Lai, L.; Dong, X.; Li, Y. Design, Manufacture and Test of Piezoelectric Cantilever-Beam Energy Harvesters with Hollow Structures. *Micromachines* **2021**, *12*, 1090. [CrossRef]
33. Doria, A.; Fanti, G.; Filipi, G.; Moro, F. Development of a Novel Piezoelectric Harvester Excited by Raindrops. *Sensors* **2019**, *19*, 3653. [CrossRef] [PubMed]
34. Doria, A.; Medè, C.; Fanti, G.; Desideri, D.; Maschio, A.; Moro, F. Development of Piezoelectric Harvesters with Integrated Trimming Devices. *Appl. Sci.* **2018**, *8*, 557. [CrossRef]
35. Doria, A.; Medè, C.; Desideri, D.; Maschio, A.; Codecasa, L.; Moro, F. On the Performance of Piezoelectric Harvesters Loaded by Finite Width Impulses. *Mech. Syst. Signal Process.* **2018**, *100*, 28–42. [CrossRef]
36. Students Harness Vibrations from Wind for Electricity. Available online: https://news.cornell.edu/stories/2010/05/researchers-harness-energy-wind-vibrations (accessed on 29 April 2020).
37. Solaripedia | Green Architecture & Building | Projects in Green Architecture & Building. Available online: https://www.solaripedia.com/13/285/3171/solar_ivy_leaves.html (accessed on 29 April 2020).
38. The 10th Annual Year in Ideas-Interactive Feature-NYTimes.Com. Available online: http://archive.nytimes.com/www.nytimes.com/interactive/2010/12/19/magazine/ideas2010.html#Turbine-Free_Wind_Power (accessed on 29 April 2020).
39. Raudaschl, M.; Levak, T.; Riewe, R.; Triantafyllidis, G.; Drnda, E.; Popek, S.; Schlegl, D.; Funke-Kaiser, D.; Lund, A. Piezoelectric Textile Façade for the Energy Supply of Active Sensor Technology with Regard to Data Management for Circular Economy in Building Construction. *IOP Conf. Ser. Earth Environ. Sci.* **2022**, *1078*, 012037. [CrossRef]
40. Structural Health Monitoring—An Overview | ScienceDirect Topics. Available online: https://www.sciencedirect.com/topics/chemical-engineering/structural-health-monitoring (accessed on 29 January 2024).
41. Ferreira, P.M.; Machado, M.A.; Carvalho, M.S.; Vidal, C. Embedded Sensors for Structural Health Monitoring: Methodologies and Applications Review. *Sensors* **2022**, *22*, 8320. [CrossRef] [PubMed]

42. Valinejadshoubi, M.; Bagchi, A.; Moselhi, O. Structural Health Monitoring of Buildings and Infrastructure. *World Acad. Sci. Eng. Technol.-Int. J. Civ. Environ. Eng.* **2016**, *10*, 731–738.
43. Preethichandra, D.M.G.; Suntharavadivel, T.G.; Kalutara, P.; Piyathilaka, L.; Izhar, U. Influence of Smart Sensors on Structural Health Monitoring Systems and Future Asset Management Practices. *Sensors* **2023**, *23*, 8279. [CrossRef] [PubMed]
44. Bremer, K.; Wollweber, M.; Weigand, F.; Rahlves, M.; Kuhne, M.; Helbig, R.; Roth, B. Fibre Optic Sensors for the Structural Health Monitoring of Building Structures. *Procedia Technol.* **2016**, *26*, 524–529. [CrossRef]
45. InComEss. Available online: https://www.incomess-project.com (accessed on 29 January 2024).
46. *EN 13830:2003*; Curtain Walling—Product Standard. SIST: Ljubljana, Slovenia, 2003. Available online: https://standards.iteh.ai/catalog/standards/cen/51c14384-e4c8-49ba-8658-6aac20f9ae1f/en-13830-2003 (accessed on 27 March 2024).
47. Smart Material Company. Available online: https://www.smart-material.com/EH-MFC-generatorsV2.html (accessed on 26 February 2024).
48. MacroFiberCompositeTM P2 Type. Available online: https://www.smart-material.com/MFC-product-P2V2.html (accessed on 26 February 2024).
49. Vlachos, M.; Lopardo, R.; Amditis, A. Real Time Vehicle Status Monitoring under Moving Conditions Using a Low Power IoT System. *J. Internet Things* **2023**, *4*, 235–261. [CrossRef]
50. Schabowicz, K.; Zawiślak, Ł.; Staniów, P. Efficiency of Ventilated Façades in Terms of Airflow in the Air Gap. *Stud. Geotech. Mech.* **2021**, *43*, 224–236. [CrossRef]
51. Rahiminejad, M.; Khovalyg, D. Review on Ventilation Rates in the Ventilated Air-Spaces behind Common Wall Assemblies with External Cladding. *Build. Environ.* **2021**, *190*, 107538. [CrossRef]
52. Tommasino, D.; Moro, F.; de Pablo Corona, E.; Vandi, L.; Baietta, A.; Pracucci, A.; Doria, A. Optimization of a Piezoelectric Wind-Excited Cantilever for Energy Harvesting from Façades. In Proceedings of the Advances in Italian Mechanism Science; Niola, V., Gasparetto, A., Quaglia, G., Carbone, G., Eds.; Springer International Publishing: Cham, Switzerland, 2022; pp. 848–856.
53. Che Tempo Faceva a Poggio Torriana a Novembre 2021-Archivio Meteo Poggio Torriana » ILMETEO.It. Available online: https://www.ilmeteo.it/portale/archivio-meteo/Poggio+Torriana/2021/Novembre (accessed on 26 February 2024).
54. Che Tempo Faceva a Poggio Torriana a Dicembre 2021-Archivio Meteo Poggio Torriana. Available online: https://www.ilmeteo.it/portale/archivio-meteo/Poggio+Torriana/2021/Dicembre (accessed on 26 February 2024).
55. Che Tempo Faceva a Poggio Torriana a Giugno 2023-Archivio Meteo Poggio Torriana. Available online: https://www.ilmeteo.it/portale/archivio-meteo/Poggio+Torriana/2023/Giugno (accessed on 26 February 2024).
56. Ansys 2023 R2 Release Highlights | Ansys Latest Release. Available online: https://www.ansys.com/products/release-highlights (accessed on 1 February 2024).

# Optimization of a piezoelectric wind-excited cantilever for energy harvesting from façades

Domenico Tommasino[1], Federico Moro[1], Enrique de Pablo Corona[2], Laura Vandi[3], Alessia Baietta[3], Alessandro Pracucci[3] and Alberto Doria[1]

[1] University of Padova, Padova, Italy
domenico.tommasino@phd.unipd.it
[2] Smart Material GmbH, Dresden, Germany
[3] Focchi Spa, Poggio Torriana (RN), Italy

**Abstract.** The optimization of the performance of a piezoelectric cantilever for energy harvesting from façades is concerned. The harvester is designed to exploit the vortex-induced vibrations due to the fluid-structure interaction between a cylindrical bluff body and the wind flow acting on the façade. An analytical lumped parameter model of the piezo-cantilever equipped with a cylindrical bluff body is provided to estimate the frequency response function between the aerodynamic tip force and the generated open circuit voltage. The analytical frequency response function is validated using experimental tests performed on a prototype of the piezo-cantilever. Finally, the optimal design variables of the harvester to maximize the generated voltage are determined using an optimization algorithm.

**Keywords:** energy harvesting, piezoelectric harvester, vortex shedding, optimization algorithm, building façade.

## 1 Introduction

Building industry in the last years has shown an increasing interest in smart components and in particular in smart IoT facades [1]. A smart IoT façade module is equipped with sensors that transmit data to the building management system and with actuators that modify the façade properties driving shading elements or openable vents. The final target being the improvement of the comfort of the occupants and the maximization of energetic efficiency [2, 3]. The integration of a large number of sensors and actuators on a façade requires long and complex wirings. Nowadays, an alternative to wirings is offered by energy harvesting systems that exploit the energy fluxes that usually hit a façade: thermal energy, wind energy, vibration energy. The interest in harvesters is increasing, since new environment-friendly harvesters, which do not make use of toxic elements (Pb, Bi, Te, Sb), are under development.

This paper deals with the development of piezoelectric harvesters able to scavenge the wind energy that hits the facade. Wind energy can be converted into electrical energy exploiting different phenomena. In [5, 6] studies were carried out to exploit the vortex shedding phenomenon from a bluff body mounted on cantilever harvester. In [7] turbulence was exploited mimicing the behavior of grass. In [8] the fluttering of an inverted-

flag piezoelectric harvester was analyzed. This paper focuses on the first phenomenon vortex shedding and presents the model of a cantilever harvester with cylindrical bluff body hit by a mild wind (velocity 1.4 m/s), which is typical of buildings in normal conditions. After experimental validation, the mathematical model is used for optimizing the dimensions of the harvester and a large increase in the generated voltage is obtained.

# 2 Mathematical model

## 2.1 Vortex-induced vibrations

A vortex-induced vibration is a typical fluid-structure interaction phenomenon, which affects bluff bodies in a steady fluid flow [9, 10]. For Reynolds numbers larger than 40, the formation of these vortices generates a variation of pressure around the body which results in a periodic lift force when the vortices are alternatively shed [9]. The generated aerodynamic force is orthogonal to the flow direction and can be quantified as a harmonic force on the bluff body as follows:

$$F_{aero}(t) = \frac{1}{2}\rho_a A_c U^2 C_L(t) = \frac{1}{2}\rho_a A_c U^2 C_{L0} \sin(2\pi f_{vs} t) \quad (1)$$

where $C_L$ is the time-dependent lift coefficient, $\rho_a$ the fluid density, $A_c$ the windward cross-section of the bluff body, $U$ the fluid velocity. The parameter $f_{vs}$ is the vortex shedding frequency and is given by the following equation:

$$f_{vs} = \frac{U S_t}{D} \quad (2)$$

in which $D$ is a geometric parameter of the bluff body, $S_t$ the Strouhal number.
The shedding of vortices synchronizes with the free movement of the structure when the $f_{vs}$ is close to the natural frequency $f_n$ of the structure. A large-amplitude self-sustained vibration occurs in this condition, due to the resonance phenomenon. Vortex-induced vibrations can be exploited in energy harvesting applications. It is important underlying that $f_{vs}$ has to match $f_n$ of the harvester to maximize the performance of the generator. It is worth noticing that both frequencies ($f_{vs}, f_n$) depend on the geometry of the harvester, hence its dimensions have to be properly determined to guarantee the correct tuning.

## 2.2 Piezoelectric cantilever harvester with cylindrical tip mass

The harvester consists of a composite cantilever beam, made by a structural substrate covered by a piezoelectric layer, and it is equipped with a cylindrical tip mass, as shown in Figure 1. The vibration of the harvester is analyzed using a single-mode approach and only the fundamental mode is considered, since it is enough to investigate maximum performance [11]. As long as the first mode of vibration is concerned, the displacement $(y)$ and the rotation $(\varphi)$ at the end of the beam (point *P* in Fig. 1) are dependent variables. The relation between $y$ and $\varphi$ is expressed by the following equation [12]:

$$y = \frac{2}{3} L_b \varphi \tag{3}$$

where $L_b$ is the length of the cantilever beam. The composite cantilever is modeled as a mass-less spring and its corresponding moving mass, calculated using Rayleigh's method, is added to the tip mass. In these hypotheses, the harvester is simulated as a one-Degree of Freedom (DoF) mass-spring-damper system equipped with a lumped piezoelectric element, which considers the piezoelectric coupling effect [13]. The aerodynamic force $F_{aero}$ is schematized as a harmonic force acting on the center of mass $G$ of the cylinder. The cylindrical tip mass is represented by a hollow cylinder.

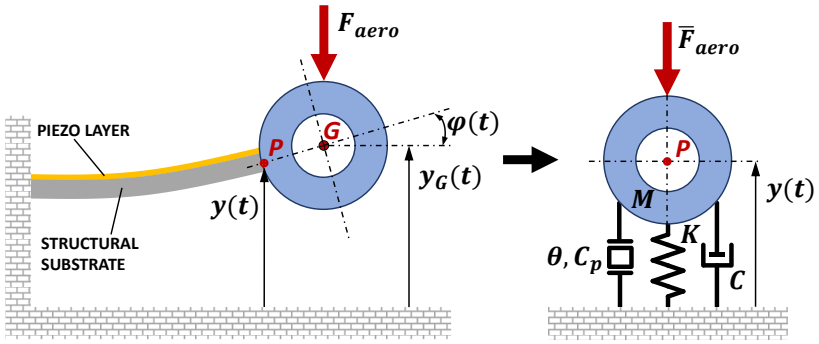


**Fig. 1.** Scheme of the one-DoF lumped parameter model.

The equation of motion is determined using the Lagrangian method, which allows to define the lumped mass ($M$), stiffness ($K$), damping coefficient ($C$) and the Lagrangian component of the force ($\bar{F}_{aero}$) along y-direction:

$$\begin{cases} M = \frac{33}{140}\left(\rho_b L_b w_b t_b + m_p\right) + \rho_c \frac{\pi\left(D_e^2 - D_i^2\right)}{4} L_c \left(1 + \frac{3D_e}{4L_b}\right)^2 + \frac{1}{32}\rho_c \pi (D_e^4 - D_i^4) L_c \left(\frac{3}{2L_b}\right)^2 \\ K = \frac{E w_b t_b^3}{4L_b^3} + \frac{\theta^2}{C_p} \\ C = 2\zeta\sqrt{KM} = \frac{2\zeta K}{\omega_n} \\ \bar{F}_{aero} = F_{aero} \cdot \left(1 + \frac{3D_e}{4L_b}\right) \end{cases} \tag{4}$$

where $\rho_b, w_b, t_b$ are the density, width and thickness of the substrate, respectively; $m_p$ the mass of the piezoelectric layer; $\rho_c, D_e, D_i, L_c$ are the density, outer diameter, inner diameter and length of the tip hollow cylinder, respectively; $E$ is the Young's modulus of the composite beam; $\zeta$ and $\omega_n$ are the damping ratio and the natural angular frequency of the piezo-cantilever harvester; $\theta$ is the electro-mechanical coupling coefficient [11], which represents the amount of charge per unit displacement ($y$) collected in the piezo-layer in open-circuit condition; $C_p$ is the capacitance of the piezoelectric layer. The equation of motion derived from Lagrangian method is as follows:

$$M\ddot{y} + C\dot{y} + Ky = \bar{F}_{aero} \tag{5}$$

The Frequency Response Function (FRF) between the aerodynamic force $F_{aero}$ and the tip displacement $y$ is calculated assuming a harmonic response of the one-DoF system:

$$FRF_y(\omega) = \frac{y_0}{F_0} = \frac{\left(1+\frac{3D_e}{4L_b}\right)}{-M\omega^2+iC\omega+K} = \frac{1}{K}\cdot\frac{\left(1+\frac{3D_e}{4L_b}\right)}{\left(1-\frac{\omega^2}{\omega_n^2}+2i\zeta\frac{\omega}{\omega_n}\right)} \tag{6}$$

The Open Circuit Voltage (OCV) $v_{oc}(t)$ across the terminals of the electrodes of the piezoelectric layer is expressed as follows [11]:

$$v_{oc}(t) = \frac{\theta}{C_p}\cdot y(t) \tag{7}$$

Finally, by letting (6) in (7), the FRF between the aerodynamic force $F_{aero}$ and the generated OCV is obtained as:

$$FRF_{v_{oc}}(\omega) = \frac{V_{oc}}{F_0} = \frac{\theta}{KC_p}\cdot\frac{\left(1+\frac{3D_e}{4L_b}\right)}{\left(1-\frac{\omega^2}{\omega_n^2}+2i\zeta\frac{\omega}{\omega_n}\right)} \tag{8}$$

## 3 Experimental validation

Experimental tests aimed at validating the analytical lumped parameter model. A prototype of a cantilever harvester built by Smart Material GmbH and Focchi Spa was used. The piezoelectric layer in the prototype consists in a Macro Fiber Composite (MFC) piezo-patch (M–8514–P2, manufactured by Smart Material GmbH) bonded to a structural substrate made by FR-4 (glass-reinforced epoxy laminate material). The tip mass is a hollow cylinder made by a polymeric material using an additive manufacturing technique. Figure 2 shows the main dimensions of the piezo-cantilever harvester used during tests. The dimensions of the piezo-patch and its electromechanical properties are available in [14].

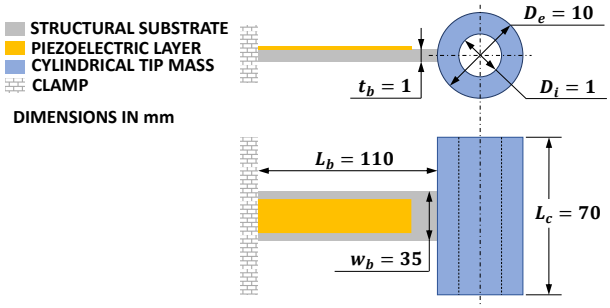


**Fig. 2.** Scheme of the prototype of the piezo-cantilever harvester used in experimental tests.

The FRF between the aerodynamic force (excitation) and the OCV (response) was measured after applying to the cylindrical tip mass in Fig. 3 an impulsive force along

the vertical direction. The excitation was applied using a mini instrumented hammer for modal analysis (PCB 084A17). The two signals (applied force and OCV) were acquired using a DAQ module NI 9230 and the software NI Signal Express.

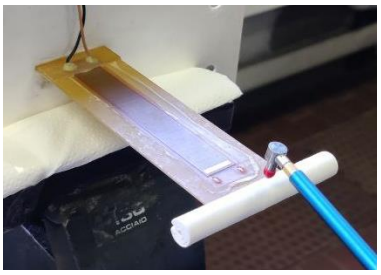

**Fig. 3.** An experimental test for FRF measurements.

Figure 4 shows that the analytical and experimental FRFs are in a very good agreement. It is worth highlighting that the analytical FRF is computed from (8), whereas experimental FRF is computed using the software NI Signal express and it is the average of the FRFs measured on three tests, performed to check repeatability.

In table 1 the values of the natural frequency and the peak amplitude obtained in the numerical and experimental FRFs are compared.

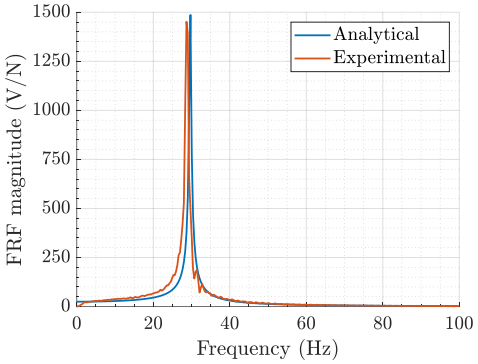


**Fig. 4.** Comparison between analytical and experimental FRFs. The analytical FRF is derived from (8).

**Table 1.** Comparison between analytical and experimental FRFs.

| | *Analytical* | *Experimental* |
|---|---|---|
| *Natural frequency (Hz)* | 29.7 | 28.7 |
| *FRF peak value (V/N)* | 1485.9 | 1451.6 |

The experimental damping ratio is 0.81 % and is determined using the logarithmic decrement method.

Using (2) and the value of the experimental natural frequency ($f_{n,exp}$), it is possible to determine the optimal velocity $\bar{U}$ of the fluid flow which causes the resonance of the harvester. It is obtained $\bar{U} = 1.4\ m/s$, (assuming $D = D_e,\ S_t = 0.21$ [9]).

## 4 Optimization algorithm

From (1) it can be noted that the aerodynamic force is proportional to the windward cross-section of the cylinder ($A_c$). Moreover, in (7) it is highlighted that a large displacement ($y$) of the end of the beam leads to a large voltage output, therefore a decrease in the natural frequency $f_n$ (or stiffness $K$, see (6)) of the cantilever increases the performance of the harvester. An optimization algorithm can be defined to find the optimal dimensions of the harvester, not only to guarantee the matching between natural and vortex shedding frequencies, but also to maximize performance.
The optimization algorithm used in the framework of this research is based on the *fmincon* function available in MATLAB [15], which finds a constrained minimum of a function $FUN(X)$ of several design variables (X). It is assumed that the objective of the optimization is to maximize the generated OCV. The design variables are represented by the dimensions of the structural substrate and the cylinder depicted in Fig. 2, hence $X = [w_b, t_b, L_b, D_e, D_i, L_c]$. It is worth noticing that the piezo-patch and the materials of the substrate and the cylinder are the same of the prototype. Therefore, the function $FUN(X)$ to be minimized is derived from (8) and is as follows:

$$FUN(X) = \frac{1}{V_{oc}(X)} = \frac{K(X)C_p}{\theta} \cdot \frac{\sqrt{\left(1-f_{vs}^2\frac{M(X)}{K(X)}\right)^2 + \left(2\zeta f_{vs}\sqrt{\frac{M(X)}{K(X)}}\right)^2}}{\left(1+\frac{3D_e}{4L_b}\right)} \cdot \frac{2}{C_{L0}\rho_a D_e L_c \bar{U}^2} \tag{9}$$

The problem is subjected to linear and non-linear constraints:

$$\min_{\mathrm{X}} \frac{1}{V_{oc}(X)} \text{ such that } \begin{cases} A \cdot X \leq B \\ A_{eq} \cdot X = B_{eq} \\ C(X) \leq 0 \\ C_{eq}(X) = 0 \end{cases} \tag{10}$$

in which $A, A_{eq}$ are matrices of coefficient and $B, B_{eq}$ are vectors of known constants; $C(X), C_{eq}(X)$ are non-linear functions. The *fmincon* function starts the research of the optimum values of the parameters from the first guess values $X_0$ of the design variables. The solution $X$ of the problem is found within the range defined by the lower ($LB$) and upper ($UB$) limits, that is:

$$LB \leq X \leq UB \tag{11}$$

The default algorithm interior-point is used to minimize the function $FUN$ and no further options were specified in the *fmincon* function.

It is defined only one linear constraint, which imposes a minimum thickness of the hollow cylinder, i.e. $D_e - D_i \geq 4\ mm$. Therefore, it is imposed $A = [0\ 0\ 0 - 1\ 1\ 0]$ and $B = -4 \cdot 10^{-3}$. Three non-linear constraints are introduced:

1. The natural frequency $f_n$ of the cantilever harvester must be tuned to the vortex shedding frequency at the given wind velocity. It is imposed that they match within a small range of frequencies, i.e.:

$$|f_n - f_{vs}| - 0.1 \leq 0 \tag{12}$$

2. The static displacement $w_s$ of the end of the cantilever [12] must be lower than a given maximum limit:

$$w_s - 0.005 \leq 0 \tag{13}$$

3. The maximum dynamic stress $\sigma_d$ at clamp [12, 16, 17] must be lower than a given maximum limit:

$$\sigma_d - 20 \cdot 10^6 \leq 0 \tag{14}$$

Table 2 shows the values used for the optimization for the parameters $X_0,\ LB,\ UB$. Table 3 shows the results of the optimization, i.e. the optimal values of the variables. The reference wind velocity is $\bar{U} = 1.4\ m/s$.

**Table 2.** Assumed values for $X_0,\ LB,\ UB$.

| | $w_b(mm)$ | $t_b\ (mm)$ | $L_b\ (mm)$ | $D_e\ (mm)$ | $D_i\ (mm)$ | $L_c\ (mm)$ |
|---|---|---|---|---|---|---|
| $LB$ | 18 | 0.5 | 100 | 10 | 0 | 70 |
| $X_0$ | 35 | 1 | 110 | 10 | 1 | 70 |
| $UB$ | 40 | 2 | 150 | 45 | 41 | 100 |

**Table 3.** Optimal values of the design variables.

| $w_b$ $(mm)$ | $t_b$ $(mm)$ | $L_b$ $(mm)$ | $D_e$ $(mm)$ | $D_i$ $(mm)$ | $L_c$ $(mm)$ | $f_n$ $(Hz)$ | $f_{vs}$ $(Hz)$ | $w_s$ $(mm)$ | $\sigma_d$ $(MPa)$ |
|---|---|---|---|---|---|---|---|---|---|
| 18.2 | 1 | 114.9 | 19.9 | 14.5 | 99.9 | 14.8 | 14.8 | 1.1 | 1.0 |

The optimal OCV output, calculated using (9) and referred to the optimal values of the design variables in Table 3, results $V_{oc,opt} = 1.8\ V$ (assuming $\rho_a = 1.225 \frac{kg}{m^3}$, $C_{L0} = 0.3$ [10]). The OCV output calculated using (9) and referred to the dimensions of the prototype (see Fig. 2) results $V_{oc} = 0.37\ V$, which is 4.9 times smaller than the optimal value. Finally, it is worth highlighting that the optimal natural frequency is smaller than the one of the prototype, whereas $A_c$ increases, due to the larger values of both $D_e$ and $L_c$.

## 5 Conclusions

The experimental tests showed that the lumped element model is able to retain the most important features of the harvester's dynamics and is suited to optimization purposes. Numerical calculations showed that optimization can lead to a large improvement of performance, since the generated power is proportional to the voltage squared. The

methods presented in this paper are suited to model and optimize more complex wind harvesters composed of multiple beams and cylinders.

**Acknowledgments** The authors want to acknowledge all the partners involved in the H2020 InComEss project—Innovative polymer-based Composite systems for high-efficient Energy scavenging and storage (Project ID: 862597).

## 6 References

1. Guardigli, L. *et al.*: Sviluppo di un prototipo di facciata continua con comportamento dinamico (SmartSkin). Journal of Technology for Architecture & Environment, *16* (2018)
2. Arnesano, M., *et al.*: A sub-zonal PMV-based HVAC and façade control system for curtain wall buildings. In MDPI Proceedings (Vol. 2, No. 15, p. 1596) (2018)
3. Arnesano, M., *et al.*: Sensors and control solutions for Smart-IoT façade modules. In *20*19 IEEE International Symposium on Measurements & Networking (M&N*)* (pp. 1-6), IEEE, (2019)
4. INCOMESS Project, INnovative Polymer-Based Composite Systems for High-Efficient Energy Scavenging and Storage. Available online: https://www.incomess-project.com/ (accessed on 21 March 2022).
5. Hobbs, William B. *et al.*: Tree-inspired piezoelectric energy harvesting. Journal of Fluids and Structures 28: 103-114 (2012)
6. Akaydin, H. D. *et al.*: The performance of a self-excited fluidic energy harvester. Smart Mat. and Struct., 21(2), 025007, (2012)
7. Hobeck, J. D. *et al.*: Artificial piezoelectric grass for energy harvesting from turbulence-induced vibration. Smart Mat. and Struct., *21*(10), 105024 (2012)
8. S. Orrego, K. Shoele et al..: Harvesting ambient wind energy with an inverted piezoelectric flag. Applied Energy, 194, 212–222, (2017)
9. Blevins, R. D.: Flow-induced vibration. New York: Van Nostrand Reinhold Co (1977)
10. Païdoussis, M. P. *et al.*: Fluid-structure interactions: cross-flow-induced instabilities. Cambridge University Press (2010)
11. Erturk, A. *et al.*: Piezoelectric energy harvesting. John Wiley & Sons (2011)
12. Doria, A. *et al.*: Tuning of Vibration Energy Harvesters by Means of Liquid Masses. In: 2021 Sixteenth International Conference on EVER, IEEE pp. 1-7 (2021)
13. Akaydin, H. D. *et al.*: Energy harvesting from highly unsteady fluid flows using piezoelectric materials. J. of Intelligent Material Sys. and Struct., 21(13), 1263-1278 (2010)
14. https://www.smart-material.com/media/Datasheets/MFC_V2.4-datasheet-web.pdf (availability checked on 11/03/2022)
15. Bottin, M. *et al.*: Analysis and control of vibrations of a Cartesian cutting machine using an equivalent robotic model. Machines *9*(8), 162 (2021)
16. Doria, A. et al..: Energy harvesting from bicycle vibrations by means of tuned piezoelectric generators. Electronics 9(9): 1377 (2020)
17. Tommasino, D. *et al.*: Vibration Energy Harvesting by Means of Piezoelectric Patches: Application to Aircrafts. Sensors, *22*(1), 363, (2022)